Advancing medical devices for novel image-guided percutaneous cardiac interventions

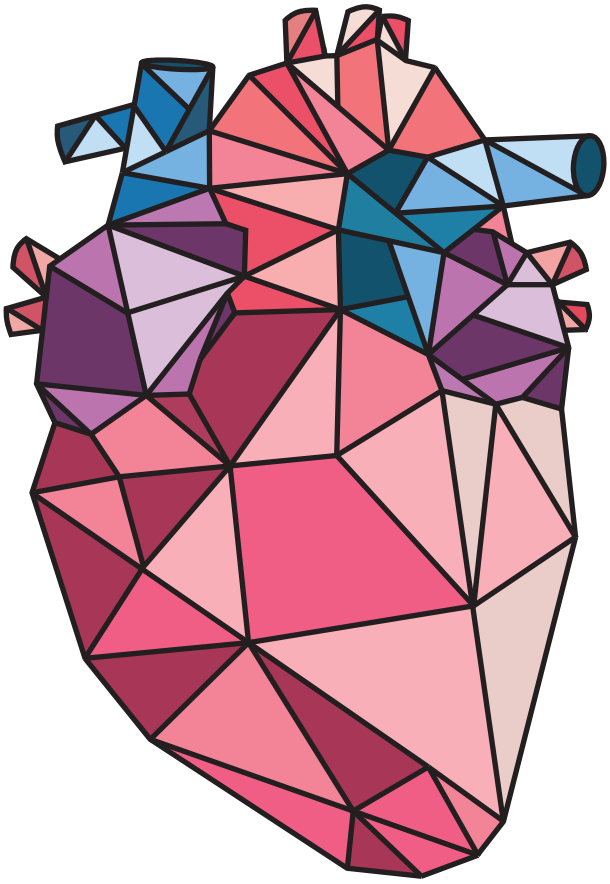

H.T. van den Broek

Advancing medical devices for novel image-guided percutaneous cardiac interventions

Hans Thijs van den Broek

Advancing medical devices for novel image-guided percutaneous cardiac interventions

ISBN	978-94-6380-409-7
Cover design	Hans Thijs van den Broek
Layout design	Proefschriftmaken.nl
Printed by	Proefschriftmaken.nl

Advancing medical devices for novel image-guided percutaneous cardiac interventions

Het bevorderen van medische hulpmiddelen voor nieuwe beeld gestuurde percutane hartinterventies

(met een samenvatting in het Nederlands)

Proefschrift

ter verkrijging van de graad van doctor aan de
Universiteit Utrecht
op gezag van de
rector magnificus, prof.dr. H.R.B.M. Kummeling,
ingevolge het besluit van het college voor promoties
in het openbaar te verdedigen op
donderdag 5 september 2019 des middags te 2.30 uur

door

Hans Thijs van den Broek

geboren op 7 december 1987 te Arnhem

Promotoren:	Prof. dr. S.A.J. Chamuleau
	Prof. dr. P.A.F.M. Doevendans
Copromotoren:	Dr. F.J. van Slochteren
	Dr. R. van Es

Financial support by the Dutch Heart Foundation for the publication of this thesis is gratefully acknowledged.

Publication of this thesis was additionally supported by ACIST Europe, Boston Scientific Nederland, CART-Tech B.V., ChipSoft, Servier Nederland Farma B.V.

Contents

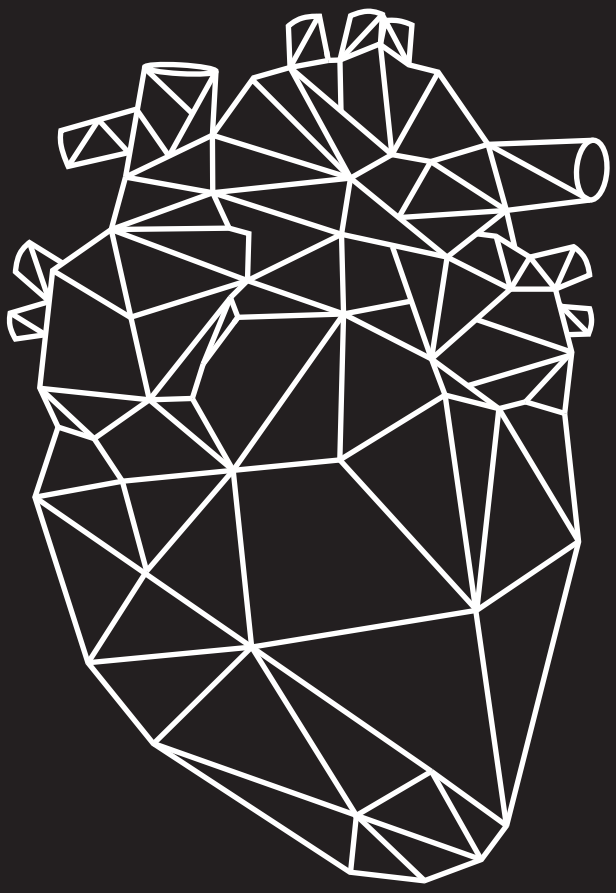

Chapter 1

Introduction

Cardiovascular Heart Disease

Disease epidemiology

Cardiovascular diseases are the global leading cause of death, with an estimated 17.9 million cardiovascular-related deaths in 2015.[1] A substantial contributor to cardiovascular morbidity and mortality is heart failure (HF). This complex clinical syndrome is present in approximately 2-3% of the adult population but most prevalent in the population above 65 years of age.[2,3] About half of the patients who develop HF die within 5 years of diagnosis.[4] HF is characterized by structural or functional ventricular impairment, leading to reduced cardiac output and/or increased intracardiac pressures at rest or during stress, and its progressive nature.[5,6]

Progression to heart failure

A major cause of developing HF is coronary artery disease (CAD) with previous myocardial infarction (MI).[5] In the acute phase of MI, myocardial perfusion is restored by a percutaneous coronary intervention. Despite timely intervention, patients can develop clinical symptoms due to the sustained damage of the cardiac muscle related to the ischemic event. To improve cardiac function and provide secondary prevention, adjunctive pharmacological treatment is started consisting of angiotensin-converting enzyme inhibitors, beta-blockers, aspirin, and statins. Successful interventional and pharmacological treatment of cardiovascular diseases has contributed to an increasing group of patients that survive CAD and eventually develop chronic HF.

Other causes of HF, besides CAD, include hypertension and abnormalities of the heart valves, pericardium, endocardium, heart rhythm and electrical conduction.[7] HF patients may develop heart rhythm and electrical conduction disorders,[8] e.g. left bundle branch block or intraventricular conduction delay, which has severe implications for cardiac function and prognosis.[9] It is estimated that in more than a third of chronic HF patients an electrical conduction disorder is present.[10] Abnormalities in heart rhythm and electrical conduction are therefore an important target for the treatment of chronic HF patients.

Current treatment strategies

In patients with chronic stable HF, the syndrome is often regulated by lifestyle modifications and pharmacological treatment.[5] Patients with moderate to severe HF, however, require interventional treatments, including revascularization to restore perfusion, valve repair and replacement to restore valve structure, cardiac resynchronization therapy (CRT) to restore conduction delays and improve heart rhythm, and mechanical support such as left ventricular assist devices to take over the heart when all function is lost.[5] These interventions aim to prevent left ventricular deterioration and/or improve left ventricle (LV) function, provide relief of the symptoms, and to prolong life. The only definite cure of HF is heart transplantation, but this is only available for a limited number of patients suffering from end-stage heart failure.[11]

Although current treatment strategies have had a beneficial effect on the treatment of patients with symptomatic HF, optimizations or introduction of novel therapies are needed to improve procedural safety, procedural outcomes, and their success rate. The effect of CRT, for example, is limited to 55-70% response rate.[12] However, several studies have shown that the response rate can be improved by, for example, targeting optimal pacing sites for LV stimulation.[13–15] These findings show that optimizations to the current interventional treatment strategies are necessary to help the increasing group of HF patients.

Challenges to optimize treatment strategies

Evolving technologies in the field of interventional cardiology have contributed to an enhanced quality of life and survival of patients suffering from cardiovascular diseases.[16] Diagnostic non-invasive multimodality imaging has brought new insights into the diagnosis and management of this patient population.[17,18] In the catheterization theatre advanced catheter-based techniques and therapies alongside imaging technologies have become routine in a large number of centres worldwide.[19,20] Yet, the main interventional imaging modality, X-ray fluoroscopy (XRF), provides high spatial resolution live 2D imaging but has several disadvantages: radiation exposure; foreshortening; opacification of overlying structures; and the lack of soft-tissue visualization. To further optimize interventional

treatment strategies, several challenges have to be overcome: 1. Three-dimensional (3D) imaging; 2. Soft-tissue visualization; 3. Treatment planning; 4. Limiting radiation and contrast agent exposure.

Three-dimensional hybrid imaging

XRF alone is not suitable to accurately deliver therapy in a dynamic complex three-dimensional environment.[21] For a better understanding of the tissues and to provide a safe outcome during complex catheterization procedures, XRF is often supported by pre- or peri-procedurally acquired images of the anatomy.[22,23] Diagnostic 3D imaging techniques, such as 3D ultrasound, magnetic resonance imaging (MRI) or computed tomography (CT), are increasingly used to visualize the cardiac anatomy. Interventional targets are no longer assessed in 2D but as 3D objects, but with a topographic surrounding (e.g. ischemic areas, airway, aorta next to pulmonary artery) with certain physiological and pathological characteristics. Introduction of novel and/or advanced 3D imaging techniques in the catheterization laboratory to visualize tissue characteristics in order to provide more detail and better procedural outcomes still needs to be investigated.

Soft-tissue visualization

The addition of 3D imaging techniques requires the understanding of advanced imaging solutions capable of soft-tissue visualization and how to use them in conjunction with the main interventional imaging modality, XRF. Current X-ray technology focusses on contrast-based visualization (angiography) and is not suitable for soft-tissue (e.g. myocardial scar or electrical conduction delay) visualization. Multiple studies have shown that the combination of anatomical, morphological and functional imaging, increases diagnostic accuracy and improves the efficacy of therapeutic interventions.[17,18,24–26] However, the information is provided separately during the intervention which makes the current process of optimal target selection inefficient. Moreover, due to the separate presentation of data the cardiologist is compelled to combine all imaging information in the mind. Each imaging modality requires specific anatomic knowledge to interpret the images and to identify abnormalities and the spatial relationship can be different and uncorrelated, therefore, combining the data on the spot can become quite complex. This is also a limiting issue for cross talk within the team. Investigating new hybrid imaging approaches that incorporate

anatomical, morphological and functional imaging to guide the cardiologist may be of great importance for therapy target selection and improving efficacy of therapeutic interventions.

Treatment planning

Treatment planning is referred to as the process of preparing for an intervention during which the available patient (medical imaging) information is used to decide about the optimal access route, optimal treatment locations, depth and angle. The importance of treatment planning is becoming more apparent with the growing use of 3D imaging and soft-tissue visualization. For example, to optimize structural heart disease interventions requires accurate prosthesis selection based on the outflow or inflow tract and annulus dimensions.[27,28] Prosthesis selection can either be performed pre-procedural with diagnostic imaging (e.g. CT) or peri-procedural based on a 3D rotational angiography.[28–30] 3D rotational angiography is a technique in which the anatomy is reconstructed from multiple X-ray acquisitions resulting in a CT-like volumetric dataset. Accurate prosthesis selection is important to ensure stable positioning of the prosthesis, to prevent leakage, and to prevent blockage of neighbouring structures (e.g. coronary arteries in case of prosthetic aortic valves). It can be reasoned that more complex interventional treatments, e.g. which require soft-tissue visualization to perform substrate targeting or substrate modification, gain a higher effect of treatment planning. It is, therefore, necessary to investigate the effect of treatment planning on the procedural outcomes.

Limiting radiation and contrast agent exposure

The increasing complexity of the percutaneous cardiovascular interventions, e.g. due to the introduction of novel treatment strategies, under the guidance of XRF, contribute to increased radiation and contrast agent exposure. Structural and valvular cardiac interventional procedures have been associated with the highest reported radiation exposures among cardiac interventions.[31] Radiation exposure is harmful to both patients and staff and has, therefore, in recent years been a focus of researchers in the field.[32,33] Pediatric patients are especially vulnerable due to the longer life span and the vulnerability for direct tissue damage and developing cancer.[34] While ionizing radiation is mainly a concern in pediatric patients, decreasing iodinated contrast agent exposure is necessary to limit the kidney burden in adult HF patients.[32,35] Pre-existing renal impairment is present in

about 10% of patients with chronic HF.[36] Hybrid fusion imaging technology incorporating treatment planning, guidance, and targeting may contribute to a decrease in radiation and contrast exposure.

Clinical Translation

In the last decade, multiple research groups have been working on fusing imaging modalities and large medical imaging companies have introduced novel imaging solutions for multiple cardiovascular disease interventions.[22,37] Overall, there has been major interest in technologies and methods to provide targeted delivery of therapy to the most optimal location.[38–40] The peri-procedural 3D image registration modality that is capable of visualizing the entire surrounding and add soft-tissue contrast to the interventional imaging suite is referred to as hybrid imaging.[22] The pathway for the development of new image-guided catheter interventions starts before introduction in the clinical practice. Developing and testing new technologies requires precise validation studies in order to assess and validate the targeting accuracy. Yet, the combination of (novel) technologies requires medical and technological knowledge to ensure optimal synergy to optimize current catheterization procedures.

This thesis investigates and tackles the challenges of treatment planning, guidance targeting, and radiation and contrast agent exposure of complex percutaneous cardiac interventions. Medical and technical expertise is used to innovate with current medical technology and develop novel imaging technologies. Hence together with CART-Tech B.V. (Utrecht, The Netherlands), CARTBox was developed to facilitate advanced treatment planning and image guidance during complex percutaneous cardiac interventions. CARTBox enables the user to identify targets based on the lesions in the myocardium and the exclusion of healthy tissue or unsafe locations in the heart derived from cardiac MRI in a standardized manner. Using hybrid imaging the cardiologist is guided towards the optimal therapy location by superimposing 3D visualized targets onto live XRF images. The path from the development of medical devices to clinical practice is an important, but a laborious process that involves many software testing steps as well as validation steps including pre-clinical and clinical research. In this thesis, the need in clinical practice is identified, followed

by an assessment of safety and feasibility and use of a newly developed histology protocol for validation of accuracy in pre-clinical research. Next, the safety and feasibility of the CARTBox software are tested in a first-in-man study. Furthermore, a novel method to assess the myocardial tissue properties based on catheter mapping data is proposed.

Thesis outline

In this thesis, 'Advancing medical devices for novel image-guided percutaneous cardiac interventions', we present and discuss the pathway from limitations in cardiac interventional imaging towards advanced treatment planning and image-guided approaches to improve cardiac catheterization interventions. In **Chapter 2**, we review the current clinical application of hybrid imaging by means of integrating different imaging modalities during cardiovascular interventions. This chapter provides an overview of various hybrid fusion imaging technologies incorporating rotational angiography focused on structural and congenital heart diseases.

The clinical translation of new image-guided catheter approaches requires more precise validation techniques in order to assess and validate the targeting accuracy of these newly developed methods. In **Chapter 3**, we describe a novel validation protocol based on myocardial tissue analysis. This protocol includes whole-heart myocardial tissue processing that enables detailed two-dimensional and three-dimensional analysis of the cardiac anatomy and intramyocardial injections.

In **Chapter 4**, we use the same histological analysis method to validate a newly developed software tool for image-guided cardiac catheter therapy, CARTBox2. In a non-inferiority study, the targeting accuracy of a novel software method for MRI-fluoroscopy guided endomyocardial interventions is compared with the clinical standard for intramyocardial injections, the NOGA XP electromechanical mapping system. In **Chapter 5**, the safety and feasibility of the CARTBox3 treatment-guidance platform are assessed in a first-in-man study involving cardiac resynchronization therapy device implantation. In this study, the safety and feasibility of the visualization of optimal left ventricular pacing sites during the implantation is tested in a step-wise approach.

In **Chapter 6**, we present a new method to assess the myocardial tissue properties based on catheter mapping data by a logistic prediction model for MI based on multiple electromechanical parameters to distinguish infarcted from healthy myocardium. In a retrospective study, we evaluate the predictive accuracy of this model in a porcine model of chronic myocardial infarction. Furthermore, we compare electromechanical-derived parameters of local mechanical activity to MRI-feature tracking derived parameters.

In the final chapter of this thesis, **Chapter 7**, we summarize the major findings and conclusions of each preceding chapter and address the clinical implications. Furthermore, we discuss future developments and the necessary advancements in the cardiovascular interventional domain.

References

1. Wang H, Naghavi M, Allen C, Barber RM, et al. Global, regional, and national life expectancy, all-cause mortality, and cause-specific mortality for 249 causes of death, 1980-2015: a systematic analysis for the Global Burden of Disease Study 2015. *Lancet* 2016;**388**(10053):1459–1544. doi:10.1016/S0140-6736(16)31012-1.

2. Roger VL. Epidemiology of Heart Failure. *Circ Res* 2013;**113**(6):646–659. doi:10.1161/CIRCRESAHA.113.300268.

3. Riet EES van, Hoes AW, Wagenaar KP, Limburg A, et al. Epidemiology of heart failure: the prevalence of heart failure and ventricular dysfunction in older adults over time. A systematic review. *Eur J Heart Fail* 2016;**18**(3):242–252. doi:10.1002/ejhf.483.

4. Roger VL. Trends in Heart Failure Incidence and Survival in a Community-Based Population. *JAMA* 2004;**292**(3):344. doi:10.1001/jama.292.3.344.

5. Yancy CW, Johnson MR, Masoudi FA, Januzzi JL, et al. 2013 ACCF/AHA Guideline for the Management of Heart Failure. *J Am Coll Cardiol* 2013;**62**(16):e147–e239. doi:10.1016/j.jacc.2013.05.019.

6. Mann DL, Bristow MR. Mechanisms and Models in Heart Failure. *Circulation* 2005;**111**(21):2837–2849. doi:10.1161/circulationaha.104.500546.

7. Khatibzadeh S, Farzadfar F, Oliver J, Ezzati M, Moran A. Worldwide risk factors for heart failure: A systematic review and pooled analysis. *Int J Cardiol* 2013;**168**(2):1186–1194. doi:10.1016/j.ijcard.2012.11.065.

8. Schneider JF, Thomas HE, Kreger BE, Mcnamara PM, Kannel WB. Newly Acquired Left Bundle-Branch Block: The Framingham Study. *Ann Intern Med* 1979;**90**(3):303–310.

9. Jørgensen TH, Backer O De, Gerds TA, Bieliauskas G, et al. Mortality and Heart Failure Hospitalization in Patients With Conduction Abnormalities After Transcatheter Aortic Valve Replacement. *JACC Cardiovasc Interv* 2019;**12**(1):52–61. doi:10.1016/j.jcin.2018.10.053.

10. Lund LH, Benson L, Ståhlberg M, Braunschweig F, et al. Age, prognostic impact of QRS prolongation and left bundle branch block, and utilization of cardiac resynchronization therapy: findings from 14 713 patients in the Swedish Heart Failure Registry. *Eur J Heart Fail* 2014;**16**(10):1073–1081. doi:10.1002/ejhf.162.

11. Jonge N De, Kirkels JH, Klöpping C, Lahpor JR, et al. Guidelines for heart transplantation. *Netherlands Hear J* 2008;**16**(3):79–87. doi:10.1007/BF03086123.

12. Daubert J-C, Saxon L, Adamson PB, Auricchio A, et al. 2012 EHRA/HRS expert consensus statement on cardiac resynchronization therapy in heart failure: implant and follow-up recommendations and management. *Hear Rhythm* 2012;**9**(9):1524–1576. doi:10.1016/j.hrthm.2012.07.025.

13. Saba S, Marek J, Schwartzman D, Jain S, et al. Echocardiography-Guided Left Ventricular Lead Placement for Cardiac Resynchronization Therapy: Results of the Speckle Tracking Assisted Resynchronization Therapy for Electrode Region Trial. *Circ Hear Fail* 2013;**6**(3):427–434. doi:10.1161/CIRCHEARTFAILURE.112.000078.

14. Khan FZ, Virdee MS, Palmer CR, Pugh PJ, et al. Targeted Left Ventricular Lead Placement to Guide Cardiac Resynchronization Therapy. *J Am Coll Cardiol* 2012;**59**(17):1509–1518. doi:10.1016/j.jacc.2011.12.030.

15. Leyva F. Cardiac resynchronization therapy guided by cardiovascular magnetic resonance. *J Cardiovasc Magn Reson* 2010;**12**(1):64. doi:10.1186/1532-429X-12-64.

16. Kpodonu J. Hybrid Cardiovascular Suite: The Operating Room of the Future. *J Card Surg* 2010;**25**(6):704–709. doi:10.1111/j.1540-8191.2010.01111.x.

17. Hoeven BL van der, Schalij MJ, Delgado V. Multimodality imaging in interventional cardiology. *Nat Rev Cardiol* 2012;**9**(6):333–346. doi:10.1038/nrcardio.2012.14.

18. Chambers JB, Myerson SG, Rajani R, Morgan-Hughes GJ, Dweck MR. Multimodality imaging in heart valve disease. *Open Hear* 2016;**3**(1):e000330. doi:10.1136/openhrt-2015-000330.

19. Sousa JE, Costa MA, Tuzcu EM, Yadav JS, Ellis S. New frontiers in interventional cardiology. *Circulation* 2005;**111**(5):671–681. doi:10.1161/01.CIR.0000153802.70682.22.

20. Hijazi ZM, Awad SM. Pediatric Cardiac Interventions. *JACC Cardiovasc Interv* 2008;**1**(6):603–611. doi:10.1016/j.jcin.2008.07.007.

21. Green NE, Chen SYJ, Messenger JC, Groves BM, et al. Three-dimensional vascular angiography. *Curr Probl Cardiol* 2004;**29**(3):101–142. doi:10.1016/j.cpcardiol.2004.02.002.

22. Voskuil M, Sievert H, Arslan F. Guidance of interventions in structural heart disease; three-dimensional techniques are here to stay. *Netherlands Hear J* 2017;**25**(2):63–64. doi:10.1007/s12471-016-0945-0.

23. Pedra CA, Fleishman C, Pedra SF, Cheatham JP. New imaging modalities in the catheterization laboratory. *Curr Opin Cardiol* 2011;**26**(2):86–93. doi:10.1097/HCO.0b013e3283437fb4.

24. Prior JO, Farhad H, Muller O. Multimodality Imaging in Ischemic Cardiomyopathy. *Curr Cardiovasc Imaging Rep* 2014;**7**(2014):9285. doi:10.1007/s12410-014-9285-x.

25. Paterson I, Mielniczuk LM, O'Meara E, So A, White JA. Imaging Heart Failure: Current and Future Applications. *Can J Cardiol* 2013;**29**(3):317–328. doi:10.1016/j.cjca.2013.01.006.

26. Gaemperli O, Saraste A, Knuuti J. Cardiac hybrid imaging. *Eur Heart J Cardiovasc Imaging* 2012;**13**(1):51–60. doi:10.1093/ehjci/jer240.

27. Piazza N, Jaegere P de, Schultz C, Becker AE, et al. Anatomy of the Aortic Valvar Complex and Its Implications for Transcatheter Implantation of the Aortic Valve. *Circ Cardiovasc Interv* 2008;**1**(1):74–81. doi:10.1161/CIRCINTERVENTIONS.108.780858.

28. Messika-Zeitoun D, Serfaty JM, Brochet E, Ducrocq G, et al. Multimodal Assessment of the Aortic Annulus Diameter. Implications for Transcatheter Aortic Valve Implantation. *J Am Coll Cardiol* 2010;**55**(3):186–194. doi:10.1016/j.jacc.2009.06.063.

29. Jabbour A, Ismail TF, Moat N, Gulati A, et al. Multimodality imaging in transcatheter aortic valve implantation and post-procedural aortic regurgitation: Comparison among cardiovascular magnetic resonance, cardiac computed tomography, and echocardiography. *J Am Coll Cardiol* 2011;**58**(21):2165–2173. doi:10.1016/j.jacc.2011.09.010.

30. Delgado V, Schuijf JD, Bax JJ. Pre-operative aortic valve implantation evaluation: Multimodality imaging. *EuroIntervention* 2010;**6**(SUPPL. G):38–47. doi:10.4244/.

31. Sciahbasi A, Ferrante G, Fischetti D, Miklin DJ, et al. Radiation dose among different cardiac and vascular invasive procedures: The RODEO study. *Int J Cardiol* 2017;**240**:92–96. doi:10.1016/j.ijcard.2017.03.031.

32. Picano E, Vañó E, Rehani MM, Cuocolo A, et al. The appropriate and justified use of medical radiation in cardiovascular imaging: A position document of the ESC Associations of Cardiovascular Imaging, Percutaneous Cardiovascular Interventions and Electrophysiology. *Eur Heart J* 2014;**35**(10):665–672. doi:10.1093/eurheartj/eht394.

33. Faroux L, Blanpain T, Nazeyrollas P, Tassan-Mangina S, et al. Trends in Patient Exposure to Radiation in Percutaneous Coronary Interventions Over a 10-Year Period. *Am J Cardiol* 2017;10–13. doi:10.1016/j.amjcard.2017.06.021.

34. Johnson JN, Hornik CP, Li JS, Benjamin DK, et al. Cumulative Radiation Exposure and Cancer Risk Estimation in Children With Heart Disease. *Circulation* 2014;**130**(2):161–167. doi:10.1161/CIRCULATIONAHA.113.005425.

35. Sinning J-M, Ghanem A, Steinhäuser H, Adenauer V, et al. Renal function as predictor of mortality in patients after percutaneous transcatheter aortic valve implantation. *JACC Cardiovasc Interv* 2010;**3**(11):1141–1149. doi:10.1016/j.jcin.2010.09.009.

36. Cleland JGF, Carubelli V, Castiello T, Yassin A, et al. Renal dysfunction in acute and chronic heart failure: Prevalence, incidence and prognosis. *Heart Fail Rev* 2012;**17**(2):133–149. doi:10.1007/s10741-012-9306-2.

37. Carminati M, Agnifili M, Arcidiacono C, Brambilla N, et al. Role of imaging in interventions on structural heart disease. *Expert Rev Cardiovasc Ther* 2013;**11**(12):1659–1676. doi:10.1586/14779072.2013.854166.

38. Behar JM, Claridge S, Jackson T, Sieniewicz B, et al. The role of multi modality imaging in selecting patients and guiding lead placement for the delivery of cardiac resynchronization therapy. *Expert Rev Cardiovasc Ther* 2016;**00**(00):1–15. doi:10.1080/14779072.2016.1252674.

39. Slochteren FJ, Es R, Gyöngyösi M, Spoel TIG, et al. Three dimensional fusion of electromechanical mapping and magnetic resonance imaging for real-time navigation of intramyocardial cell injections in a porcine model of chronic myocardial infarction. *Int J Cardiovasc Imaging* 2016;1–11. doi:10.1007/s10554-016-0852-x.

40. Goreczny S, Dryzek P, Morgan GJ, Lukaszewski M, et al. Novel Three-Dimensional Image Fusion Software to Facilitate Guidance of Complex Cardiac Catheterization 3D image fusion for interventions in CHD. *Pediatr Cardiol* 2017;**38**(6):1133–1142. doi:10.1007/s00246-017-1627-4.

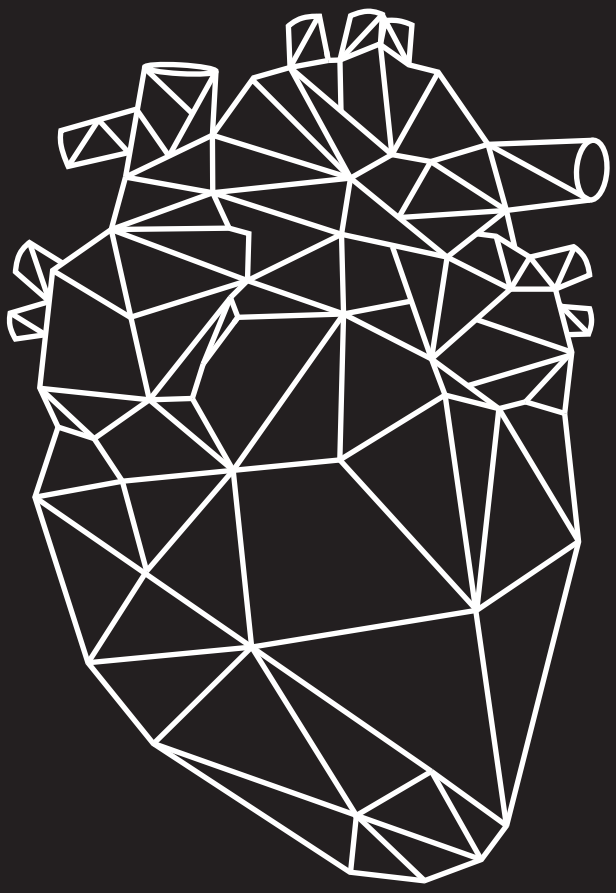

Chapter 2

3D Hybrid Imaging for Structural and Congenital Heart Interventions in the Cath Lab

3D Hybrid Imaging for Structural and Congenital Heart Interventions in the Cath Lab. Structural Heart, 2018, 2:5, 362-371, doi:10.1080/24748706.2018.1490841

HT. van den Broek MSc [1], R. van Es PhD [1], G.J. Krings MD PhD [3], Q.M.B. de Ruiter PhD [2], M. Voskuil MD PhD [1], M. Meine MD PhD [1], P. Loh MD PhD [1], P.A. Doevendans MD PhD [1,4], S.A.J. Chamuleau MD PhD [1], F.J. van Slochteren PhD [1]

[1] Department of Cardiology, University Medical Center Utrecht, Utrecht, The Netherlands
[2] Department of Vascular Surgery, University Medical Center Utrecht, Utrecht, The Netherlands
[3] Department of Paediatric Cardiology, Wilhelmina Children's Hospital, University Medical Center Utrecht, Utrecht, The Netherlands
[4] Netherlands Hearts Institute / Central Military Hospital Utrecht, Utrecht, The Netherlands

Abstract

Hybrid imaging (HI) during cardiovascular interventions enables the peri-procedural visualization of the organs and tissues by means of integrating different imaging modalities. HI can improve procedural efficacy and safety. This review provides an overview of different systems, their possibilities and the current clinical use and benefits focused on structural and congenital heart diseases. We have performed a literature search and linked the software options to the clinical use in cardiology to gain insight into the clinical use of the systems. In this review, we focus on radiation and contrast exposure, complication rate and procedure time. We found that currently available studies are limited by small cohorts. Nevertheless, HI systems for valvular procedures result in a significant decrease of radiation and contrast exposure. The largest benefit hereof is observed when HI is used in combination with rotational angiography. Furthermore, automatically determined optimal implant angle for transcatheter aortic valve implantation decreases the complication rate significantly. Congenital heart disease interventions that require 2D/3D TEE such as septal defects show a significant decrease in radiation and contrast exposure and procedural time when using TEE-XRF fusion software. MitraClip procedures using these HI systems, however, show only a trend in decrease of these effects. In conclusion, major interventional X-ray vendors offer HI software solutions which are safe and can aid the planning and image guidance of cardiovascular interventions. Even though current HI technologies have limitations, HI provides support in the increasingly complex cardiac interventional procedures to provide better patient care.

Introduction

Structural heart disease (SHD) and congenital heart disease (CHD) interventions involve a wide range of procedures which have expanded significantly during the last years. Minimal invasive therapies such as transcatheter aortic valve implantation (TAVI), devices for atrial septal defects (ASD), or clips to treat mitral regurgitation have become alternatives for surgical procedures.[1–4] As the expanding portfolio of interventional cardiology comes with new challenges, a need for imaging tools to support the cardiologist arose.

Standard mono- and biplane X-ray cine angiography and fluoroscopy (XRF) used during interventional cardiology procedures, primarily enable contrast-based visualization and are less suitable for the characterization of soft tissues. The increasing complexity of interventional procedures requires visualization of the topographic surrounding of interventional targets. This increases the radiation exposure and use of contrast medium during these interventions, which is potentially harmful to the patients and staff.[5] This paradigm drives the development of new techniques aiming to improve visualization while reducing radiation and contrast exposure. Currently, XRF is often supported side-by-side by pre- or peri-procedurally acquired imaging modalities as 2D/3D ultrasound, MRI, CT or a combination of these. Fusion of multiple imaging modalities, for instance fluoroscopy with CT, is referred to as hybrid imaging (HI).[6]

HI during cardiovascular interventions enables the peri-procedural visualization of the organs and tissues acquired by means of integrating different imaging modalities. HI can improve procedural efficacy and safety. This review provides an overview of different hybrid fusion imaging technologies incorporating rotational angiography, their possibilities, and the current clinical use and benefits for structural and congenital heart diseases.

Methods

We performed a PubMed and Embase search to identify full-text reports describing the use of image-guided structural, valvular and cardiac device closure interventions. In addition to the search results, we searched the references of relevant articles retrieved by the search strategy. Search terms included cardiac, structural heart disease or congenital heart disease; and image guidance, image guided, image guided therapy, hybrid imaging, fusion imaging or 3D imaging. Hereafter we linked the software options to the clinical application to gain insight into the use of the systems (e.g. radiation exposure, procedural time, complication rate etc.). Additionally, we have contacted the four largest interventional XRF companies (Philips Healthcare, Siemens Healthineers, GE Healthcare, and Canon Medical) and collected all necessary data to provide an overview of the different systems and their possibilities.

This article will briefly discuss the imaging modalities used for HI and review various types of interventions using HI divided into SHD (i.e. valvular interventions) and CHD (i.e. septal defects and obstructive lesions).

Imaging modalities used in HI

Pre-procedurally acquired imaging

The most frequently used pre-procedural imaging modalities that are integrated with live XRF images are Ultrasound and CT. However, cardiac MRI is increasingly used in the diagnostic workup in cardiovascular diseases and allows assessment of the function and structure of the cardiovascular system (e.g. heart function, myocardial infarct visualization, and perfusion imaging),[7] use of MRI for HI is still limited.

Cardiac CT is routinely used to evaluate coronary heart disease, evaluate heart and valve function, and assess calcium build-up in the coronary arteries and aorta. Modern CT setups use a multi-detector technique (up to 320 detectors). The high number of detectors results in high resolution 3D cardiac imaging data.[1]

Peri-procedurally acquired imaging

Traditionally, transoesophageal echocardiography (TEE) has been an important aid alongside XRF in structural and congenital heart procedures to facilitate amongst others, transcatheter mitral valve repair, trans-septal punctures (TSP), and closure of septal defects or paravalvular leaks.[8] TEE provides sufficient visualization of soft tissue whereas 3D TEE facilitates realistic representation of cardiac structures and allows navigation in 3D space. However, interpreting the images of TEE alongside XRF is difficult due to the different image orientation of the two modalities.

Cone-beam CT (CBCT), also referred to as C-arm CT, allows physicians to obtain a 3D volume reconstruction during the interventional procedure, from a single gantry rotation of a flat-panel detector XRF imaging setup.[9] The 3D volume obtained with CBCT resolves low contrast objects. CBCT is the underlying mechanism of a 3D rotational angiography (3DRA), which incorporates a contrast injection during the gantry rotation to visualize highly contrast enriched objects. The latter technique requires contrast injection in the proximal cavity of the region of interest during the entire rotation, to visualize the tissue-blood border, the depot effect. During the procedure, a 3D anatomical roadmap, acquired with 3DRA, can be superimposed onto the live XRF images (**Figure 1**). This provides e.g. instant visualization of the large arteries and the interventional devices. Furthermore, CBCT based 3D datasets can also be used to perform 3D to 3D data registration with e.g. CT, MRI, and SPECT (**Table 1 and 2**).

Caution while using HI (radiation and contrast exposure)

CBCT based HI interventions potentially expose the patient to increased levels of radiation and contrast compared to conventional XRF guidance. The reported radiation and contrast levels for CBCT are significantly lower than the median radiation exposure used in adult cardiac CT, especially with optimized CBCT protocols.[10–15] When used only for anatomical guidance during HI, CBCT is, therefore, the preferred modality. Moreover, a beneficial effect of CBCT + XRF based interventions compared to XRF alone interventions on skin dose is seen in patients.[16] The focus for optimizing CBCT protocols for adult patients is on reducing contrast use to limit the kidney burden while in the pediatric patients the focus is on reducing the radiation exposure.[17]

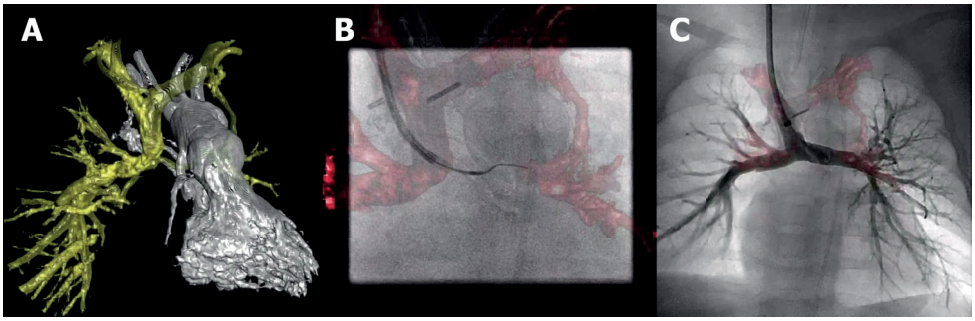

Figure 1: Hybrid imaging during recanalization of a partial cavo-pulmonary connection of the left pulmonary artery. A 3D reconstruction of the pulmonary artery tree (yellow structure) and left ventricle with outflow tract (white structure). **B** 3D overlay of the pulmonary tree is used to introduce a guidewire into the left pulmonary artery. **C** Contrast injection in the pulmonary artery tree with the stent in place.

Radiation reduction can be achieved by reducing the collimation, detector entrance dose, and frame rate with preservation of image quality (**Table 3**).[12,14,18] Several studies have shown that standardized acquisition and contrast protocols have a beneficial effect on radiation exposure and contrast use during SHD (**Table 3**).[10–13] Siemens systems require a short image acquisition to be done before starting the DynaCT to calibrate the CBCT settings. Too short image acquisition may result in high tube currents and therefore an unnecessary increase in radiation dose.[12] Next to lowering radiation exposure, the reduced amounts of contrast medium are also beneficial for the safety of the patients.[19]

Important for an adequate 3DRA acquisition is homogenous contrast density at the entire region of interest during the entire rotation. This requires a contrast protocol to enhance the spatial and temporal resolution of 3DRA. Critical for the contrast administration is the contrast location (depot), the amount of contrast (dilution) and timing of prefilling. In addition, the washout of contrast can be delayed using e.g. rapid ventricular pacing, inducing at least an arterial blood pressure reduction of 50%. Thus enhancing contrast density and edge sharpness. On the contrary, rapid ventricular pacing results in ventricular dimensions which do not represent normal physiological dimensions but are sized between diastolic and systolic dimensions. Furthermore, a breath hold or a respiratory stop during the acquisition minimizes movement of thoracic structures. The respiratory state is also important during registration of MRI or CT datasets. Registration of datasets with corresponding respiratory states results in a higher registration accuracy.

Table 1: Overview of advanced imaging options of major XRF vendors.

	Philips Healthcare		Siemens Healthineers		GE Healthcare		Canon Medical	
Systems	Allura Xper FD10/10, FD20/10, FD20 Azurion 5, 7		Artis Q, Q.zen Artis zee, zeego Artis pheno		IGS 3x0, 5x0, 6x0, 7x0 [a]		Infinix-i systems	
3D technology	3DRA	Cone-beam CT	3DRA	Cone-beam CT	3DRA	Cone-beam CT	3DRA	Cone-beam CT
Products	3DRA	XperCT	InSpace 3D	DynaCT	Innova 3D	Innova CT HD	3D-DA / 3D-DSA	Low Contrast Imaging
Anatomy best visualized	Contrast filled	Soft tissue, bones and contrast filled tissues	Contrast filled	Soft tissue, bones and contrast filled tissues	Contrast filled	Soft tissue, bones and contrast filled tissues	Contrast filled	Soft tissue, bones and contrast filled tissues
Acquisition time	80°/s (240 frames in 4s)	○ 80°/s (120 frames in 4s) ○ 80°/s (240 frames in 4s) ○ 24°/s (300 frames in 10s) ○ 24°/s (620 frames in 10s)	40°/s (133 frames in 5s) [b]	40°/s (248 frames in 5s) [b]	40°/s (approx. 150 frames in 5s)	○ 40°/s (approx. 250 frames in 5s) ○ 28°/s (approx. 350 frames in 7s) ○ 16°/s (approx. 600 frames in 12s)	○ 80°/s (250 frames in 2.6s) ○ 80°/s (400 frames in 2.6s) ○ 80°/s (600 frames in 2.6s)	○ 25°/s (250 frames in 10s) ○ 26.7°/s (400 frames in 15s) ○ 30°/s (600 frames in 20s)
Angular rotation (°)	240	240	200 2x 220 / 360 [c]	200 2x 220 / 360 [c]	200	200	210	210
Frame rate (fps)	30	30-60	26.6 [d]	49.6 [d]	30	50	100 [d]	25-30 [d]
Processing time	5s (256^3)	< 1min	< 20s	< 20s	< 30s	< 1min		
Spatial Resolution	256^3	256^3	256^3 (512^3)	256^3 (512^3)	512^3	512^3	256^3 (512^3)	256^3 (512^3)
Image integration	CT, MR		CT , MR, PET-CT		CT, MR, PET-CT, SPECT		CT, MR	

[a] X: 2 = 20 x 20 detector, 3 = 30 x 30 detector, 4 = 40 x 40 detector. [b] Artis Pheno can perform all 3D imaging acquisitions in 4s. [c] Artis Pheno can perform 360 degrees rotation. [d] Estimated based on acquisition time and angular rotation. 3DRA: 3D rotational angiography; CBCT: cone-beam CT; CT: computed tomography; MR: magnetic resonance; PET: positron emission tomography; SPECT: single positron emission CT.

Table 2: Overview of HI software tools of major XRF vendors for structural and congenital heart diseases.

	Philips Healthcare		**Siemens Healthineers**		**GE Healthcare**
Tools	HeartNavigator	EchoNavigator	Aortic Valve Guide	TrueFusion	HeartVision 2
Image Integration	CT	Echo (Philips CX50 or iE33, or Philips EPIC)	CBCT CT	Echo (Acuson SC2000 Prime only)	CBCT CT MR SPECT PET
Image Fusion	2D/3D matching of 3D volume with 2D XRF 3D/3D match with 3D XRF	Automatic fusion of 3D TEE with 2D XRF	2D/3D (2 2D XRF images > 30° apart) 3D/3D match with 3D XRF	Automatic fusion of 3D TEE with 2D XRF	2D/3D match with 2 2D XRF orthogonal (AP, Lateral) shots 3D/3D match with 3D XRF
Image Processing	**Automatic** segmentation: - Left ventricle - Aortic valve - Aorta - Coronary ostia	Demarcation of anatomical structures on echo	**Automatic** segmentation: - Aortic root - Coronary ostia - Aortic valve cusps Demarcation of landmarks	Demarcation of anatomical structures on echo	**Automatic** segmentation: - Left cavities (CT) - Left atrium (Innova 3D/CT HD) - Large structures (CT/Innova 3D/ Innova CT HD)

Measurements	**Automatic:** Annulus: - Diameter - Perimeter - Area Aortic: - Diameters above annulus - Ostia heights - Sinus diameters		Annulus: - Diameter - Perimeter - Area	**Automatic:** Annulus: - Diameter - Perimeter - Area Aortic: - Root Sinotubular junction - Root Sinus of Valsalva	**Automatic:** Annulus: - Diameter - Perimeter - Area Aortic: - Diameters above annulus - Ostia heights - Sinus diameters
Roadmap + extra markers	Real-time 3D volume or outline overlay	Real-time 3D TEE overlay Demarcation of landmarks	Real-time 3D volume or outline overlay Demarcations of Cusp nadirs, coronary ostia markers and ascending aorta centreline Add circle of perpendicularity	Real-time 3D TEE overlay Demarcation of landmarks	Real-time 3D volume overlay Add landmark points and planning lines
Optimal X-ray angle	Yes TAVI		Yes	Yes	Yes TAVI
Additional	Device selection and view planning Calcification distribution ascending aorta	Automatic tracking of TEE transducer position and orientation Automatic TEE field of view outline is displayed		Automatic tracking of TEE transducer position and orientation Automatic TEE field of view outline is displayed	

3DRA: 3D rotational angiography; CBCT: cone-beam CT; CT: computed tomography; MR: magnetic resonance; PET: positron emission tomography; SPECT: single positron emission CT; TAVI: transcatheter aortic valve implantation; TEE: transoesophageal echocardiography; XRF: single- and bi-plane cine angiography and fluoroscopy.

Table 3: Overview of optimized CBCT scan and contrast infusion protocols used for structural and congenital heart disease interventions.

	Adult		**Pediatric**	
Source	Numburi et al [10]	Balzer et al [11]	Peters et al [12]	Haddad et al [13]
XRF system	Siemens Axiom Artis	Philips Allura FD20	Siemens Artis zee	Toshiba Infinix-I
Scan duration (s)	5	5.2	5	4.1
Frame rate (frames/s)	60	60	30	25
Angular rotation (°)	220	210	200	206
Number of Projections (frames/scan)	235	312	248	-
Tube potential (kV)	Automatic (75-125)	120	Automatic	88 (< 30 kg) & 95 (> 30 kg)
Tube current (mAs)	Automatic (150-692)	Automatic (50-325)	Automatic (mean 118.4±104)	Automatic (25-55)
Detector entrance dose (µGy/X-ray pulse)	0.54	-	-	~0.13-0.22
Contrast infusion site	Aortic root	Left ventricle	Varying	Varying
Iodine concentration (mgI/mL)	370	350	300	-
Total volume (mL/kg) (contrast:saline)	- (~1:1)	0.8 mL/kg (1:1)	- (3:4)	1.6 mL/kg (1:2 for < 30 kg & 2:3 for > 30 kg)
Flow rate (mL/s)	10-15	14	2-14	-
Injection duration (s)	6-8	6	6	5-6
Scan delay (s)	1-2	1	1	1-2
Gating	Ungated	Ungated	Ungated	Ungated
Cardiac rhythm during imaging	RVP (200 bpm)	RVP (200 bpm)	RVP (180+ bpm)	RVP (140-180 bpm)

The protocols are divided in adult and pediatric protocols, respectively focused on TAVI procedures and reducing radiation and contrast levels while maintaining good image quality. Bpm: beats per minute; RVP: rapid ventricular pacing; XRF: single- and bi-plane cine angiography and fluoroscopy.

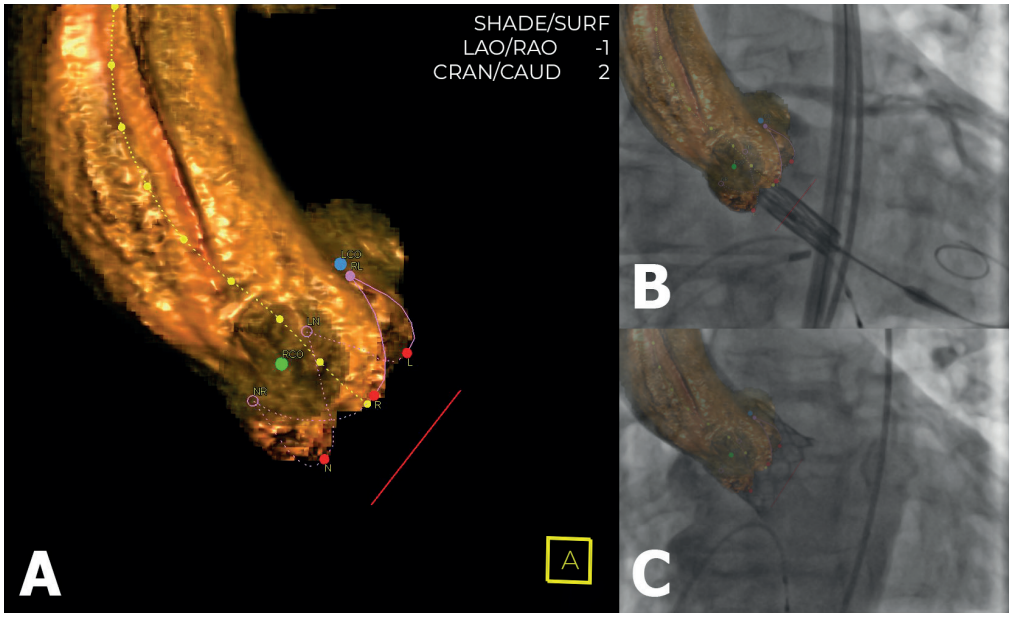

Figure 2: Hybrid imaging during TAVI. A 3D reconstructed DynaCT of the aortic root using Aortic Valve Guide (Siemens Healthineers) shows automatically generated aortic centerline (marked yellow dotted line), a circle of perpendicularity (marked red line), and coronary ostia markers (blue and green markers). **B**-**C** The cusps markers (red dots) and circle of perpendicularity enable accurate prosthesis deployment at the correct annular height.

Types of interventions using HI

Valvular interventions

Challenges in valvular interventions

Percutaneous valvular interventions are challenging due to: 1. prosthesis selection based on accurate measurement of the valve annulus and the out- or inflow tract, which is critical to prevent paravalvular leakage, coronary occlusion, and possibly cardiac arrhythmias.[20] 2. Difficult catheter manipulations with limited manual maneuverability,[21] and 3. Limited intraoperative ability to expand the view from 2D to 3D cardiac anatomy including critical anatomical landmarks, e.g. possibly causing occlusion of adjacent coronary arteries.

Solutions for aortic valve interventions

To overcome the aforementioned issues for TAVI procedures, all major XRF vendors offer commercial TAVI planning software packages (**Table 2**). These software packages can

automatically delineate the aortic root in CT or CBCT images and calculate the aortic valve deployment angles based on the position and orientation of the aortic valve annulus.[22] Markers of the aortic root, left and right coronary ostia are automatically superimposed on the live XRF images, thus facilitating intuitive navigation and maneuvering (**Figure 2**).[22] Furthermore, accurate deployment angles are provided for aortic valve placement.

Different implementations for aortic valve interventions

Aortic Valve Guide software (Siemens Healthineers) has shown to reliably fulfil the functionality and significantly reduce procedure time, radiation exposure and use of contrast using CBCT.[22–25] Consequently, a reduction in peri- and post-interventional complications such as device malpositioning, paravalvular leakage, trauma of surrounding structures as well as other organ damage (acute kidney failure) was shown.[22,24] Excellent implant angles determined by Aortic Valve Guide are significantly more likely to be associated with no paravalvular regurgitation compared to satisfactory or poor implant angles (41.3% vs. 21.6%, respectively, $p = 0.045$) independent of operator experience.[22]

HeartNavigator software (Philips Healthcare) has also shown to provide accurate prosthesis selection, comparable to gold standard CT assessment.[26] In addition, Philips' HeartNavigator has shown to provide accurate planning and guidance to obtain transapical access for amongst others paravalvular leakage repair. However, no significant differences in procedural data, contrast and fluoroscopy time were shown compared to obtaining transapical access without HeartNavigator. Although a trend can be seen in reduced contrast volume and XRF time during procedures where HeartNavigator was used.[27]

The use of HeartVision (GE Healthcare) is well described for endovascular aortic repair but there is no literature available that describes the use in cardiac procedures. From the specifications and intended use, it can be deduced that the functionality of the systems of Siemens and GE Healthcare add a wider range of image integration options compared to HeartNavigator (Philips Healthcare) (**Table 2**). The latter system only allows the integration of CT.

Solutions for mitral valve interventions

Transcatheter mitral valve implantation interventions face similar challenges as TAVI procedures,[30] specific software solutions, however, are lacking. Mitral valve repair by means of MitraClip device (Abbot Vascular, Santa Clara, CA) procedures are performed under XRF guidance and supported by 2D/3D TEE, which is presented in parallel to most often two cardiologists performing the procedure. TEE-XRF fusion optimizes image representation to allow for a fast and clear understanding of the images when TEE and XRF are used in conjunction.

Different implementations for mitral valve interventions

Both Siemens and Philips offer software solutions to integrate live 3D TEE with live XRF (**Table 2**).[8,31] The TEE transducer is automatically tracked in the live XRF images and the 3D echocardiographic images are fused with the XRF images. Demarcations of important soft tissue structures made in the echo images are shown on the live images. Thus allowing accurate assessment for the position of TSP.[32,33] Philips' EchoNavigator guided MitraClip procedures versus conventional TEE-XRF guided MitraClip procedures showed no differences in procedure time and radiation exposure, although a trend towards shorter procedure time was observed.[31,32] Interestingly, EchoNavigator allowed faster placement of two or more clips decreasing the time until the second or third clip by 6 (83.2 ± 27.4 vs. 88.9 ± 29.0 min, p = 0.6) and 60 (134.2 ± 23.2 vs. 199.5 ± 72.8 min, p = 0.4) minutes, respectively.[32]

There is no literature on the use of Siemens' TrueFusion TEE-XRF fusion software in cardiac procedures. From the specifications and intended use, it can be deduced that the functionality of TrueFusion is comparable to EchoNavigator. Both TrueFusion and EchoNavigator require specific echo systems to ensure accurate TEE-XRF fusion imaging (**Table 2**).

Solutions for other heart valves

For the use of HI in the repair/implantation of the other heart valves the available literature is limited. Pre-procedural image fusion during pulmonary valve implantations using VesselNavigator (Philips Healthcare) has shown to significantly reduce the procedure time, radiation exposure, and contrast levels compared to 2D XRF and 3DRA alone.[34] Another

study showed no significant difference in radiation exposure with 3DRA guidance compared to 2D XRF, although a trend of decreased radiation exposure could be seen.[35]

CHD interventions

Challenges in septal defect closures

Septal defect closure with devices are challenging procedures due to: 1. Varying morphology of the septal defect and 2. The number of defects. 3. Prosthesis selection is based on accurate measurement of the septal defect(s).

Solutions for septal defect closures

Percutaneous closure of atrial septal defects has shown to benefit from TEE-XRF fusion by EchoNavigator,[36] the integrated information from TEE enabled catheter and device placement at exactly the intended anatomic location in 81% (n = 21) of the procedures.[31] Furthermore, TEE-XRF significantly decreased both fluoroscopy time and radiation dose. Besides septal defect closures, TSP is a procedural step in e.g. MitraClip placement and left atrial appendage occlusions. EchoNavigator has shown to be a safe method to guide TSP and significantly decreases the duration to perform TSP (18.48 ± 5.62 vs. 23.20 ± 9.61 min, p = 0.006).[37]

Challenges in obstructive lesions

Obstructive lesions such as coarctation of the aorta (CoA) or pulmonary vein stenosis are increasingly treated using a minimally invasive approach. Important for a successful intervention is: 1. accurate 3D imaging of the topographic cardiac surrounding to accurately size the stenosis and 2. avoid occlusion of adjacent vasculature, e.g. carotid or subclavian arteries.

Solutions for obstructive lesions

To overcome these challenges for CoA, integrating 3DRA in the workflow provides important anatomical information and therefore a better understanding of the aortic arch and CoA morphology compared to conventional XRF (**Figure 1 and 3**).[39] Live XRF overlay of the 3D-reconstructed image allows detailed 3D image guidance without a significant increase in procedural duration or radiation exposure.[40,41] Moreover, pre-procedural

imaging can be used for co-registration with XRF and used as roadmaps for live XRF guidance with low registration errors < 4 mm (75%, 21/28 patients).[42,43]

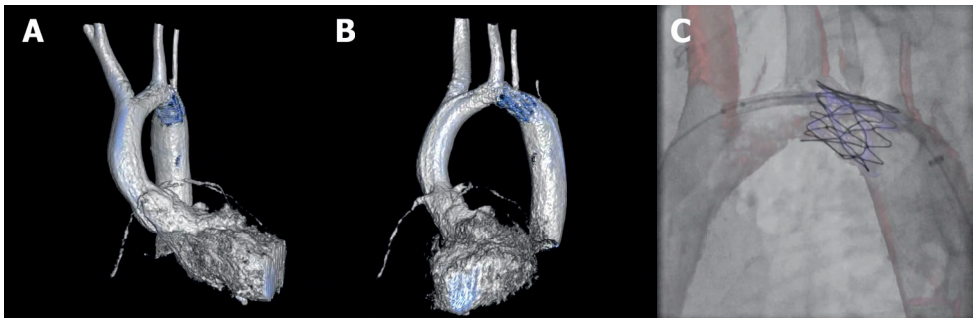

Figure 3: Hybrid imaging during stent placement in a coarctation of the aorta. A-B 3D reconstruction of the left ventricle and aorta (white structure) and stent in the aortic arch (blue structure), respectively shown in the AP and LAO projections. **C** 3D overlay of the aortic arch with the stent in place. The 3D roadmap is used to provide targeted stent placement and avoid obstruction of the left common carotid and left subclavian arteries.

Discussion

Advanced imaging techniques using HI in clinical use is still in its infancy and far from standard in most Cath labs. Current technologies are limited to planning and visualization of anatomy only. The studies included in our review are focused on the impact of hybrid fusion imaging technology on the short-term outcome compared to the multi-modality approach. Available tools have shown a significant decrease in fluoroscopy time, radiation dose, contrast medium use, and in some cases a shorter procedure time is achieved. These procedural outcomes can be directly attributed to the use of hybrid fusion technology. In daily practice, HI solutions can be integrated smoothly into the workflow in the catheterization lab, providing important visualization of 3D cardiac anatomy and surrounding organs. Most studies report on the use of Siemens' Aortic Valve Guide or Philips' EchoNavigator.

Fusion of CBCT or 3DRA with XRF is currently most used for guidance of TAVI's in combination with Siemens' Aortic Valve Guide. The advantage of using CBCT techniques over pre-procedural imaging are the maintained patient position, volume status and

physiology between the time of imaging and intervention.[44] Furthermore, compared to pre-procedural CT, the radiation and contrast exposure of CBCT is significantly lower.[11,22]

TEE-XRF fusion is increasingly used in mitral valve repair and various CHD procedures. The major advantage is the use of real-time fusion of two important imaging modalities. Whereas the use of CBCT is currently limited by static image guidance, TEE-XRF fusion guides the operator by image fusion of dynamic images. Furthermore, the technique offers a solution to the difficulties to interpret and superimpose the images of TEE alongside XRF in the mind of the implanting cardiologist.

Various reports on interventions involving TSP show integration of TEE-XRF in the workflow, resulting in a significant decrease in radiation exposure and fluoroscopy time when guided by Philips' EchoNavigator. Comparable results are shown in other cardiac interventions, in left atrial appendage occlusion up to 52% of total radiation exposure was reduced.[38] Only a trend in decrease of radiation and contrast exposure was observed in MitraClip procedures while, especially in more complex interventions, a larger benefit could be expected.[38] Therefore an interesting observed effect is that the higher the number of MitraClips placed, the shorter the time duration per clip when using Philips' EchoNavigator. Considering that a higher number of clips that are necessary is related to a more complex procedure, the aforementioned observed effect emphasizes the importance of adequate 3D imaging.

Operator experience in hybrid imaging solutions

It can be argued that the beneficial effects when using HI during interventions are less pronounced in experienced teams. The software techniques discussed in this review aim to improve the current clinical workflow, procedural outcomes, and potentially clinical outcomes. Hybrid fusion imaging technologies such as Aortic Valve Guide, automate and standardize the segmentation process and identification of aortic cusps as well as perpendicular valve view. Therefore, upon sufficient image quality, these steps do not have to be performed by the operator, limiting intra- and interobserver variability, potentially providing more reliable procedural outcomes. Siemens' Aortic Valve Guide has shown to significantly more likely provide excellent TAVI implant angles compared to CBCT or XRF alone, independent of operator experience.[22] Several reports described that the learning

curve of TEE-XRF fusion caused an underestimation of the potential beneficial effect. Potentially a larger beneficial effect can be expected when more experience with TEE-XRF is gained.[31,32] Quantification of the effect of operator experience, however, requires studies with larger cohorts.

Institutional costs

All major XRF vendors offer flat-panel detector systems that provide CBCT imaging options as well as pre-procedural image integration (**Table 1**), and market penetration is likely to increase in the future.[9] The institutional costs for these systems range between US$1.2 million and US$5.0 million depending on the vendor, specifications, single or biplane system, and the integration of various advanced imaging modalities such as 3D echocardiography for TEE-XRF fusion.[45] These prices can differ depending on the agreements made between the institution and vendor.

In theory, each XRF system can perform CBCT/3DRA acquisitions independent of the detector size. Larger XRF detectors should be preferred considering more information is acquired during a CBCT acquisition. This is important especially in case a 3D/3D registration with pre-procedural imaging without the need for fiducial markers is required. Moreover, lower costs per examination have been reported in favor of CBCT compared to XRF alone.[46] This can save procedural and healthcare costs.

Other cardiac applications

While the focus in this review is on image-guided SHD and CHD procedures, cardiac interventions involving substrate targeting (e.g. endomyocardial biopsies, regenerative therapy) and/or modification (e.g. electrophysiology, cardiac resynchronization therapy device implantations) could also benefit from interventional planning and image guidance provided by HI (**Figure 4**).[47,48] However, this was considered to be outside the scope of the present manuscript.

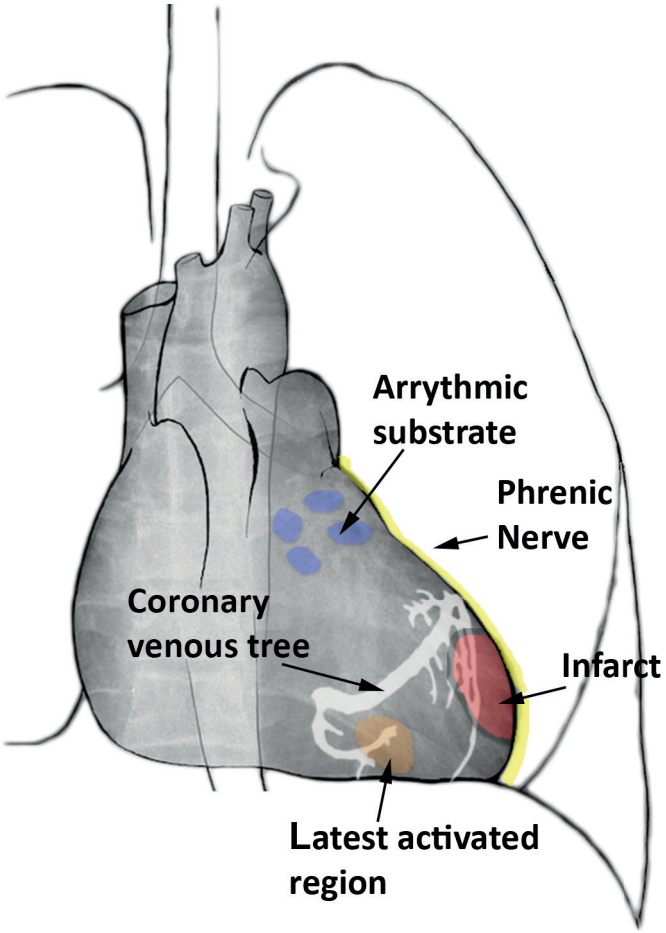

Figure 4: Schematic overview of potential 3D overlay markings onto XRF to guide CRT and electrophysiology cardiac interventions. The blue markings show targets for pulmonary vein isolation. In yellow the phrenic nerve is depicted, passing along the epicardium of the left ventricle. In red an infarcted region is visualized with corresponding border zone marked in black. The orange region is showing the latest activated area along with the coronary venous tree depicted in white.

Future developments

Current fusion imaging software does not provide for motion compensation, specifically cardiac motion. A promising development is 4DRA, which can provide functional assessment of ventricular, valvular and vascular structures. These developments include optimizations of the current cone-beam back projection algorithms to acquire 4D reconstructions that include motion estimation and temporal parameterization by

acquisition time.[49–51] Combinations of 4DRA with quick post-processing to generate 4D reconstructions opens the way for live dynamic 3D roadmaps which could potentially further increase interventional accuracy.

Another interesting HI development are augmented reality (AR) based headsets. AR-based headsets enable projection of multidimensional full-color holograms superimposed on the real world using holographic lenses. An advanced sensor system maps the environment around the user to anchor the holograms to the real world. Using voice commands and hand gestures AR-based headsets are very suitable to be introduced into the catheterization theatre. Potentially providing the cardiologist with additional 3D anatomical information and direct guidance projected on the patient.[52] Besides HI, there is an increased use of 3D printing of cardiac structures for pre-procedural interventional treatment planning.[53]

Limitations

Although the available tools are comprehensive, the literature on the clinical use of the reviewed HI software solutions using XRF systems for cardiac procedures is still limited. Currently available studies are limited by small cohorts and focus on short-term procedural outcomes. Large multicenter studies are necessary to fully evaluate the current technologies and determine the long-term clinical benefits. Nevertheless, this review provides an overview of the tools that are clinically most used in SHD and CHD procedures and provides insight into the future directions for HI.

Conclusion

Major interventional X-ray vendors offer HI software solutions which are safe and can aid the planning and image guidance of cardiovascular interventions. HI integration in SHD and CHD procedures has shown significant decreases in radiation and contrast exposure and complication rate. For visualization of more complex soft tissue characteristics, e.g. needed during cardiac resynchronization therapy device implantations, developments are ongoing and will provide standardized solutions in the future. Even though current HI technologies have limitations, HI provides support in the increasingly complex cardiac interventional procedures to provide better patient care.

Notes

Funding

The research is part of the SmartCare project funded by the TTI transition grant via the government and Top Sector Life Sciences & Health.

References

1. Holmes DR, Mack MJ, Kaul S, Agnihotri A, et al. 2012 ACCF/AATS/SCAI/STS Expert Consensus Document on Transcatheter Aortic Valve Replacement. *J Am Coll Cardiol* 2012;**59**(13):1200–1254. doi:10.1016/j.jacc.2012.01.001.

2. Ooi YK, Kelleman M, Ehrlich A, Glanville M, et al. Transcatheter Versus Surgical Closure of Atrial Septal Defects in Children A Value Comparison. *JACC Cardiovasc Interv* 2016;**9**(1):79–86. doi:10.1016/j.jcin.2015.09.028.

3. Hijazi ZM, Awad SM. Pediatric Cardiac Interventions. *JACC Cardiovasc Interv* 2008;**1**(6):603–611. doi:10.1016/j.jcin.2008.07.007.

4. Takagi H, Ando T, Umemoto T. A review of comparative studies of MitraClip versus surgical repair for mitral regurgitation. *Int J Cardiol* 2017;**228**(June 2016):289–294. doi:10.1016/j.ijcard.2016.11.153.

5. Pantos I, Patatoukas G, Katritsis DG, Efstathopoulos E. Patient radiation doses in interventional cardiology procedures. *Curr Cardiol Rev* 2009;**5**(1):1–11. doi:10.2174/157340309787048059.

6. Voskuil M, Sievert H, Arslan F. Guidance of interventions in structural heart disease; three-dimensional techniques are here to stay. *Netherlands Hear J* 2017;**25**(2):63–64. doi:10.1007/s12471-016-0945-0.

7. Cavalcante JL, Lalude OO, Schoenhagen P, Lerakis S. Cardiovascular Magnetic Resonance Imaging for Structural and Valvular Heart Disease Interventions. *JACC Cardiovasc Interv* 2016;**9**(5):399–425. doi:10.1016/j.jcin.2015.11.031.

8. Thaden JJ, Sanon S, Geske JB, Eleid MF, et al. Echocardiographic and Fluoroscopic Fusion Imaging for Procedural Guidance: An Overview and Early Clinical Experience. *J Am Soc Echocardiogr* 2016;**29**(6):503–512. doi:10.1016/j.echo.2016.01.013.

9. Schwartz JG, Neubauer AM, Fagan TE, Noordhoek NJ, et al. Potential role of three-dimensional rotational angiography and C-arm CT for valvular repair and implantation. *Int J Cardiovasc Imaging* 2011;**27**(8):1205–1222. doi:10.1007/s10554-011-9839-9.

10. Numburi UD, Kapadia SR, Schoenhagen P, Tuzcu EM, et al. Optimization of acquisition and contrast injection protocol for C-arm CT imaging in transcatheter aortic valve implantation: Initial experience in a swine model. *Int J Cardiovasc Imaging* 2013;**29**(2):405–415. doi:10.1007/s10554-012-0075-8.

11. Balzer JC, Boering YC, Mollus S, Schmidt M, et al. Left ventricular contrast injection with rotational C-arm CT improves accuracy of aortic annulus measurement during cardiac catheterisation. *EuroIntervention* 2014;**10**(3):347–354. doi:10.4244/EIJV10I3A60.

12. Peters M, Krings G, Koster M, Molenschot M, et al. Effective radiation dosage of three-dimensional rotational angiography in children. *Europace* 2014;**17**(4):611–616. doi:10.1093/europace/euu207.

13. Haddad L, Waller BR, Johnson J, Choudhri A, et al. Radiation Protocol for Three-Dimensional Rotational Angiography to Limit Procedural Radiation Exposure in the Pediatric Cardiac Catheterization Lab. *Congenit Heart Dis* 2016; doi:10.1111/chd.12356.

14. Buck S De, Alzand BSN, Wielandts JY, Garweg C, et al. Cardiac three-dimensional rotational angiography can be performed with low radiation dose while preserving image quality. *Europace* 2013;**15**(12):1718–1724. doi:10.1093/europace/eut140.

15. Starek Z, Lehar F, Jez J, Wolf J, et al. Periprocedural 3D imaging of the left atrium and esophagus: comparison of different protocols of 3D rotational angiography of the left atrium and esophagus in group of 547 consecutive patients undergoing catheter ablation of the complex atrial arrhythmias. *Int J Cardiovasc Imaging* 2016;1–9. doi:10.1007/s10554-016-0888-y.

16. Eloot L, Bacher K, Steenbeke F, Drieghe B, et al. Three-dimensional rotational X-ray acquisition technique is reducing patients' cancer risk in coronary angiography. *Catheter Cardiovasc Interv* 2013;**82**(4):419–427. doi:10.1002/ccd.24879.

17. Picano E, Vañó E, Rehani MM, Cuocolo A, et al. The appropriate and justified use of medical radiation in cardiovascular imaging: A position document of the ESC Associations of Cardiovascular Imaging, Percutaneous Cardiovascular Interventions and Electrophysiology. *Eur Heart J* 2014;**35**(10):665–672. doi:10.1093/eurheartj/eht394.

18. Glatz AC, Zhu X, Gillespie MJ, Hanna BD, Rome JJ. Use of angiographic CT imaging in the cardiac catheterization laboratory for congenital heart disease. *JACC Cardiovasc Imaging* 2010;**3**(11):1149–1157. doi:10.1016/j.jcmg.2010.09.011.

19. Sinning J-M, Ghanem A, Steinhäuser H, Adenauer V, et al. Renal function as predictor of mortality in patients after percutaneous transcatheter aortic valve implantation. *JACC Cardiovasc Interv* 2010;**3**(11):1141–1149. doi:10.1016/j.jcin.2010.09.009.

20. Jabbour A, Ismail TF, Moat N, Gulati A, et al. Multimodality imaging in transcatheter aortic valve implantation and post-procedural aortic regurgitation: Comparison among cardiovascular magnetic resonance, cardiac computed tomography, and echocardiography. *J Am Coll Cardiol* 2011;**58**(21):2165–2173. doi:10.1016/j.jacc.2011.09.010.

21. Singh GD, Smith TW, Rogers JH. Targeted Transseptal Access for MitraClip Percutaneous Mitral Valve Repair. *Interv Cardiol Clin* 2017;**5**(1):55–69. doi:10.1016/j.iccl.2015.08.005.

22. Poon KK, Crowhurst J, James C, Campbell D, et al. Impact of optimising fluoroscopic implant angles on paravalvular regurgitation in transcatheter aortic valve replacements - Utility of three-dimensional rotational angiography. *EuroIntervention* 2012;**8**(5):538–545. doi:10.4244/EIJV8I5A84.

23. Binder RK, Leipsic J, Wood D, Moore T, et al. Prediction of Optimal Deployment Projection for Transcatheter Aortic Valve Replacement: Angiographic 3-Dimensional Reconstruction of the Aortic Root Versus Multidetector Computed Tomography. *Circ Cardiovasc Interv* 2012;**5**(2):247–252. doi:10.1161/CIRCINTERVENTIONS.111.966531.

24. Samim M, Stella PR, Agostoni P, Kluin J, et al. Automated 3D analysis of pre-procedural MDCT to predict annulus plane angulation and C-arm positioning: Benefit on procedural outcome in patients referred for TAVR. *JACC Cardiovasc Imaging* 2013;**6**(2):238–248. doi:10.1016/j.jcmg.2012.12.004.

25. linden A van, Kempfert J, Blumenstein J, Möllmann H, et al. Manual versus automatic detection of aortic annulus plane in a computed tomography scan for transcatheter aortic valve implantation screening. *Eur J Cardio-thoracic Surg* 2014;**46**(2):207–212. doi:10.1093/ejcts/ezt600.

26. Vaitkus PT, Wang DD, Greenbaum A, Guerrero M, O'Neill W. Assessment of a novel software tool in the selection of aortic valve prosthesis size for transcatheter aortic valve replacement. *J Invasive Cardiol* 2014;**26**(7):328–332.

27. Kliger C, Jelnin V, Sharma S, Panagopoulos G, et al. CT angiography-fluoroscopy fusion imaging for percutaneous transapical access. *JACC Cardiovasc Imaging* 2014;**7**(2):169–177. doi:10.1016/j.jcmg.2013.10.009.

28. Stortecky S, Heg D, Gloekler S, Wenaweser P, et al. Accuracy and reproducibility of aortic annulus sizing using a dedicated three-dimensional computed tomography reconstruction tool in patients evaluated for transcatheter aortic valve replacement. *EuroIntervention* 2014;**10**(3):339–346. doi:DOI: 10.4244/EIJV10I3A59.

29. Mieghem NM Van, Rodriguez-Olivares R, C. Ren BC Ben, Gils L Van, et al. Computed tomography optimised fluoroscopy guidance for transcatheter mitral therapies. *EuroIntervention* 2016;**11**(12):1428–1431. doi:DOI: 10.4244/EIJV11I12A273.

30. Blanke P, Dvir D, Naoum C, Cheung A, et al. Prediction of fluoroscopic angulation and coronary sinus location by CT in the context of transcatheter mitral valve implantation. *J Cardiovasc Comput Tomogr* 2015;**9**(3):183–192. doi:10.1016/j.jcct.2015.02.007.

31. Jone P-N, Ross MM, Bracken JA, Mulvahill MJ, et al. Feasibility and Safety of Using a Fused Echocardiography/Fluoroscopy Imaging System in Patients with Congenital Heart Disease. *J Am Soc Echocardiogr* 2016;**29**(6):513–521. doi:10.1016/j.echo.2016.03.014.

32. Sündermann SH, Biaggi P, Grünenfelder J, Gessat M, et al. Safety and feasibility of novel technology fusing echocardiography and fluoroscopy images during MitraClip interventions. *EuroIntervention* 2014;**9**(10):1210–1216. doi:10.4244/EIJV9I10A203.

33. Quaife RA, Salcedo EE, Carroll JD. Procedural Guidance Using Advance Imaging Techniques for Percutaneous Edge-to-Edge Mitral Valve Repair. *Curr Cardiol Rep* 2014;**16**(2):452. doi:10.1007/s11886-013-0452-5.

34. Goreczny S, Moszura T, Dryzek P, Lukaszewski M, et al. Three-dimensional image fusion guidance of percutaneous pulmonary valve implantation to reduce radiation exposure and contrast dose: A comparison with traditional two-dimensional and three-dimensional rotational angiographic guidance. *Netherlands Hear J* 2016; doi:10.1007/s12471-016-0941-4.

35. Nguyen HH, Balzer DT, Murphy JJ, Nicolas R, Shahanavaz S. Radiation Exposure by Three-Dimensional Rotational Angiography (3DRA) During Trans-catheter Melody Pulmonary Valve Procedures (TMPV) in a Pediatric Cardiac Catheterization Laboratory. *Pediatr Cardiol* 2016; doi:10.1007/s00246-016-1453-0.

36. Faletra FF, Biasco L, Pedrazzini G, Moccetti M, et al. Echocardiographic-Fluoroscopic Fusion Imaging in Transseptal Puncture: A New Technology for an Old Procedure. *J Am Soc Echocardiogr* 2017;**30**(9):886–895. doi:10.1016/j.echo.2017.05.001.

37. Afzal S, Veulemans V, Balzer J, Rassaf T, et al. Safety and efficacy of transseptal puncture guided by real-time fusion of echocardiography and fluoroscopy. *Netherlands Hear J* 2017;**25**(2):131–136. doi:10.1007/s12471-016-0937-0.

38. Jungen C, Zeus T, Balzer J, Eickholt C, et al. Left atrial appendage closure guided by integrated echocardiography and fluoroscopy imaging reduces radiation exposure. *PLoS One* 2015;**10**(10):1–13. doi:10.1371/journal.pone.0140386.

39. Berman DP, Khan DM, Gutierrez Y, Zahn EM. The use of three-dimensional rotational angiography to assess the pulmonary circulation following cavo-pulmonary connection in patients with single ventricle. *Catheter Cardiovasc Interv* 2012;**80**(6):922–930. doi:10.1002/ccd.23461.

40. Starmans NLP, Krings GJ, Molenschot MMC, Stelt F van der, Breur JMPJ. Three-dimensional rotational angiography in children with an aortic coarctation. *Netherlands Hear J* 2016; doi:10.1007/s12471-016-0899-2.

41. Stenger A, Dittrich S, Glöckler M. Three-Dimensional Rotational Angiography in the Pediatric Cath Lab: Optimizing Aortic Interventions. *Pediatr Cardiol* 2016;**37**(3):528–536. doi:10.1007/s00246-015-1310-6.

42. Goreczny S, Dryzek P, Morgan GJ, Lukaszewski M, et al. Novel Three-Dimensional Image Fusion Software to Facilitate Guidance of Complex Cardiac Catheterization 3D image fusion for interventions in CHD. *Pediatr Cardiol* 2017;**38**(6):1133–1142. doi:10.1007/s00246-017-1627-4.

43. Suntharos P, Setser RM, Bradley-Skelton S, Prieto LR. Real-time three dimensional CT and MRI to guide interventions for congenital heart disease and acquired pulmonary vein stenosis. *Int J Cardiovasc Imaging* 2017;**33**(10):1619–1626. doi:10.1007/s10554-017-1151-x.

44. Noseworthy PA, Malchano ZJ, Ahmed J, Holmvang G, et al. The impact of respiration on left atrial and pulmonary venous anatomy: Implications for image-guided intervention. *Hear Rhythm* 2005;**2**(11):1173–1178. doi:10.1016/j.hrthm.2005.08.008.

45. Kpodonu J. Hybrid Cardiovascular Suite: The Operating Room of the Future. *J Card Surg* 2010;**25**(6):704–709. doi:10.1111/j.1540-8191.2010.01111.x.

46. Kriatselis C, Nedios S, Akrivakis S, Tang M, et al. Intraprocedural imaging of left atrium and pulmonary veins: A comparison study between rotational angiography and cardiac computed tomography. *PACE - Pacing Clin Electrophysiol* 2011;**34**(3):315–322. doi:10.1111/j.1540-8159.2010.02969.x.

47. Rogers T, Ratnayaka K, Karmarkar P, Campbell-Washburn AE, et al. Real-Time Magnetic Resonance Imaging Guidance Improves the Diagnostic Yield of Endomyocardial Biopsy. *JACC Basic to Transl Sci* 2016;**1**(5):376–383. doi:10.1016/j.jacbts.2016.05.007.

48. Behar JM, Rajani R, Rinaldi CA. Guided left ventricular lead placement for cardiac resynchronization therapy: an opportunity for image integration. *Eur J Heart Fail* 2017;**19**(3):435–435. doi:10.1002/ejhf.716.

49. Mory C, Auvray V, Zhang B, Grass M, et al. Cardiac C-arm computed tomography using a 3D + time ROI reconstruction method with spatial and temporal regularization. *Med Phys* 2014;**41**(2):21903. doi:10.1118/1.4860215.

50. Wielandts J-Y, Buck S De, Michielsen K, Louw R, et al. Multi-phase rotational angiography of the left ventricle to assist ablations: feasibility and accuracy of novel imaging. *Eur Hear J – Cardiovasc Imaging* 2016;**17**(2):162–168. doi:10.1093/ehjci/jev120.

51. Taubmann O, Haase V, Lauritsch G, Zheng Y, et al. Assessing cardiac function from total-variation-regularized 4D C-arm CT in the presence of angular undersampling. *Phys Med Biol* 2017;**62**(7):2762–2777. doi:10.1088/1361-6560/aa6241.

52. Kuhlemann I, Kleemann M, Jauer P, Schweikard A, Ernst F. Towards X-ray free endovascular interventions – using HoloLens for on-line holographic visualisation. *Healthc Technol Lett* 2017;**4**:184–187. doi:10.1049/htl.2017.0061.

53. Meier LM, Meineri M, Qua Hiansen J, Horlick EM. Structural and congenital heart disease interventions: the role of three-dimensional printing. *Netherlands Hear J* 2017;**25**(2):65–75. doi:10.1007/s12471-016-0942-3.

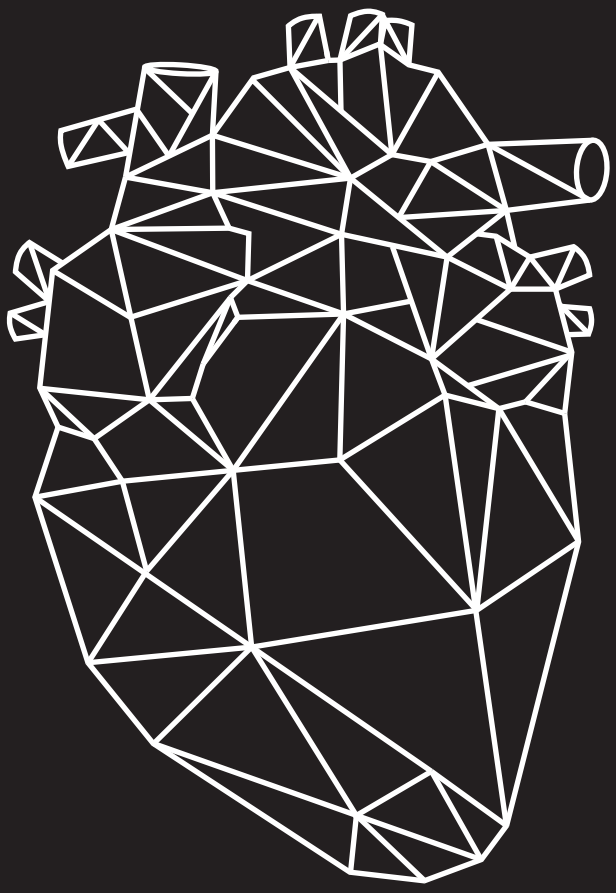

Chapter 3

3D Whole-Heart Myocardial Tissue Analysis

Journal of Visualized Experiments, 2017, (122), e54974, doi:10.3791/54974

HT. van den Broek MSc [1], L. de Jong BSc [1,2], P.A. Doevendans MD PhD [1], S.A.J. Chamuleau MD PhD [1], F.J. van Slochteren PhD *[1], R. van Es PhD *[1]
* These authors contributed equally

[1] Department of Cardiology, University Medical Center Utrecht, Utrecht, The Netherlands
[2] MIRA Institute, University Twente, Enschede, The Netherlands

Abstract

Cardiac regenerative therapies aim to protect and repair the injured heart in patients with ischemic heart disease. By injecting stem cells or other biologicals that enhance angio- or vasculogenesis into the infarct border zone (IBZ), tissue perfusion is improved, and the myocardium can be protected from further damage. For maximum therapeutic effect, it is hypothesized that the regenerative substance is best delivered to the IBZ. This requires accurate injections and has led to the development of new injection techniques. To validate these new techniques, we have designed a validation protocol based on myocardial tissue analysis. This protocol includes whole-heart myocardial tissue processing that enables detailed two-dimensional (2D) and three-dimensional (3D) analysis of the cardiac anatomy and intramyocardial injections. In a pig, myocardial infarction was created by a 90-min occlusion of the left anterior descending coronary artery. Four weeks later, a mixture of a hydrogel with superparamagnetic iron oxide particles (SPIOs) and fluorescent beads was injected in the IBZ using a minimally-invasive endocardial approach. 1 h after the injection procedure, the pig was euthanized, and the heart was excised and embedded in agarose (agar). After the solidification of the agar, magnetic resonance imaging (MRI), slicing of the heart, and fluorescence imaging were performed. After image post-processing, the 3D analysis was performed to assess the IBZ targeting accuracy. This protocol provides a structured and reproducible method for the assessment of the targeting accuracy of intramyocardial injections into the IBZ. The protocol can be easily used when the processing of scar tissue and/or validation of the injection accuracy of the whole heart is desired.

Introduction

Ischemic heart disease has been the world's leading cause of death for the past decades.[1] Acute treatment after myocardial infarction aims to restore blood flow to the myocardium via percutaneous coronary intervention or coronary artery bypass grafting. In severe infarctions, a large area of the myocardium is scarred, and these cases often result in ischemic heart failure (HF).[2] Current treatment options for HF focus on prevention and the preservation of cardiac function for the HF patients, but not on regeneration.

In the last decade, cardiac regenerative therapies have been investigated as a treatment option for HF.[3] This therapy aims to deliver biologicals, such as stem cells or growth factors, directly to the injured myocardium to induce revascularization, cardiomyocyte protection, differentiation, and growth.[4] For optimal therapeutic effect, it is hypothesized that the biological must be injected in the infarct border zone (IBZ) to facilitate good tissue perfusion for the survival of the biological and for the optimal effect to the target zone.[5,6] Multiple techniques have been developed to perform identification and visualization of the IBZ to guide intramyocardial injections.[7–11] Besides identification and visualization of the IBZ, the delivery also relies on the biomaterials and injection catheters used. To validate the injection accuracy of the delivery techniques, an accurate and reproducible quantification method is required.

We have developed a protocol for whole-heart myocardial tissue processing that offers two-dimensional (2D) and three-dimensional (3D) imaging, which can be used for qualitative and quantitative study aims. The protocol covers the embedding process and the digital image analysis. In this paper, we demonstrate a protocol for the assessment of the targeting accuracy of intramyocardial injections in the IBZ in a large porcine model of chronic myocardial infarction.

Protocol

The *in vivo* experiment was conducted in accordance with the Guide for the Care and Use of Laboratory Animals prepared by the Institute of Laboratory Animal Research. The experiment was approved by the local Animal Experiments Committee.

1. Preparation of injectable and embedding solution

1. Prepare the injectable gel.
    1. Prepare 1 mL of ureido-pyrimidinone (UPy) gel in accordance to previously-described protocols.[12,13]
    2. Add superparamagnetic iron oxide particles (SPIOs) to the solution to get a concentration of 15 µg/mL and stir the mixture for 5 min for uniform distribution.
    3. Add the fluorescent microbeads to the solution to get a concentration of 10,000 beads/mL and stir the mixture for 5 min for uniform distribution.
    4. Store the resulting mixture at room temperature in a dark environment. Warm and vortex or stir the solution shortly before the injection procedure.

2. Prepare the embedding solution.
    1. Start with tap water at room temperature and add agarose (agar) to a concentration of 4 wt%.
    2. Slowly heat up the solution to the boiling point using a microwave oven and stir frequently during heating. Upon reaching the boiling point, store and keep the agar solution above 70 °C for 2 h to allow trapped air to surface.
    3. Allow the agar to cool down at room temperature to a temperature between 50 and 60 °C until the time of embedding.

2. Injection procedure

1. Perform premedication (anti-arrhythmic agents, anti-platelet therapy, and pain medication), anesthesia, venous access, and intubation, as previously described.[14]

2. Perform injections using an intramyocardial injection catheter (**Table of Materials**). For each injection, 0.2 mL of the mixture is injected in one bolus at a constant rate of approximately 0.3 mL/min using an injection device. Place the injections at different positions along the IBZ.[12]
3. Administer 0.2 mL/kg (1.0 mmol/mL) of a gadolinium-based contrast agent 15 min prior to euthanizing the animal.
4. Administer 20 mL of 7.5% potassium chloride intravenously to euthanize the animal.
5. Secure mediastinal access following protocol steps 8.2-8.3, as described by Koudstaal *et al.*[14] Cut the inferior caval vein 5 cm from the right atrium and remove outflowing blood with a suction device. Excise the heart and rinse it with 0.9% saline at room temperature.

3. Embedding procedure

1. Prepare the heart.
    1. Remove the pericardium from the heart while keeping the atria and ventricles intact. Dissect the ascending aorta ±1 cm above the aortic valve using Klinkenberg scissors. Cut the inferior caval vein ±1 cm from the atrium, and do the same for the pulmonary veins.
    2. Suture the apex of the heart to the bottom of a plastic embedding container (17x15x15 cm, WxDxH) using a 2-0 suture to prevent floatation of the heart during embedding (**Figure 1A**).
    3. Suture the remaining part of the aorta to the rims of the container using 2-0, making sure that the heart is centered and not touching the walls of the container (**Figure 1B**).

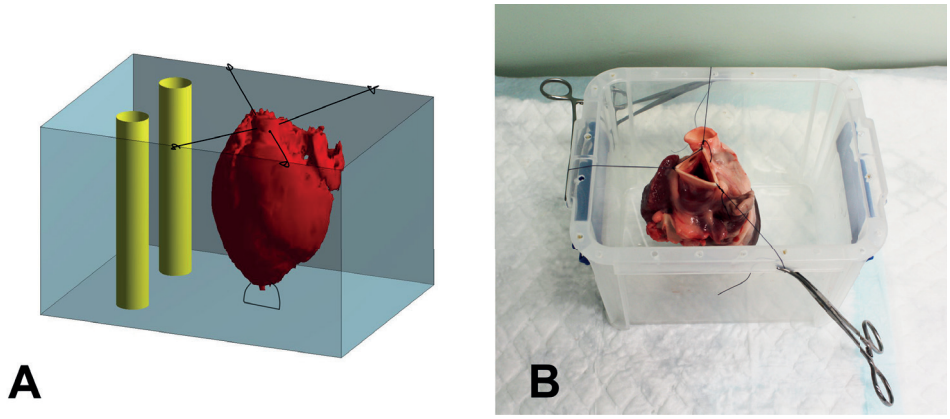

Figure 1: Schematic overview and photograph of the embedding container. (**A**) Schematic overview of the embedding process. The heart (red) is secured in the container (blue) using sutures. After filling the heart with the agar solution, the space around the heart is filled. Finally, two rigid plastic tubes (yellow) are positioned in the container, next to but not touching the heart, to serve as a reference during image registration. (**B**) Photograph of a heart secured in the embedding container. The sutures are clamped to the rim of the container using mosquito clamps.

2. Embed the heart in an end-diastolic-like geometry.

   NOTE: The prevention of air bubble creation is necessary. If large air bubbles present in the agar solution, keep the agar at 40 °C, allowing the air bubbles to surface.

   1. Clamp the inferior caval vein using mosquito clamps. Slowly inject the liquid agar using a 50-mL syringe in the right atrium via the superior caval vein until both the right atrium and ventricle are completely filled.
   2. Clamp the pulmonary veins using mosquito clamps. Gently pass an agar-filled 50-mL syringe retrogradely through the aortic valves. Slowly inject the solution in the left ventricle (LV) until the LV and the left atrium are completely filled. After filling the LV, clamp the aorta to keep the agar in the LV.

3. Pour the remaining agar into the container until the heart is fully covered. Place two rigid plastic tubes within the embedding container to serve as reference structures for later image registration (**Figure 1A**). Make sure the tubes do not touch the walls of the container or the heart.
4. Let the agar solidify at 2-7 °C.

4. Image acquisition

1. Perform transversal *ex vivo* MRI scans of the heart that is embedded in the container.
    1. Place the container with the embedded heart inside a head coil (**Table of Materials**).
    2. Angulate the slices parallel to the bottom of the container. Use the same orientation and angulation in each *ex vivo* MRI sequence.
    3. To visualize myocardium, perform a fluid-attenuated inverse recovery (FLAIR) sequence with the following parameters: repetition time [TR]/echo time [TE] = 10 s/140 ms, flip angle = 90°, pixel size = 0.5 x 0.5 mm, field of view [FOV] = 169 x 169 mm, 320 x 320 matrix, and 3 mm slice thickness.
    4. To visualize the myocardial infarction, perform a late-gadolinium enhanced (LGE) sequence with the following parameters: [TR]/[TE] = 5.53 ms/1.69 ms, flip angle = 25°, pixel size = 1.0 x 1.0 mm, [FOV] = 169 x 169 mm, 176 x 176 matrix, and 3 mm slice thickness.
    5. To visualize SPIOs, perform a T2*-weighted gradient echo sequence with the following parameters: [TR]/[TE] = 88.7 ms/15 equally-distributed TEs with a range of 1.9-24.6 ms, flip angle = 15°, pixel size = 0.5 x 0.5 mm, [FOV] = 169 x 169 mm, 320 x 320 matrix, and 3 mm slice thickness.

2. Tissue processing
    1. Turn the container upside down and allow air between the agar and the sides of the container to remove the solid agar solution, including the heart, from the container. Remove the plastic rods from the solid agar.
    2. Section the agar block containing the heart in 5-mm slices from the apex to the base of the heart using a meat slicer. Keep the angulation of the cut slices the same as in the acquired MR images by cutting parallel to the bottom of the agar block.
    3. Stain the agar slices (including the heart) for 15 min in 1 wt% of 2,3,5-triphenyltetrazoliumchloride (TTC) dissolved in 0.9% saline at 37 °C, and photograph the slices on both sides from a perpendicular view (**Figure 2A**). Next, carefully rinse the slices in 0.9% saline.

        NOTE: In this study, we used a dSLR setup with an appropriate lens/objective, a tripod, and uniform lighting. However, the photographs served only as a control for the assessment of the scar region, so we could have used a different setup.

3. Fluorescence imaging

    NOTE: Depending on the excitation and emission wavelengths of the fluorescent microbeads, select the appropriate filter block and excitation lasers (*e.g.,* the red microbeads used here have excitation and emission wavelengths of 580 nm and 605 nm, respectively; therefore, the selected excitation laser and bandpass filters were set to 532 nm, 580/30 nm and 610/30 nm, respectively).

    1. Select fluorescence-mode imaging on the variable-mode scanner. Set the photomultiplier tube to 430 V or equivalent and the pixel size to 100 x 100 µm. Select an excitation laser (532 nm) closest to the excitation wavelength of the fluorescent microbeads.

2. For the first filter block, select a bandpass filter (580/30 nm) that overlaps with the emission wavelength of the injected fluorescence beads (channel 1). Select a bandpass filter for the second filter block (610/30) outside the emission wavelength (channel 2).

   NOTE: The second filter block serves as a negative control and to remove auto-fluorescence while keeping the injection sites intact.

3. Scan both sides of the agar slices in the fluorescence mode of the variable-mode laser scanner using the two channels. Make sure that each slice is completely scanned, including the reference holes.

5. Post-processing

NOTE: The first step in image post-processing is the manual segmentation of the myocardium using in-house developed scripts to trace the endo- and epicardial borders, as well as the injection sites. This is the same for both MRI and fluorescence scans.

1. Segment the myocardium in the MRI scans.
   1. Segment the endocardial and epicardial LV borders on the FLAIR MRI sequence images.
   2. Copy the LV segmentation from step 5.1.1 to the LGE-MRI dataset and segment the scar on the LGE MRI sequence.
   3. Copy the myocardium segmentation from step 5.1.1 to the T2*-weighted dataset and segment the SPIO depositions in the LV myocardium.
2. Process the fluorescence images and perform segmentations.
   1. Load the files obtained from the variable-mode scanner and make a separate image of each cross-sectional heart slice.
   2. Flip the slices that were scanned in base to apex orientation and sort the fluorescence images into a stack for both channels that is oriented from apex to base.

3. Segment the endocardial and epicardial LV borders on the fluorescence images.
4. Segment the scar manually on the fluorescence images and use the LGE-MRI scan and the photographs to confirm scar morphology.
5. Subtract the image stack of channel 2 from the image stack of channel 1 to exclude auto-fluorescence. Manually segment the fluorescent microbead depositions and use the T2* images for confirmation.

3. To create an anatomically-correct 3D geometry, perform a rigid registration of the slices in the image stack based on the reference structures (the holes created by the rigid tubes). Calculate and store the applied translation and rotation of each image.

4. Apply the stored transformations to the image stacks and the segmentations. Linearly interpolate the segmentations of both sides of the slices to reconstruct the original slice thickness and to create a 3D model of the data.

6. Analysis

1. Perform 2D and/or 3D measurements of the distance between the centres of the injection sites and the IBZ to assess the injection accuracy. Measure the distance along the endocardial border of the LV segmentation. In **Figure 2C** and **2F**, an example of the 2D and 3D measurements is indicated by the red line.

Representative results

Tissue embedding

Through the embedding process, an end-diastolic-like geometry was established. The agar successfully adhered to the heart tissue, enabling the tissue to be sliced at the desired angulation with equal slice thicknesses (**Figure 2A** and **2C**).

Scar- and injection-site assessment

For each imaging modality, infarct and injection location assessments were performed successfully. In both 2D fluorescence imaging and MRI imaging, the scar and injection sites were clearly distinct (**Figure 2C**, **2D**, and **2E**, respectively)**.** Photographs of the TTC-stained tissue and LGE-MRI images provide a control for scar assessment in fluorescence imaging (**Figure 2A** and **2C**).

3D reconstruction

The reference markers provide an accurate and reliable method for image registration. Image post-processing enables the reconstruction of the 3D geometry of the *ex vivo* heart based on the segmentations and the fluorescent images of the heart (**Figure 2F**). The 3D geometry of the segmentations allows for an accurate 3D injection accuracy assessment (**Figure 2F**).

Measurements

In this study, the injection depositions and IBZ were projected onto the endocardial wall. Afterwards, the distances between the projections on the endocardial surface were measured (**Figure 2C** and **2F**). The high-resolution (0.1 x 0.1 mm) fluorescent images allowed accurate measurements. In the 3D reconstruction, the resolution in the z-direction due to the slice thickness was 2.5 mm.

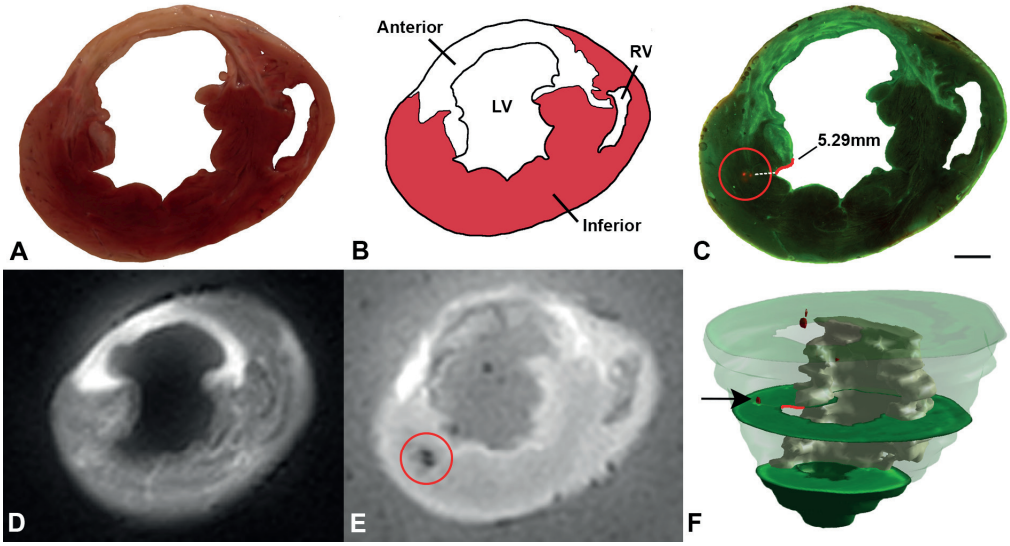

Figure 2: Typical *ex vivo* imaging data and 3D reconstruction. The resulting images acquired by the different modalities used in this protocol. All images show the same transverse slice of the embedded heart. **A** Photograph of the TTC-stained slice in which the scar is visible. **B** Schematic overview of the anatomical structures. **C** Fluorescence image with both channels combined. The channel covering the bead emission spectrum is shown in red and the negative control is shown in green. The red circle indicates the injection site. The distance measurement from the injection to the IBZ is indicated with the red line. **D** Short-axis LGE-MRI; the infarct area is shown as a hyper-intense white area. **E** T2*-weighted MRI; the SPIO particles within the injected substance can be recognized as the local signal void indicated by the red circle. **F** 3D visualization of injection sites (red), scar tissue (white), and myocardium (green) as segmented in the fluorescent images. The arrow indicates the same injection spot as in **C** and **E**. In this image, the same distance measurement is indicated with the red line. LV = Left Ventricle, RV = Right Ventricle. The scale bar represents 10 mm.

Discussion

Whole-heart 3D myocardial tissue processing according to this protocol provides a structured method that enables the 3D analysis of the infarct, the IBZ, and the performed injections with respect to the cardiac anatomy. The filling volume of the heart depends on the desired analysis. In this study, to assess the injection accuracy, we aimed to fill the heart to resemble the end-diastolic geometry as close as possible. To enforce this, the LV apex is fixed to the bottom of the container and the LV is filled with agar while the pulmonary veins are clamped. When the LV is filled, the aorta is clamped as well, preventing the agar from flowing out of the LV and imitating the end-diastolic geometry as close as possible.

Sectioning the embedded heart offers the benefit of uniform slice thickness and allows the slices to be in the same angulation as in *ex vivo* imaging. After slicing, the embedding material prevents the tissue from deformation caused by the handling of the slices during image acquisition. Ideally, TTC staining should be performed as soon as possible after removal from the body, as the staining relies on enzymes to differentiate between metabolically-active and -inactive tissues. In our protocol, however, there are several important steps that must be performed before the TTC staining can take place, including the embedding process, in which the embedded heart is cooled to solidify the agar. Since we have observed clear staining of the infarcted tissue in all slices, we believe that this effect was minimal.

The imaging equipment used here can be replaced by different equipment that provides the same functionality. High-resolution fluorescence imaging on a variable-mode laser scanner and the option to set multiple filter blocks in order to effectively and accurately process the tissue are essential for detailed analysis. For image post-processing, software packages that allow full freedom to perform image analysis are required. In our experience, 3D analysis for the assessment of the injection accuracy was used, but analysis on the 2D images is also possible.

We have thus far performed this myocardial tissue processing method in 10 pigs and have been able to find 73% of the injection sites of in a total of 118 performed injections. The difference between the number of injections performed and the amount of identified injection sites is possibly caused by the difference between the 5-mm slice thickness and the 1.5-mm penetration depth of the fluorescence scanner. Theoretically, 2 mm of tissue is not measured in each slice. Thinner slices would solve this problem.

Limitations

Despite the end-diastolic-like geometry at the start of the embedding process, some hearts appeared to have contracted a little in the agar. Since we observed no large deviations from the end-diastolic volume, we believe that this effect was minimal and did not affect the injection accuracy assessment. Using thinner tissue slices would improve the accuracy of the assessment and allow for a more detailed comparison with *ex vivo* MRI. Another option

would be to use NIRF agents instead of fluorescent microbeads to improve the penetration depth and possibly-detected fraction. Furthermore, the low temperature of the embedded heart and the timing of the TTC staining might cause a lack of the enzymes that are necessary for this type of staining. Nevertheless, the photographs of the stained slices proved to be a good control for scar assessment.

Future perspectives

Although this method was originally designed for accuracy assessments of intramyocardial injections, studies with other endpoints can also benefit from this method (*e.g.,* infarct size, morphology assessment, or other organs). In addition to MRI, other 3D imaging modalities, such as CT, PET, or SPECT, can be used on the myocardial tissue following the demonstrated methodology. In addition, the integration of these different imaging modalities could possibly further optimize the 2D and 3D analyses.

Conclusion

To conclude, we have provided a novel, standardized, and reproducible method to perform 3D whole-heart myocardial tissue processing. Agar has proven to be a suitable medium for whole-heart embedding, enabling the tissue to be sliced at the desired angulation and with equal thickness. Moreover, the image registration proved feasible for the 3D reconstruction of myocardial imaging, enabling 3D assessment at a high spatial resolution, which can be used for qualitative and quantitative study aims.

Notes

Acknowledgements

The authors would like to thank Marlijn Jansen, Joyce Visser, and Martijn van Nieuwburg for their assistance with the animal experiments. We greatly acknowledge Martijn Froeling and Anke Wassink for their assistance with the MRI imaging.

References

1. Nowbar, A. N., Howard, J. P., Finegold, J. a, Asaria, P. & Francis, D. P. 2014 global geographic analysis of mortality from ischaemic heart disease by country, age and income: statistics from World Health Organisation and United Nations. *Int J Cardiol.* **174** (2), 293–8, doi:10.1016/j.ijcard.2014.04.096, (2014).

2. Kannel, W. B. & Belanger, A. J. Epidemiology of heart failure. *Am Heart J.* **121** (3), 951–957, doi:10.1016/0002-8703(91)90225-7, (1991).

3. Ibáñez, B., Heusch, G., Ovize, M. & Van De Werf, F. Evolving therapies for myocardial ischemia/reperfusion injury. *J Am Coll Cardiol.* **65** (14), 1454–1471, doi:10.1016/j.jacc.2015.02.032, (2015).

4. Bartunek, J., Vanderheyden, M., Hill, J. & Terzic, A. Cells as biologics for cardiac repair in ischaemic heart failure. *Heart.* **96** (10), 792–800, doi:10.1136/hrt.2007.139394 , (2010).

5. Orlic, D., Kajstura, J., *et al.* Bone marrow cells regenerate infarcted myocardium. *Nature.* **410** (6829), 701–705, doi:10.1038/35070587, (2001).

6. Nguyen, P. K., Lan, F., Wang, Y. & Wu, J. C. Imaging: Guiding the Clinical Translation of Cardiac Stem Cell Therapy. *Circ Res.* **109** (8), 962–979, doi: 10.1161/CIRCRESAHA.111.242909, (2011).

7. Psaltis, P. J. & Worthley, S. G. Endoventricular electromechanical mapping-the diagnostic and therapeutic utility of the NOGA XP Cardiac Navigation System. *J Cardiovasc Transl Res.* **2**, (1), 48–62, doi:10.1007/s12265-008-9080-7, (2009).

8. Tomkowiak, M. T., Klein, A. J., *et al.* Targeted transendocardial therapeutic delivery guided by MRI-x-ray image fusion. *Catheter Cardiovasc Interv.* **78** (3), 468–78, doi:10.1002/ccd.22901, (2011).

9. Dauwe, D. F., Nuyens, D., *et al.* Three-dimensional rotational angiography fused with multimodal imaging modalities for targeted endomyocardial injections in the ischaemic heart. *Eur Heart J Cardiovasc Imaging.* **15** (8), 900-7, doi:10.1093/ehjci/jeu019 , (2014).

10. van Slochteren, F. J., van Es, R., *et al.* Multimodality infarct identification for optimal image-guided intramyocardial cell injections. *Neth Heart J.* **22** (11), 493–500, doi:10.1007/s12471-014-0604-2, (2014).

11. Slochteren, F. J., Es, R., *et al.* Three dimensional fusion of electromechanical mapping and magnetic resonance imaging for real-time navigation of intramyocardial cell injections in a porcine model of chronic myocardial infarction. *Int J Cardiovasc Imaging.* **32** (5), 833-43, doi:10.1007/s10554-016-0852-x, (2016).

12. Pape, a. C. H., Bakker, M. H., *et al.* An Injectable and Drug-loaded Supramolecular Hydrogel for Local Catheter Injection into the Pig Heart. *J Vis Exp.* (100), doi:10.3791/52450, (2015).

13. Bastings, M. M. C., Koudstaal, S., *et al.* A fast pH-switchable and self-healing supramolecular hydrogel carrier for guided, local catheter injection in the infarcted myocardium. *Adv Healthc Mater.* **3** (1), 70–78, doi: 10.1002/adhm.201300076, (2014).

14. Koudstaal, S., Jansen of Lorkeers, S. J., *et al.* Myocardial infarction and functional outcome assessment in pigs. *J. Vis. Exp.* (86), doi:10.3791/51269, (2014).

Supplementary Data

Table of materials

Name of Material/ Equipment	Company	Comments/Description
0.9% Saline	Braun	
Agarose	Roche Diagnostics	Scientific grade multipurpose agar
Biomolecular fluorescence scanner Typhoon 9410	GE Healthcare	
Embedding container		Plastic, dimensions 17 x 14,5 x 14 cm
FluoSpheres Polystyrene Microspheres	Invitrogen	Red, 10 µm
Gadolinium	Gadovist	1,0 mmol/mL
dS 32 channel head coil	Philips	Or similar
Matlab	Mathworks	To insure compatibility 2015a or newer
Meat slicer	Berkel	
Myostar injection catheter	Biosense Webster	
Super paramagnetic iron oxide particles	Sinerem	
Triphenyl-tetrazolium chloride	Merck	
UPy-PEG10k		
Vicryl 2-0	Ethicon	

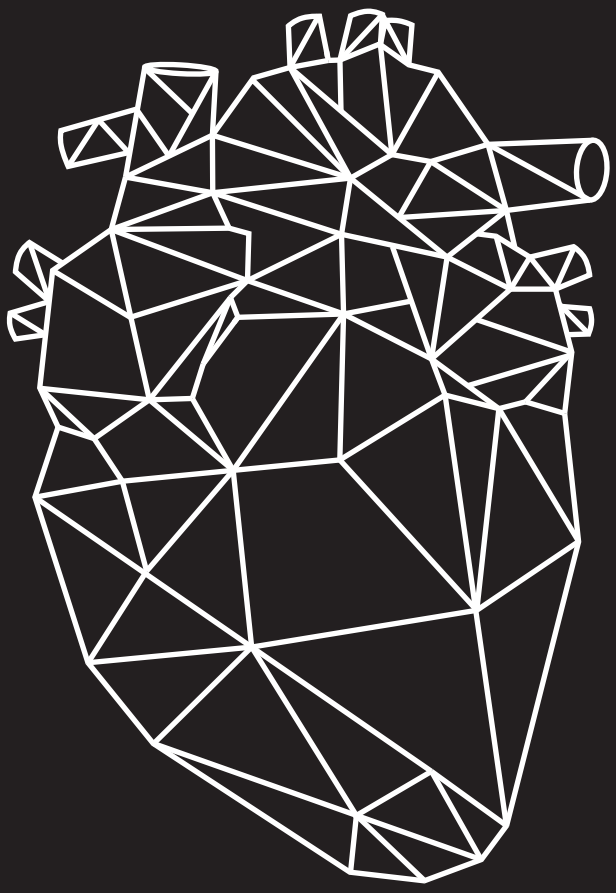

Chapter 4

Validation of a Novel Stand-Alone Software Tool for Image Guided Cardiac Catheter Therapy

International Journal of Cardiovascular Imaging, 2019. doi:10.1007/s10554-019-01541-9

R. van Es PhD [1], HT. van den Broek MSc [1], M. van der Naald MD 1, L. de Jong MSc [1], E.R. Nieuwenhuis MSc [1], A.O. Kraaijeveld MD PhD [1], P.A. Doevendans MD PhD [1,2], S.A.J. Chamuleau MD PhD [1], F.J. van Slochteren PhD [1]

[1] Department of Cardiology, University Medical Center Utrecht, Utrecht, The Netherlands
[2] Netherlands Hearts Institute / Central Military Hospital Utrecht, Utrecht, The Netherlands

Abstract

Comparison of the targeting accuracy of a new software method for MRI-fluoroscopy guided endomyocardial interventions with a clinically available 3D endocardial electromechanical mapping system. The new CARTBox2 software enables therapy target selection based on infarction transmurality and local myocardial wall thickness deduced from preoperative MRI scans. The selected targets are stored in standard DICOM datasets. Fusion of these datasets with live fluoroscopy enables real-time visualization of MRI defined targets during fluoroscopy guided interventions without the need for external hardware. In ten pigs (60-75 kg), late gadolinium enhanced (LGE) MRI scans were performed 4 weeks after a 90-min LAD occlusion. Subsequently, 10-16 targeted fluorescent biomaterial injections were delivered in the infarct border zone (IBZ) using either the NOGA 3D-mapping system or CARTBox2. The primary endpoint was the distance of the injections to the IBZ on histology. Secondary endpoints were total procedure time, fluoroscopy time and dose, and the number of ventricular arrhythmias. The average distance of the injections to the IBZ was similar for CARTBox2 (0.5 ± 3.2 mm) and NOGA (-0.7 ± 2.2 mm; $p = 0.52$). Injection procedures with CARTBox2 and NOGA required 69 ± 12 and 60 ± 17 min, respectively ($p = 0.36$). The required endocardial mapping procedure with NOGA prior to injections, leads to a significantly longer total procedure time ($p < 0.001$) with NOGA. Fluoroscopy time with NOGA (18.7 ± 11.0 min) was significantly lower than with CARTBox2 (43.4 ± 6.5 min; $p = 0.0003$). Procedures with CARTBox2 show a trend towards less ventricular arrhythmias compared to NOGA. CARTBox2 is an accurate and fast software-only system to facilitate cardiac catheter therapy based on gold standard MRI imaging and live fluoroscopy.

Introduction

Multimodality image integration during fluoroscopy guided cardiac interventions enables conjunct visualization of soft tissue characteristics during the intervention. X-ray fluoroscopy (XRF) is traditionally used to guide the catheter during minimally invasive procedures. Since XRF is unable to accurately display soft tissues, fusing XRF with MRI images enables superimposition of the cardiac anatomy on fluoroscopic images.[1,2] Since the contrast of native clinical MRI scans can be low, the benefit of solely anatomy visualization is limited and does not allow the user to determine exact targets. A real benefit arises when the MRI dataset is pre-processed before the fusion to emphasize and visualize only its relevant anatomical of functional aspects during the procedure.

To optimize procedural success accurate identification of the target location for e.g. ablation of an arrhythmic focus, the positioning of a pacing lead or performing an endomyocardial biopsy or injection, it is important that identification is done based on the associated gold standard imaging modality. In close collaboration with CART-Tech B.V. (Utrecht, the Netherlands), we have therefore developed CARTBox2 software, which facilitates offline MRI based treatment planning for cardiac catheter interventions. CARTBox2 is MRI-vendor, XRF-vendor and catheter-vendor independent and enables the user to process an MRI dataset to annotate and visualize parameters of interest such as myocardial infarction transmurality or myocardial wall thickness. The software subsequently stores all information in a DICOM treatment dataset which contains the annotated information as well as anatomical data to facilitate its registration with XRF. The annotated regions can then be visualized in conjunction with the interventional fluoroscopy imaging system in real-time during the intervention.

The aim of the present study was to assess the accuracy of CARTBox2 for the targeted delivery of cardiac catheter therapy to the border zone of myocardial infarction based on the gold standard for myocardial infarction assessment: Late Gadolinium Enhancement (LGE)-MRI. For comparison, the clinical standard NOGA® XP platform (Biosense Webster Cordis, Johnson & Johnson, USA) for intramyocardial injections in the infarct border zone (IBZ) based on electro-mechanical maps was used.[3] In a porcine model of myocardial infarction, we compared the IBZ targeting accuracy of the CARTBox2 and the NOGA system.

Secondary endpoints were the total XRF time and dose, procedure time and arrhythmogenicity of the procedure.

Methods

Animals

All experiments were performed in accordance with the "Guide for the Care and Use of Laboratory Animals", prepared by the Institute of Laboratory Animal Resources, and with prior approval by the Animal Experimentation Committee of the Faculty of Medicine, Utrecht University, the Netherlands. For this study, 14 6-months old 60–75 kg female Dutch Topigs pigs (Van Beek SPF varkensfokkerij B.V., Lelystad, The Netherlands) were subjected to an anteroseptal myocardial infarction by a 90-min occlusion of the left anterior descending artery distal to the second diagonal branch, according to a previously described protocol.[4] Pre-treatment and anesthesia during the ischemia/reperfusion (I/R) procedure were performed as described before.[5] Before starting all procedures, 300 mg amiodarone and heparin (100 IE/kg after positioning the sheaths and 50 IE/kg every 2 h) were administered. Pigs were mechanically ventilated with a positive pressure ventilator with FiO2 = 0.5, 10 ml/kg tidal volume and a frequency of 12/min under continuous capnography. An additional arterial line was inserted for continuous arterial blood pressure monitoring. After I/R, the animals were housed in stables for 4 weeks.

Before the injection procedure, 4 weeks after I/R, all animals underwent an LGE-MRI scan to visualize the myocardium, the myocardial wall thickness, the myocardial infarction and IBZ (MRI parameters are listed in the Supplementary Data). For the injections, a mixture of 10% ureido-pyrimidinone gel, superparamagnetic iron oxide (SPIO) particles (15 μg/ml; Sinerem, Guerbet, France) and fluorescent beads (10.000 beads/ml, 580/em605, Molecular Probes Invitrogen) was used.[6–8] The animals were randomized to undergo intramyocardial injections using either the NOGA system or CARTBox2 (**Figure 1**). In each animal at least 10 injections (0.2 ml) were performed using the Myostar® injection catheter (Biosense Webster), needle extension was set to half of the myocardial wall thickness in the IBZ measured on MRI. After the injection procedures, gadolinium was administered

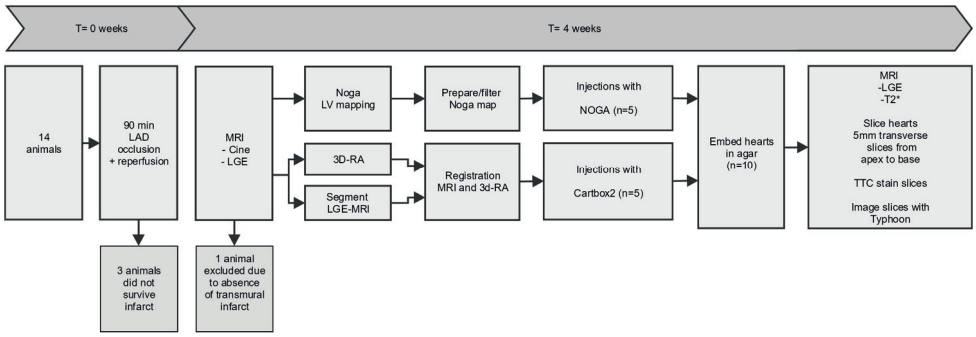

Figure 1: Experimental study design. A total of 14 animals were subjected to myocardial infarction, ten animals underwent the injection procedure. Five animals were randomized into the NOGA-arm, whilst 5 animals were randomized to the CARTBox2 group. All ten hearts were embedded and analysed.

intravenously (GadoVist 0.2 ml/kg) and 15 min later the animals were euthanized using an intravenous bolus of 20 ml 7.5% potassium chloride.

Injection procedure

The NOGA group

The NOGA system was used to create an electromechanical map of the left ventricle (LV) using the NOGAStar® mapping catheter that provides 3D magnetic tracking.[9] To create the 3D Map the catheter is steered over the LV endocardial wall to measure local unipolar and bipolar depolarization voltages and wall deformation (linear local shortening). By acquiring the end-diastolic positions of the catheter during the measurements (mapping points) on the LV endocardium a 3D point cloud is created.[10] Subsequently, the measured parameters are interpolated between the points to reconstruct a 3D endocardial surface on which the location of the infarct, the IBZ, and consequently the target area for the injections can be identified based on the measured parameters. After the mapping procedure, a trackable injection catheter is inserted into the LV to perform injections into the IBZ based on the created 3D map.

Preparation

An 8F sheath was placed in the right femoral artery. Under XRF guidance, the NOGAStar® mapping catheter (Biosense Webster) was introduced into the LV via retrograde passage through the aortic valve. Using the NOGA system (SW version 1.1.43), measurements were performed homogeneously over the endocardial wall to ensure complete al coverage of the LV endocardium. After the mapping procedure, the NOGA maps were filtered using the moderate filter option of the NOGA system. If necessary more points were acquired to maintain the homogeneous distribution of the points over the endocardium. The map was finalized when at least 100 points met the aforementioned criteria. Subsequently, the infarct was identified by setting bipolar voltages maps to a range of 0.5–1.5 mV and a target line (preferred injection location) was manually drawn on the 1 mV area around the infarct using the NOGA system software.

Injection procedure

The Myostar® injection catheter was introduced into the LV and injections were performed at the target line. In both study groups, a provoked extra-systole on the ECG signal upon needle exertion was defined as successful needle insertion in the myocardium.

CARTBox2 group

Preparation

First, endo- and epicardial contours were manually segmented in the end-diastolic LGE-MRI images using the freely available software Segment version 2.0 R4265 (http://segment.heiberg.se).[11] Subsequently, the infarct was segmented with Segment based on the full width at half maximum algorithm (**Figure 2**).[12,13] Next the segmentations were loaded into the CARTBox2 software to assign 16 injection targets into the IBZ region with 1–20% infarct transmurality and wall thickness (WT) of > 5 mm, equally distributed over the septal and anterior side of the infarct. Areas with transmurality higher than 20% or WT < 5 mm were marked as danger zones. Thereafter, the targets were stored in a separate DICOM treatment dataset for each target. The infarct transmurality (e.g. with 20% infarct transmurality, 20% of the myocardial in the radial direction consists of infarcted myocardium) was determined using the full width at half maximum segmented LGE-MRI images.[12,13]

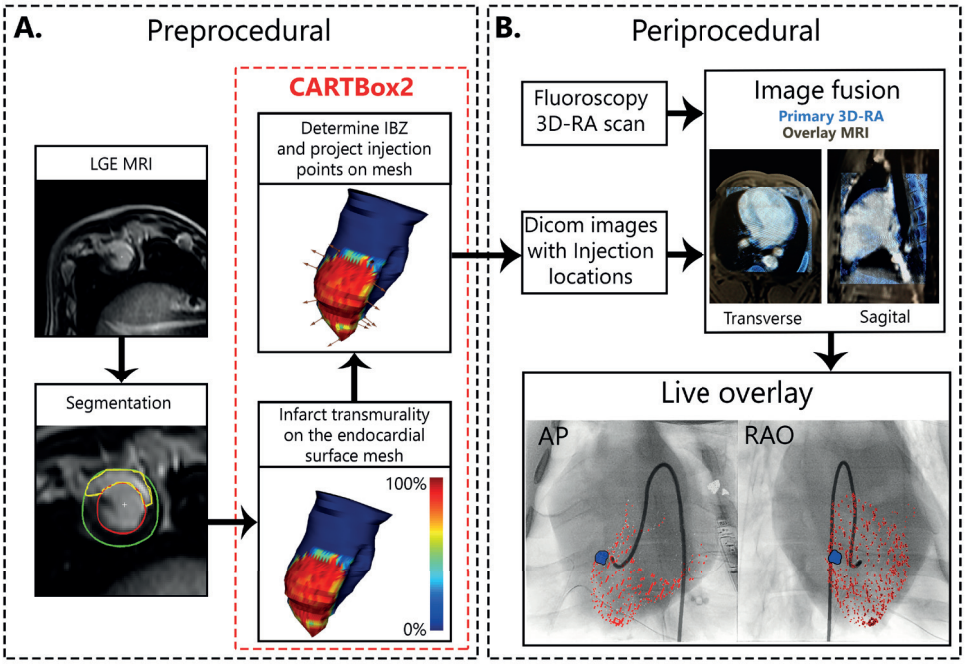

Figure 2: CARTBox2 workflow. A The preprocedural steps include the acquisition of an LGE-MRI scan of the left ventricle. The endocardium, epicardium, and infarct are then segmented. Using CARTBox2, from these segmentations, the scar transmurality is calculated and projected onto the endocardial surface mesh. Subsequently, the IBZ is calculated and the injection locations are defined and projected onto the mesh (brown arrows), these locations are embedded into the MRI DICOM images. **B** After acquiring a 3D-RA scan, the MR DICOM image is fused with the 3D-RA image based on skeletal anatomy. During the injection procedure, the target locations are visualized on the live fluoroscopic images. The AP and RAO images showing the endocardium (red) and target (blue) are visually enhanced for printing purposes. LGE-MRI: late gadolinium enhanced magnetic resonance image, IBZ: infarct border zone, 3D-RA: 3-dimensional rotational angiography, AP: anterior-posterior, RAO: right anterior oblique.

Injection workup

A 3D rotational angiography (3D-RA) roll scan of the thorax was performed using a single plane C-arm (Allura FD 20, Philips Healthcare, the Netherlands; parameters in **Supplementary Data**). A 3D reconstruction is made from a 180 degrees rotation of the C-arm during 10.2 s. With an average heart rate of 60 bmp during the rotational scan on average 10 heartbeats are contained in the 3D reconstruction leading to a 3D

representation of the end diastolic outer contour of the heart. The DICOM treatment datasets containing the injection targets are also acquired at end diastole and were semi-automatically fused with the resulting 3D-RA dataset, first based on thoracic anatomy to align the two volumes and secondly based on the epicardial contour using Interventional Tools (R8.8.1) on the Philips workstation. Meanwhile, an 8F sheath was placed in the right femoral artery.

Injection procedure

The Myostar® injection catheter was introduced into the LV via femoral access and retrograde passage through the aortic valve under XRF guidance. The injection targets were displayed in combination with XRF. After registration, the targets are locked to the XRF hardware and move in conjunction with the XRF detector/C-arm movement. Injections were aimed at the targets displayed on XRF. Targeting of a displayed point was verified by inspecting the catheter location from at least 2 fluoroscopic angles that were at least 30 degrees apart.

Histological processing

After euthanasia, the heart was excised and prepared in an agarose solution for coarse histological analysis as previously described.[14]

After complete gelation of the agarose, ex vivo LGE and T2* MRI scans were performed to image the SPIOs (parameters in **Supplementary Data**). Thereafter, the embedded heart was cut into 5 mm thick transversal slices starting at the apex with a Berkel® meat slicer. The cuts were angulated identical to the angulation of short-axis ex-vivo MRI acquisitions. Tissue slices were stained in a 1 m% dissolved 2,3,5-triphenyltetrazoliumchloride (TTC) solution. Both sides of every slice were photographed and scanned using a Typhoon 9410 (GE Healthcare) variable mode scanner set at 2 channels (ch.1 532 nm, filter: 580BP30; ch.2 633 nm, filter: 610BP30) with an image resolution of 0.1×0.1 mm to visualize the fluorescent beads.

Data analysis

Per-procedural ventricular arrhythmia monitoring

In 8 animals ECG leads of a Holter device (Fysiologic ECG Services, Amsterdam, The Netherlands) were attached to the chest of the animals to enable continuous recording during the mapping and injection procedures. The total number of premature ventricular contractions (PVCs), non-sustained ventricular tachycardias (VT) and sustained VTs were counted during the mapping procedure and each separate injection by two investigators blinded for randomization. A PVC was defined as a single ectopic complex, a doublet was counted as 2 PVCs. Non-sustained VTs were defined as 3 or more consecutive ventricular complexes with a frequency more than 100/min with a total duration shorter than 30 s.

Injection accuracy assessment

In the fluorescent images, the myocardial scar tissue was segmented and the TTC and ex vivo LGE-MRI images were used for verification of the infarct location and morphology.[14] The positions of the injections were annotated in the fluorescence images. The primary endpoint of this study, the distance of each injection to the 1–20% infarct transmurality region was measured along the endocardial contour in the segmented fluorescence images by two observers blinded for study randomization (**Figure 4**). The depth of each injection and the wall thickness were measured perpendicular to the endocardial contour.

Statistical analysis

All normally distributed data are presented as mean ± standard deviation. A Shapiro–Wilk test was used to test the data for normality. With all repeated measurements, a mean per animal was used for comparison. Continuous variables with a normal distribution were compared with a two tailed unpaired *t* test, categorical data was compared using a Chi square test. No outlier analysis was performed. A p-value of < 0.05 was considered to be statistically significant. All analyses were performed using SPSS (IBM® SPSS® Statistics, version 23).

Table 1: Baseline characteristics

Parameter	NOGA (n = 5)	CARTBox2 (n = 5)	p-value
Body weight (kg)	72.7 ± 6.4	70.5 ± 5.1	0.559
LV mass (gr)	132 ± 14	120 ± 19	0.309
Infarct size (gr)	13.4 ± 5.0	19.0 ± 5.8	0.141
Ejection fraction (%)	52.6 ± 8.7	46.9 ± 4.4	0.236
End diastolic volume (ml)	127 ± 27	126 ± 27.5	0.950
End systolic volume (ml)	61 ± 20	67 ± 17	0.658

All parameters except body weight were measured using MRI.

Results

An anteroseptal myocardial infarction was induced successfully in 14 animals. One animal died during the infarct induction, one animal died in the night following infarct induction, most likely due to a cardiac arrhythmia. One animal was euthanized 1 week after infarct induction after reaching the 'humane' end-point due to congestive heart failure. Eleven animals survived to 4 weeks (**Figure 1**). One animal was excluded from the study after the MRI scan due to the absence of a clear infarct and IBZ. Consequently, in total 5 animals were treated and analysed in both groups. Baseline characteristics were balanced between the two study groups (**Table 1**).

Noga mapping procedure

In the 5 animals that underwent electromechanical mapping with the NOGA system, an average of 135 ± 57 measurements (points) were acquired per map. The average NOGA mapping procedure duration was 90.0 ± 9.2 min. The average XRF time and dose during mapping were 12.9 ± 9.9 min and 18.2 ± 19.0 Gy·cm^2, respectively. A total of 157 ± 62 PVCs and 78 ± 56 non-sustained VTs were observed during the mapping procedure.

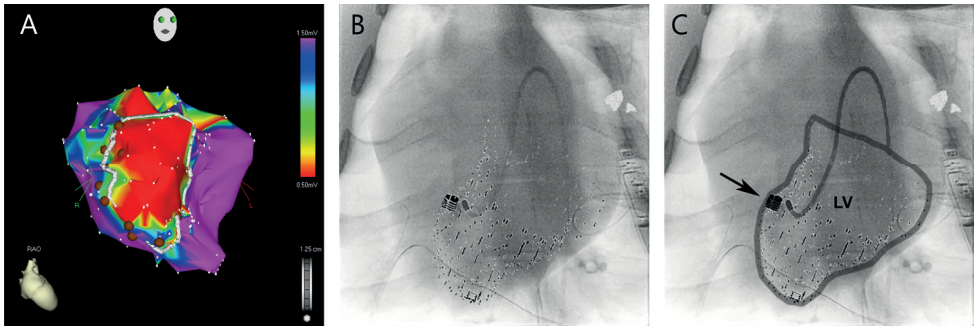

Figure 3: Examples of NOGA and CARTBox injection procedure. A Example of a NOGA bipolar voltage map (colour scale: 0.5–1.5 mV) in right anterior oblique view, with design line (white) to indicate the infarct border zone. The injections are shown as brown circles. **B** Anterior-posterior X-ray fluoroscopy image fused with the CARTBox2 modified MRI scan. The left ventricular endocardium (small dots) and the injection target (large dot). **C** The same image as shown in **B**, the endocardial wall and catheter are visually enhanced. The arrow indicates the injection target defined on late gadolinium enhanced MRI.

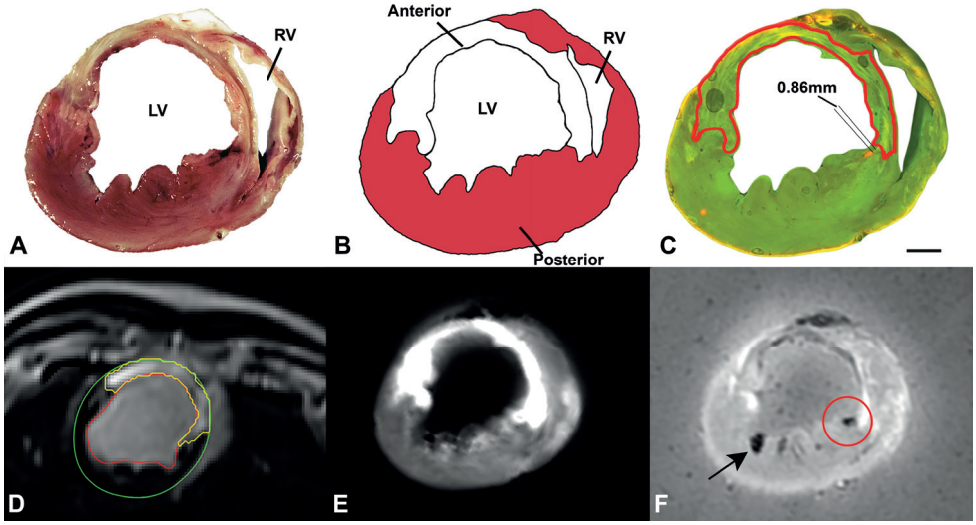

Figure 4: Example of histological analysis. A Photograph of a heart slice after TTC staining. **B** Schematic impression of the heart slice shown in **A**, with the myocardium shown in red and the infarct in white. **C** Fluorescent image of the same heart slice showing the injection deposition in orange. The infarct segmentation is shown in red. The parallel lines indicated the measured distance from the injection to the infarct area. **D** In vivo LGE-MRI scan of the heart. The segmentation was used in CARTBox2, the red line = endocardial border, green line = epicardial border and yellow line = infarct segmentation. **E** Ex vivo LGE-MRI image of the heart slice shown in figures **A-C**, which was used to segment the infarct location. **F** Ex vivo T2* image of the heart slice that was used to confirm the location of the injections found with fluorescent imaging (indicated by red circle). The arrow points towards an air-bubble.

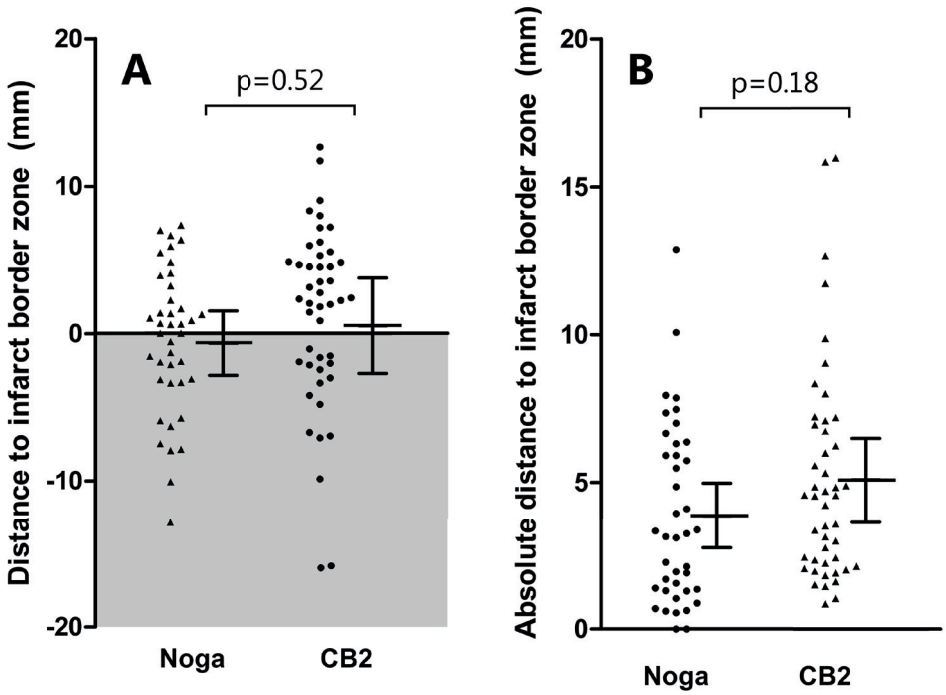

Figure 5: Details of injections. A-B The dots represent individual injections with NOGA (n = 40) and CARTBox2 (n = 46). The error bars show the mean and standard deviation of the injections in each animal. **A** The gray area indicates the infarct area.

Intramyocardial injections

A total of 118 injections were performed using the NOGA system (5 animals, 58 injections; e.g. **Figure 3A**) or the CARTBox2 system (5 animals, 60 injections; e.g. **Figure 3B-C**). During histological analysis, 8.0 ± 1.2 (71 ± 16%) and 9.2 ± 3.1 (76 ± 16%; p = 0.45) injections were retrieved in the NOGA and CARTBox2 groups, respectively (e.g. **Figure 4**). The average distance of the injections to the IBZ was not significantly different for NOGA (− 0.7 ± 2.2 mm) and CARTBox2 (0.5 ± 3.2 mm; p = 0.52) (**Figure 5**). The average injection depth was 2.9 ± 1.5 mm and 3.4 ± 1.0 mm (p = 0.59) for NOGA and CARTBox2, respectively.

Injection procedure duration

The total procedure duration of CARTBox2 (69.2 ± 11.9 mins) was significantly shorter than the total procedure duration of NOGA (150.2 ± 12.4 mins) ($p < 0.001$) (**Table 2**). The CARTBox procedure contains the 3D-RA and injection procedure whereas the NOGA procedure contains both a mapping and an injection procedure (**Table 2**). No significant difference was found in the duration of the injection parts of the two methods: 69.2 ± 11.9 mins vs. 60.2 ± 16.7 mins for CARTBox and NOGA, respectively (**Table 2**).

XRF time and dose during injections

In the CARTBox2 group, the average 3D-RA roll scan radiation dose was 5.6 ± 1.6 Gy·cm^2. Significantly more XRF time and dose were used with the CARTBox2 procedures (**Table 2**).

Ventricular arrhythmia monitoring

In both groups, Holter recordings were successfully analysed in four animals. In the NOGA and CARTBox2 groups, respectively 2 and 1 animal(s), suffered a sustained VT during the injection procedure that required cardioversion. Procedures with CARTBox2 showed a trend towards fewer PVCs and non-sustained VTs than NOGA procedures (**Table 2**).

Table 2: Injection procedure parameters

	NOGA (n = 5)	CARTBox2 (n = 5)	p
Injection procedure			
Time (min)	60.2 ± 16.7	69.2 ± 11.9	0.355
Total XRF time (min)	6.1 ± 6.2	43.4 ± 6.5	< 0.001
Total DAP (Gy·cm^2)	11.2 ± 18.0	64.2 ± 49.0	0.071
PVCs (#)[a]	239 ± 100	283 ± 10	0.42
Non-sustained VTs (#)[a]	41.5 ± 11.7	74.3 ± 35.0	0.13
Per injection			
Time (min/injection)	5.4 ± 1.8	6.0 ± 1.4	0.55
Total XRF time (min/injection)	0.5 ± 0.5	3.7 ± 0.8	< 0.001
Total DAP (Gy·cm^2/injection)	0.9 ± 1.4	5.4 ± 3.6	0.031
PVCs (#)[a]	21.0 ± 7.3	20.3 ± 1.1	0.86
Non-sustained VTs (#)[a]	3.7 ± 0.5	5.2 ± 2.1	0.21
Total procedure (Mapping/3D-RA + injections)			
Total time (min)	150.2 ± 12.4	69.2 ± 11.9	< 0.001
Total XRF time (min)	18.7 ± 11.0	43.4 ± 6.5	0.003
Total DAP (Gy·cm^2)	29.4 ± 35.7	69.8 ± 49.0	0.174
PVCs (#)[a]	396 ± 138	283 ± 10	0.20
Non-sustained VTs (#)[a]	120 ± 68	74.3 ± 35.0	0.28

[a] Holter recording and analysis were performed only in the last 8 animals (4 in each group). DAP: dose area product, XRF: X-ray fluoroscopy, PVC: premature ventricular contraction, VT: ventricular tachycardia.

Discussion

In this study, we have assessed the accuracy of CARTBox2 to target injections to the IBZ in a large animal model of myocardial infarction. For comparison, we have used a clinically available electromechanical mapping and catheter tracking system dedicated to perform intramyocardial injections into the IBZ. To the best of our knowledge, this is the first study in which an MRI-vendor, XRF-vendor and catheter-vendor independent software-only image fusion technique was used for the real-time visualization of injection targets during intramyocardial injections performed with XRF. We showed that CARTBox2 is able to accurately guide intramyocardial injections to the targets located on the IBZ. Since CARTBox2 does not require an endocardial mapping procedure, CARTBox2 procedures were significantly shorter than procedures performed with NOGA. Because navigation with CARTBox2 is done solely based on XRF, the total XRF time and dose were significantly higher

with CARTBox2 procedures than with NOGA, but are comparable with a typical percutaneous coronary intervention (PCI). The number of induced cardiac arrhythmias showed a trend towards being lower in the CARTBox2 group.

Pig model

The myocardial infarction induced by 90 min LAD occlusion lead to severe myocardial infarctions with a clear IBZ, which facilitates clear measurement of the primary endpoint (**Figure 4**). All unexpected deaths occurred before interventions were performed and can therefore only be attributed to the severity of the myocardial infarctions. The exclusion of one pig due to small non-transmural infarction can probably be attributed to non-total occlusion of the LAD after a resuscitation session during the infarct induction procedure.

Accuracy

With CARTBox2 we were able to define the injection target zone based on the gold standard imaging modality for myocardial infarction transmurality and wall thickness. In this study the target region in the CARTBox2 group was set at 1–20% infarct transmurality and > 5 mm wall thickness to assure histological identification of the IBZ and to avoid the transmurally infarcted and thin myocardium. In both study groups, the injections were performed using the 8F MyoStar® injection catheter. In both groups, the histological retrieval rate of the injections in both groups was not 100%, (range 54–93%). This can be explained by (1) non-successful injections, e.g. an extra-systole was provoked upon needle excursion, but the biomaterial was not delivered into the tissue, and (2) the penetration depth of the fluorescent light was limited to 1.5 mm while the histological slices were cut at 5 mm to allow tissue handling. On average, injections performed with NOGA were located on the inside of the IBZ (-0.7 ± 2.2 mm), while injections with CARTBox2 were located on the outside of the IBZ (0.5 ± 3.2 mm; $p = 0.52$). This difference is most likely caused by the slightly different region that is targeted by the set 1–20% infarct transmurality zone with CARTBox2 compared to the 0.5–1.5 mV setting with NOGA. Despite some studies showed considerable variability in bipolar voltage (BV) values for regions of specific infarct transmurality it was also shown that BV was specifically sensitive for transmural infarcts.[10,15] BV is therefore considered the best parameter to assess infarct tissue since it is less sensitive for far-field signals.[15,16] The thresholds used in this study were selected based on an

extensive literature study and historical data. Since the injections in both study groups are placed close to the real IBZ we believe that the error induced hereby was minimal. To further limit this intrinsic error of the NOGA procedure we performed extensive mapping and applied filtering so that at least 100 points homogeneously distributed over the LV endocardium remained in each dataset to minimize the error introduced by interpolation of endocardial potentials and point locations.

With CARTBox2 procedures, a registration error between the LGE-MRI and 3D-RA scan can lead to a targeting error for all injections in a procedure. Theoretically, the total registration error consists of a combination of errors introduced in the multiple steps involved in the protocol, LGE-MRI segmentation, 3D-RA reconstruction and in the registration of the LGE-MRI scan with the 3D-RA. The accuracy of the segmentation of the MRI and reconstruction of the 3D-RA is limited by the resolution of the acquired data. The accuracy of the registration of both image modalities was not evaluated in this study, however by using a step-wise registration method based on skeletal and cardiac anatomy the chance of registration errors is minimized. As a proof thereof we did not observe structural differences of the location between the anterior and septal injections in the CARTBox2 groups, suggesting that a structural shift during registration was not present.

In this study, XRF during the CARTBox2 injection procedure was displayed at 3.75 frames/s, while the overlay consisted of a static end-diastolic endocardial posture of the heart. While navigating to the targets, the operator had to interpret the end-diastolic endocardial catheter position in each cardiac cycle. Using the two XRF-angle approach, the operator was, however, able to accurately assess whether the catheter reached a target position. A large difference in the location of the endocardium between the LGE-MRI and 3D-RA, e.g. due to a difference in the hemodynamic filling state of the subject, should be avoided to ensure accurate navigation.

With CARTBox2, the fusion of LGE-MRI images with XRF is performed on the XRF workstation provided by the XRF vendor and therefore is state of the art, and does not require external hardware during the injection procedure. Other studies have used online image fusion systems to guide intramyocardial injections that run on an external computer

connected to the XRF system to fuse it with LGE-MRI,[2] CT or 18F-FDG-PET/CT images.[1] Comparing the reported accuracy for LGE-MRI based XRF interventions of these respective studies 0.9 ± 5.0 mm (mean ± SD) and 4.8 ± 0.5 mm (mean ± SEM) and with our data 0.5 ± 3.2 mm (mean ± SD), suggests that the IBZ injection accuracy of CARTBox2 is in the same order of magnitude.

Procedure duration

Intramyocardial injections performed with the NOGA system require the creation of a detailed endocardial surface map. Average mapping time in this study was 90 min whereas a typical clinical NOGA mapping procedure takes about 45 min.[10] The double time taken for the mapping procedure in this study can be attributed to the chosen primary study endpoint, which required detailed mapping and filtering of the electroanatomical map to optimally assess the IBZ. The total procedure time, including the mapping and injection procedure, was significantly shorter with CARTBox2 than with NOGA. Substituting the mapping time in our study with the typical value of 45 min still leads to a significantly shorter total procedure time for CARTBox2 (69.2 ± 11.9 min) compared to NOGA (103.2 ± 13.6 min; $p = 0.004$).

In contrast to NOGA, CARTBox2 requires the acquisition (1 h) and segmentation (15 min) of an LGE-MRI scan. Since both are performed prior to the injection procedure, the Cath Lab procedure time is not increased by CARTBox2. The 3D-RA roll scan required for CARTBox2 is acquired prior to the injection procedure and takes less than 1 min but does add to the total amount of radiation of the CARTBox2 procedure. Subsequently, registration of the LGE-MRI with 3D-RA was performed during the time in which the arterial access sheaths were placed and consequently did not increase the procedure time. In this study, we found no significant difference in the time required for the intramyocardial injections of both systems. Of note, the targeting facilitated by CARTBox2 is of a different nature compared to NOGA. With CARTBox2 the physician is aiming for a single target at a time, without visualization of the IBZ or neighbouring targets (**Figure 3B and 3C**), whereas with NOGA the physician can navigate over the IBZ, whilst other injections are visualized (**Figure 3A**). The abovementioned fundamental difference between both systems is likely to have caused an increase in the procedure time of the CARTBox2 procedures.

XRF time and dose

Injections performed with CARTBox2 required significantly more XRF time in comparison with the NOGA system. The DAP per minute of XRF per injection is lower in the CARTBox2 group, showing that the XRF angulation and rotation used with CARTBox2 (mainly right/left anterior oblique) required less XRF energy compared to the angulation used with NOGA (mainly anterior-posterior). With the NOGA system being a non-fluoroscopic navigation system, XRF guidance is only required for passing the aortic valve and during the initial mapping points. We were unable to find any reports in the literature on XRF usage during NOGA procedures. The average reported doses for a PCI are in the range of 70–150 Gy·cm^2.[17,18] Data of the present study showed that the XRF dose with CARTBox2 procedures is similar or lower than an average PCI.

Ventricular arrhythmia monitoring

In the present study 2/5 and 1/5 animals required cardioversion during the NOGA and CARTBox2 procedures, respectively. The number of non-sustained ventricular arrhythmias per injection was similar in both study groups, suggesting that the longer procedure time (mapping) of NOGA may be responsible for the higher total number of ventricular arrhythmias. However, due to the large variation in PVCs in the NOGA group and with non-sustained VTs in both groups, no significant differences were observed between both groups.

Limitations

In this study, a single plane XRF device was used. The use of a biplane XRF device obviates the need for multiple C-arm rotations to verify optimal catheter positioning, saving much procedure time. It is therefore likely that the total procedure time with CARTBox2 would have been considerably shorter if a biplane XRF setup had been used.

The CARTBox2 approach of visualizing the target as a single point instead of a targeting line forced the operator to manoeuvre the catheter to that exact position. This approach inevitably increased injection duration during the CARTBox2 procedure when a target was difficult to reach. Instead of changing focus to a reachable target, time was spent on reaching difficult targets. The visualization of a single target at a time by CARTBox2 was

chosen to optimize the 3D orientation of the physician and ease of navigation by XRF using a single plane fluoroscopy system. Showing multiple targets or the complete IBZ in combination with increased user experience will further reduce the time required for the CARTBox2 procedure.

Since the NOGA map is constructed from points that are acquired on the LV endocardium using a catheter, the target region is always reachable with the catheter. In contrast, targets selected with CARTBox2 are selected manually from LGE-MRI and can be difficult to reach with the catheter due to for example the presence of papillary muscles or the basal location of the injection target. More experience with the pre-procedural selection of injection targets can prevent selection of targets that are difficult to reach.

Clinical implications

In the present study, we have compared CARTBox2 to a clinically available electromechanical mapping system for intramyocardial injections into the IBZ. CARTBox2 is however not limited to this type of procedure and it can be used for all procedures for which pre-operative treatment planning based on 3D imaging data is beneficial. Other possible applications are the lead placement for cardiac resynchronization therapy devices, acquiring endomyocardial biopsies or performing ablations in regions with a scar substrate. The fusion of processed LGE-MRI data, or wall thickness analysis from multi-detector CT scans with the electro-anatomical navigation systems to guide ventricular tachycardia substrate mapping and ablation have been described.[19,20]

With CARTBox2, not only targets can be identified, but also areas that should be avoided can be annotated. In the case of intramyocardial injections or endocardial biopsies such areas may include sections in which the myocardium is too thin, in case of lead placement, such areas may include stretches of nonconductive fibrous myocardium or locations in proximity to the phrenic nerve.

For the purpose of intramyocardial injections, the use of CARTBox2 as an alternative to the NOGA system for intramyocardial injections may significantly shorten the procedure time and increase Cath Lab capacity. Furthermore, CARTBox2 obviates the need for expensive dedicated intramyocardial injection systems in terms of acquisition, training and operating

(e.g. mapping and injection catheters) costs. The radiation dose with CARTBox2 injection procedures is higher than during the NOGA procedures, but does not exceed that of a typical PCI, and is likely to decrease with experience.

Conclusion

CARTBox2 is a safe and accurate alternative 'software-only' technology for treatment planning and fluoroscopy based image-guided cardiac catheter therapies. The data of this study on the specific topic of intramyocardial injections shows that the procedures performed with CARTBox2 are equally accurate and quicker. In contrast, CARTBox2 requires the acquisition of an LGE-MRI scan and requires more fluoroscopy than NOGA. The software only CARTBox2 method enables its use in all cardiologic centres that have modern fluoroscopic imaging equipment.

Notes

Acknowledgements

We kindly acknowledge Marlijn Jansen, Joyce Visser and Martijn van Nieuwburg for their assistance with the animal procedures. Martijn Froeling and Anke Wassink are greatly acknowledged for their assistance with the acquisition of the MRI scans. Patricia Dankers is acknowledged for her help with the Upy gel. We greatly acknowledge Dave Hopman of Fysiologic B.V. for his dedication in assisting with the Holter analyses and CART-Tech B.V. for providing software and support during the study.

Conflict of interest

Authors SC and FvS are co-founders of CART-Tech B.V., the other authors have no conflicts of interest to declare. Authors RvE, SC and FvS have filed patents on the topic of cardiac navigation technology.

References

1. Dauwe DF, Nuyens D, Buck S De, Claus P, et al. Three-dimensional rotational angiography fused with multimodal imaging modalities for targeted endomyocardial injections in the ischaemic heart. *Eur Heart J Cardiovasc Imaging* 2014;**15**(8):900–907. doi:10.1093/ehjci/jeu019.

2. Tomkowiak MT, Klein AJ, Vigen KK, Hacker T a, et al. Targeted transendocardial therapeutic delivery guided by MRI-x-ray image fusion. *Catheter Cardiovasc Interv* 2011;**78**(3):468–478. doi:10.1002/ccd.22901.

3. Psaltis PJ, Worthley SG. Endoventricular electromechanical mapping-the diagnostic and therapeutic utility of the NOGA XP Cardiac Navigation System. *J Cardiovasc Transl Res* 2009;**2**(1):48–62. doi:10.1007/s12265-008-9080-7.

4. Koudstaal S, Jansen of Lorkeers SJ, Gho JMIH, Hout GPJ van, et al. Myocardial infarction and functional outcome assessment in pigs. *J Vis Exp* 2014;(86):1–10. doi:10.3791/51269.

5. Jansen of Lorkeers SJ, Gho JMIH, Koudstaal S, Hout GPJ van, et al. Xenotransplantation of Human Cardiomyocyte Progenitor Cells Does Not Improve Cardiac Function in a Porcine Model of Chronic Ischemic Heart Failure. Results from a Randomized, Blinded, Placebo Controlled Trial. Tang Y, ed. *PLoS One* 2015;**10**(12):e0143953. doi:10.1371/journal.pone.0143953.

6. Bastings MMC, Koudstaal S, Kieltyka RE, Nakano Y, et al. A fast pH-switchable and self-healing supramolecular hydrogel carrier for guided, local catheter injection in the infarcted myocardium. *Adv Healthc Mater* 2014;**3**(1):70–78. doi:10.1002/adhm.201300076.

7. Pape a. CH, Bakker MH, Tseng CCS, Bastings MMC, et al. An Injectable and Drug-loaded Supramolecular Hydrogel for Local Catheter Injection into the Pig Heart. *J Vis Exp* 2015;(100):e52450. doi:10.3791/52450.

8. Delikatny EJ, Poptani H. MR techniques for in vivo molecular and cellular imaging. *Radiol Clin North Am* 2005;**43**(1):205–220. doi:10.1016/j.rcl.2004.07.004.

9. Ben-Haim SA, Osadchy D, Schuster I, Gepstein L, et al. Nonfluoroscopic, in vivo navigation and mapping technology. *Nat Med* 1996;**2**(12):1393–1395. doi:10.1038/nm1296-1393.

10. Gyöngyösi M, Dib N. Diagnostic and prognostic value of 3D NOGA mapping in ischemic heart disease. *Nat Rev Cardiol* 2011;**8**(7):393–404. doi:10.1038/nrcardio.2011.64.

11. Heiberg E, Sjögren J, Ugander M, Carlsson M, et al. Design and validation of Segment - freely available software for cardiovascular image analysis. *BMC Med Imaging* 2010;**10**:1–13. doi:10.1186/1471-2342-10-1.

12. Flett AS, Hasleton J, Cook C, Hausenloy D, et al. Evaluation of Techniques for the Quantification of Myocardial Scar of Differing Etiology Using Cardiac Magnetic Resonance. *JACC Cardiovasc Imaging* 2011;**4**(2):150–156. doi:10.1016/j.jcmg.2010.11.015.

13. Gho JMIH, Es R van, Slochteren FJ van, Jansen of Lorkeers SJ, et al. A systematic comparison of cardiovascular magnetic resonance and high resolution histological fibrosis quantification in a chronic porcine infarct model. *Int J Cardiovasc Imaging* 2017;**33**(11):1797–1807. doi:10.1007/s10554-017-1187-y.

14. Broek HT Van den, Jong L De, Doevendans PA, Chamuleau SAJ, et al. 3D whole-heart myocardial tissue analysis. *J Vis Exp* 2017;**2017**(122) doi:10.3791/54974.

15. Slochteren FJ, Es R, Gyöngyösi M, Spoel TIG, et al. Three dimensional fusion of electromechanical mapping and magnetic resonance imaging for real-time navigation of intramyocardial cell injections in a porcine model of chronic myocardial infarction. *Int J Cardiovasc Imaging* 2016;1–11. doi:10.1007/s10554-016-0852-x.

16. Wijnmaalen AP, Geest RJ van der, Huls van Taxis CFB van, Siebelink H-MJ, et al. Head-to-head comparison of contrast-enhanced magnetic resonance imaging and electroanatomical voltage mapping to assess post-infarct scar characteristics in patients with ventricular tachycardias: real-time image integration and reversed registration. *Eur Heart J* 2011;**32**(1):104–114. doi:10.1093/eurheartj/ehq345.

17. Pantos I, Patatoukas G, Katritsis DG, Efstathopoulos E. Patient radiation doses in interventional cardiology procedures. *Curr Cardiol Rev* 2009;**5**(1):1–11. doi:10.2174/157340309787048059.

18. Chida K, Saito H, Kagaya Y, Kohzuki M, et al. Indicators of the maximum radiation dose to the skin during percutaneous coronary intervention in different target vessels. *Catheter Cardiovasc Interv* 2006;**68**(2):236–241. doi:10.1002/ccd.20830.

19. Andreu D, Penela D, Acosta J, Fernández-Armenta J, et al. Cardiac magnetic resonance–aided scar dechanneling: Influence on acute and long-term outcomes. *Hear Rhythm* 2017;**14**(8):1121–1128. doi:10.1016/j.hrthm.2017.05.018.

20. Komatsu Y, Cochet H, Jadidi A, Sacher F, et al. Regional myocardial wall thinning at multidetector computed tomography correlates to arrhythmogenic substrate in postinfarction ventricular tachycardia: Assessment of structural and electrical substrate. *Circ Arrhythmia Electrophysiol* 2013;**6**(2):342–350. doi:10.1161/CIRCEP.112.000191.

Supplementary Data

MRI parameters (pre-injection)

Cine

Repetition time [TR]/echo time [ET] = 3.39 ms/1.69 ms. Flip angle = 60 °, Pixel size = 1.25 x 1.25 mm, [FOV] = 320 x 320 mm, 256 x 256 matrix, 8 mm slice thickness.

Late Gadolinium Enhancement

[TR]/[ET] = 3.64 ms/1.19 ms. Flip angle = 25 °, Pixel size = 1.25 x 1.25 mm, [FOV] = 296 x 296 mm, 256 x 256 matrix, 4 mm slice thickness.

MRI parameters (ex-vivo)

LGE

[TR]/[ET] = 5.53 ms/1.69 ms. Flip angle = 25 °, Pixel size = 1.0 x 1.0 mm, [FOV] = 169 x 169 mm, 176 x 176 matrix, 3 mm slice thickness.

*T2**

[TR]/[ET] = 88.7 ms/15 equally distributed ETs with range 1.9-24.6 ms. Flip angle = 15 °, Pixel size = 0.5 x 0.5 mm, [FOV] = 169 x 169 mm, 320 x 320 matrix, 3 mm slice thickness.

XRF parameters

Cardiac low dose, 3,75fps. Exposure prefilter 0.10 mm Cu + 1.00 mm Al.

3D-RA parameters

180° rotation in 10.2s, 30fps. Max rotation speed 30°/s. Tube voltage 125kV. 128x128 reconstruction matrix

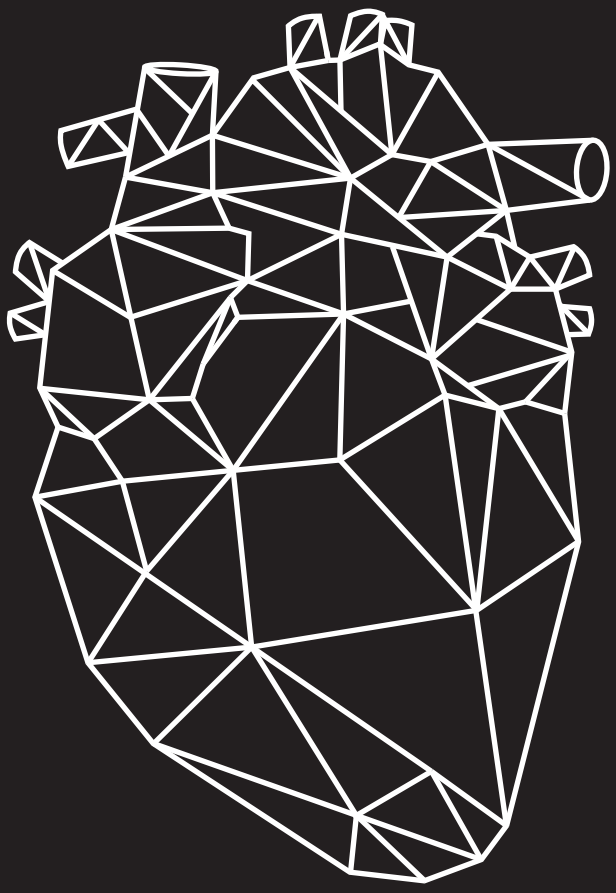

Chapter 5

Multimodality Imaging for Real-Time Image-Guided Left Ventricular Lead Placement during Cardiac Resynchronization Therapy Implantations

International Journal of Cardiovascular Imaging, 2019. doi:10.1007/s10554-019-01574-0

O.A.E. Salden MD [1], HT. van den Broek MSc [1], W.M. van Everdingen MD PhD [1], F.A.A. Mohamed Hoesein MD PhD [2], B.K. Velthuis MD PhD [2], P.A. Doevendans MD PhD [1,3], M. Cramer MD PhD [1], A.E. Tuinenburg MD PhD [1], P. Leufkens PharmD [4], F.J. van Slochteren PhD [1,4], M. Meine MD PhD [1]

The first two and last two authors contributed equally to this manuscript.

[1] Department of Cardiology, University Medical Center Utrecht, Utrecht, The Netherlands
[2] Department of Radiology, University Medical Center Utrecht, Utrecht, The Netherlands
[3] Netherlands Hearts Institute / Central Military Hospital Utrecht, Utrecht, The Netherlands
[4] CART-Tech B.V., Utrecht, The Netherlands

Abstract

This study was performed to evaluate the feasibility of intra-procedural visualization of optimal pacing sites and image-guided left ventricular (LV) lead placement in cardiac resynchronization therapy (CRT). In fifteen patients (10 males, 68 ± 11 years, 7 with ischemic cardiomyopathy and ejection fraction of 26 ± 5%), optimal pacing sites were identified pre-procedurally using cardiac imaging. Cardiac magnetic resonance (CMR) derived scar and dyssynchrony maps were created for all patients. In six patients the anatomy of the left phrenic nerve (LPN) and coronary sinus ostium was assessed via a computed tomography (CT) scan. By overlaying the CMR and CT dataset onto live fluoroscopy, aforementioned structures were visualized during LV lead implantation. In the first nine patients, the platform was tested, yet, no real-time image-guidance was implemented. In the last six patients real-time image-guided LV lead placement was successfully executed. CRT implant and fluoroscopy times were similar to previous procedures and all leads were placed close to the target area but away from scarred myocardium and the LPN. Patients that received real-time image-guided LV lead implantation were paced closer to the target area compared to patients that did not receive real-time image-guidance (8 mm [IQR: 0 – 22] versus 26 mm [IQR: 17 – 46], $p = 0.04$), and displayed marked LV reverse remodeling at six months follow up with a mean LVESV change of -30 ± 10% and a mean LVEF improvement of 15 ± 5%. Real-time image-guided LV lead implantation is feasible and may prove useful for achieving the optimal LV lead position.

Introduction

Cardiac resynchronization therapy (CRT) has had a major beneficial effect on the treatment of patients with symptomatic heart failure, severe left ventricular (LV) dysfunction, and prolonged QRS duration. Nevertheless up to 30-45% of patients do not obtain a clinical or echocardiographic benefit from CRT.[1] Improving CRT response rate has been the main focus of many researchers in the field, whom have demonstrated that improved response can be achieved by targeting optimal pacing sites for LV stimulation.[2–4]

LV lead placement in or near an area of myocardial scar worsens outcomes,[4–6] while pacing in or near an area of latest mechanical contraction improves both response rate and prognosis after CRT.[2,3] Still, the fluoroscopic projections used during CRT implantation provide no tissue characteristics, and therefore no information regarding the optimal site for LV pacing. Consequently, LV leads are mostly placed empirically on the posterolateral wall in patients undergoing CRT. However, there is a substantial inter-individual variation regarding the optimal pacing site as a result of myocardial scar regions and diversity in intrinsic electrical activation of the myocardium. Cardiac magnetic resonance (CMR) imaging has been proposed as a promising tool for LV target area identification since it is able to assess myocardial scar tissue with late gadolinium enhancement (LGE) and mechanical dyssynchrony with feature tracking.[6] Yet, LV lead delivery into target areas remains difficult due to left phrenic nerve (LPN) stimulation. And restrictions caused by coronary vein anatomy.

Aforementioned challenges call for additional techniques that offer real-time visualization of optimal pacing sites during CRT device implantation. In the present study, we test the feasibility of a custom-made treatment-guidance platform (CARTBox[7], CART-Tech B.V., Utrecht, The Netherlands) for real-time visualization of scar location, latest contracting area, and LPN position onto live fluoroscopy during CRT implantation procedures.

Methods

Study population

Fifteen patients with an indication for CRT according to the current ESC guidelines were prospectively enrolled.[8] Patients with severely impaired renal function (GFR < 30 ml/min/1.73 m^2), and patients with a contraindication for CMR, as well as patients with persistent atrial fibrillation, were excluded. All subjects gave written informed consent. The study was performed according to the Declaration of Helsinki and was approved by the local institutional review board and ethics committee.

Study design

In this prospective feasibility study, LV target areas were determined on pre-procedurally acquired CMR and computed tomography (CT) scans using a custom-made platform, CARTBox (CART-Tech B.V., Utrecht, The Netherlands). After LV target area identification, target areas were co-registered with live fluoroscopy during CRT implantations.

The study was conducted in four steps to test the feasibility of the various features of CARTBox in a stepwise approach (**Figure 1**). During steps 1-3 (including three patients per step, thus nine patients in total) specific tissue characteristics (scar, delayed mechanical activation, the LPN and coronary sinus ostium (CSO)) were identified on a pre-procedural CMR or CT scan. Based on the location of scar, delayed activation, and the LPN, a target area for LV lead delivery was chosen. Importantly, LV lead target area and tissue characteristics were fused with live fluoroscopic imaging, however they were not visible for the implanting cardiologist. Therefore, this group, in whom we performed treatment planning but no real-time image-guidance, is further mentioned as the non-target group. In step 4 (six patients) all aforementioned tissue characteristics were determined and displayed in conjunction with live fluoroscopy in the catheterization theatre during LV lead implantation. Thus enabling the implanting cardiologist to perform image-guided LV lead placement in a targeted treatment group (target group).

In all patients implantation characteristics (radiation dose, procedure and fluoroscopy time, and peri-procedural complications) were collected together with electrical properties at the

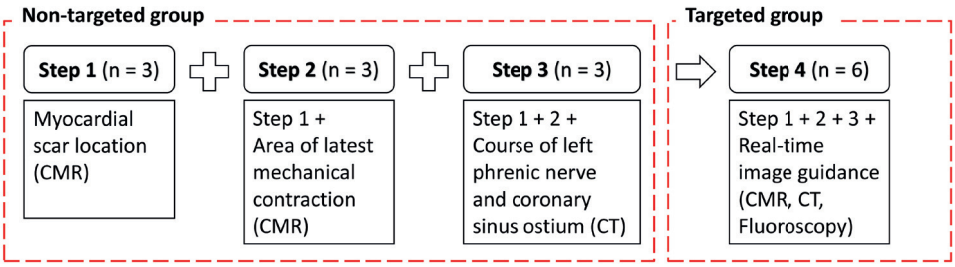

Figure 1: Schematic overview of study. Each step resembles a phase during the study. In step 1, a CMR scan was made to assess the location of myocardial scar tissue (patients 1-3). In step 2, scar identification and contraction timing analysis were performed on CMR images (patients 4-6). In step 3, a CT scan was added to identify the left phrenic nerve and coronary sinus ostium (patients 7-9). In step 1-3 the feasibility of CARTBox was tested for identification and live visualization of the structures. In step 4, steps 1-3 were combined and used for real-time image-guidance of left ventricular lead placement (patients 10-15). CMR: cardiac magnetic resonance; CRT: cardiac resynchronization therapy; CT: computed tomography.

stimulation electrode (pacing threshold, LPN stimulation threshold, paced QRS duration and the electrical delay, which was measured as the interval from Q on the surface ECG to local sensing at the LV electrogram (QLV), divided by QRS duration (QLV/QRS). Echocardiography was performed before and six months after implantation to determine the presence of LV reverse remodeling (defined as a ≥ 15% reduction in LV end-systolic volume).

Cardiac magnetic resonance imaging

CMR was performed 1-7 days prior to CRT implantation in all patients, using a 1.5 T Philips Ingenia scanner (Philips Healthcare, Best, The Netherlands). Gold standard LGE CMR scans were made to determine the size and the location of the myocardial scar. Short axis steady-state-free-precession cine images were made to determine areas of latest contraction, using feature tracking (CMR-FT) software (TomTec Arena, 2D Cardiac Performance Analysis MR, Version 1.2, Unterschleissheim, Germany). The settings during the CMR acquisitions were as follows. Cine: repetition time/echo time = 3.4 ms/1.7 ms, flip angle = 60°, voxel size = 1.67 x 1.67 mm, field of view = 32 x 32cm, 192 x 192 matrix, 8 mm slice thickness, 30 phases/R-R interval, electrocardiogram-gated. LGE: repetition time/echo time = 3.2 ms/1.6 ms, flip angle = 15°, voxel size = 2.1 x 2.1 mm, field of view = 46 x 46 cm, 220 x 220 matrix, 8 mm slice thickness. Cine and LGE scans were made at the same positions with the same orientation.

Cardiac computed tomography

CT scans were performed 2-14 days prior to CRT implantation in nine patients for the identification of LPN and CSO. CT images were acquired using Turbo Flash in a Siemens Somatom Force 384 (2 x 192) row scanner (Siemens Healthcare, Forchheim, Germany). The CT protocol was optimized for visualization of contrast in the venous system using a double bolus technique to ensure opacification of the CSO. The first bolus of 60mL of iodinated contrast medium (saline:contrast ratio: 1:2, 300 mg of iodine/mL, Ultravist; Bayer AG, Berlin, Germany) was administered at the start and the second bolus of 80 mL was injected after 40 s. Both boluses were injected at a rate of 6 mL/s into the basilic vein. CT scanning was triggered by using a bolus-tracking technique, with the region-of-interest placed in the descending aorta. Image acquisition started 11 s after the attenuation reached the predefined threshold of 200 HU. Scanning time was approximately 0.25 s. The reference tube potential and tube current were set to 100 kV and 350 mAs, respectively. Both were regulated by automatic potential and tube current programs (Care kV and Care dose 4D). Images were reconstructed with a 1.0 mm slice thickness and a 0.4 x 0.4 mm pixel spacing with a Bv40d reconstruction kernel.

Image processing

Image processing with CARTBox consisted of three steps (**Figures 2 and 3**). The first step consisted of the segmentation of a) scarred myocardium and dyssynchrony on CMR images, and b) the identification of the LPN and CSO on CT-scans.

a) To start, the LV endo- and epicardium of the end-diastolic short axis CMR cine and LGE images were automatically segmented (**Figure 3A**). The full width at half maximum method was used for the segmentation of myocardial scar on LGE images (**Figure 3B**).[9] Segmentations were manually adjusted if necessary. For detection of the latest mechanical contracting segments, time to peak analysis was performed on the short axis CMR cine images using CMR-FT software.[10,11] Time to peak endocardial circumferential strain was used for the identification of latest contracting segments (**Figure 3C**) because circumferential strain is believed to produce higher intra- and interobserver reproducibility than segmental radial strain analysis.[12,13] After image processing, scar transmurality and contraction timing data were projected on a 3D-epicardial surface mesh (**Figure 3E-F**).

b) After CMR processing, the location of the CSO and course of the LPN were segmented manually from CT data. A board-certified cardiac radiologist (FMH) reviewed the results of the segmentation processes.

In the second step, the implanting cardiologist selected the optimal area for LV lead delivery based on the course of the LPN and the 3D-CMR surface mesh containing scar transmurality [%] and contraction timing [ms] data (**Figure 3E-F**). Optimal pacing sites were chosen in an area with 0% scar transmurality and most delayed contraction. Septal segments were excluded as target areas.

In the final step, two 3D-treatment files were created by CARTBox in the standard DICOM format. One 3D-treatment file contained myocardial scar transmurality and the LV target segments (**Figure 4A**). The other 3D-treatment file consisted of the anatomy of the LPN and CSO (**Figure 4B**).

Image fusion

Prior to CRT implantation, a 3D-rotational scan was made in the catheterization theatre. In a single gantry rotation of 200°, a 3D CT-like dataset is acquired by using the Siemens Artis Zee (Syngo X workplace version B21), which allows 3D fusion of CMR and CT images with live fluoroscopy. After fusing the 3D-treatment datasets, 3D representations of the specific anatomical aspects (i.e. myocardial scar, LV lead target, LPN and/or CSO) were visualized in conjunction with the fluoroscopy images by assigning a unique color for each anatomic structure. (**Figure 4**). After registration the targets rotate accordingly upon rotation of the C-arm. The fused images were shown in a separate part of the screen in the catheterization theatre. Directly after CRT device implantation, a second 3D-rotational scan was acquired to measure the distances between the final LV pacing electrode location and the locations of the scar, LV lead target area, and LPN.

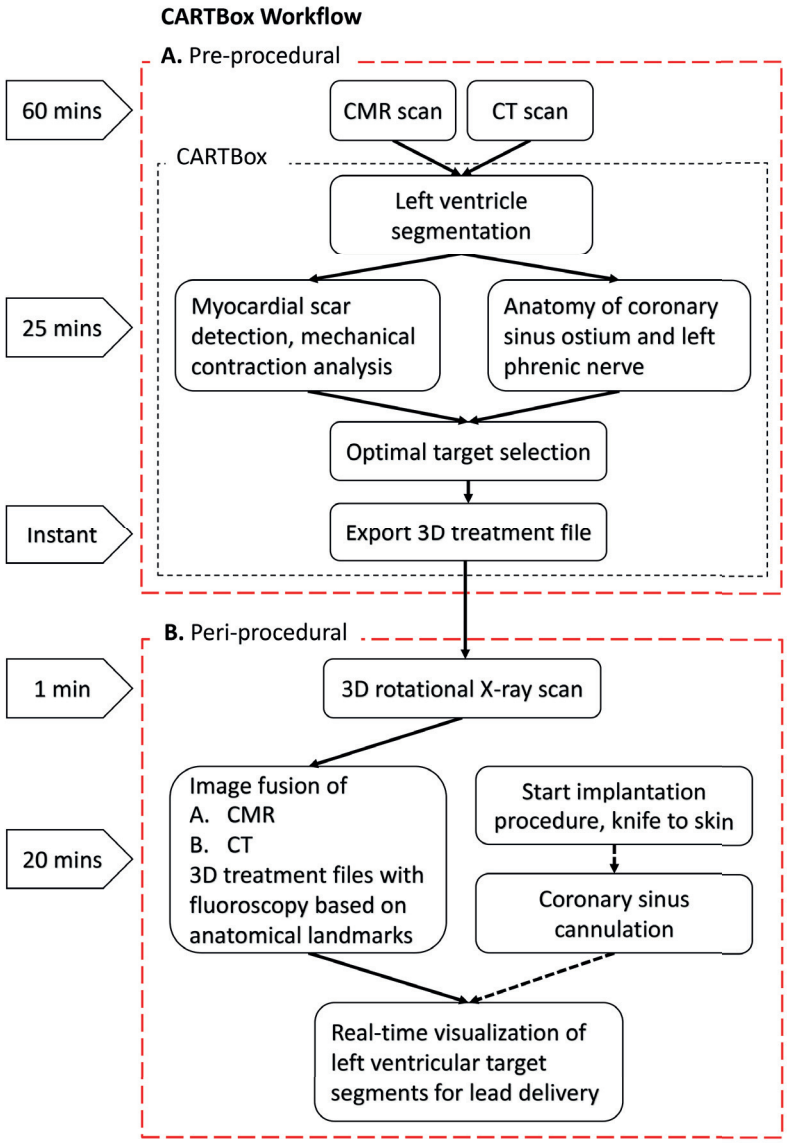

Figure 2: CARTBox workflow and time requirement. The pre-procedural workflow (**Panel A**) consists of the acquisition of cardiac MRI and CT (60 minutes in total), and image processing in CARTBox. The image processing, required to identify the optimal site for LV stimulation, and necessary to produce a detailed 3D-model of the heart, takes approximately 25 minutes per scan. The implantation procedure (**panel B**) starts with acquiring a 3D-rotational X-ray scan (minutes). The 3D-treatment files are then semi-automatically fused with the 3D-rotational scan based on anatomy landmarks. This takes approximately 20 minutes and can be performed during RV lead implantation and coronary sinus cannulation. Using this approach, LV target areas can be visualised on live fluoroscopic images during LV lead implantation. CMR: cardiac magnetic resonance; CT: computed tomography.

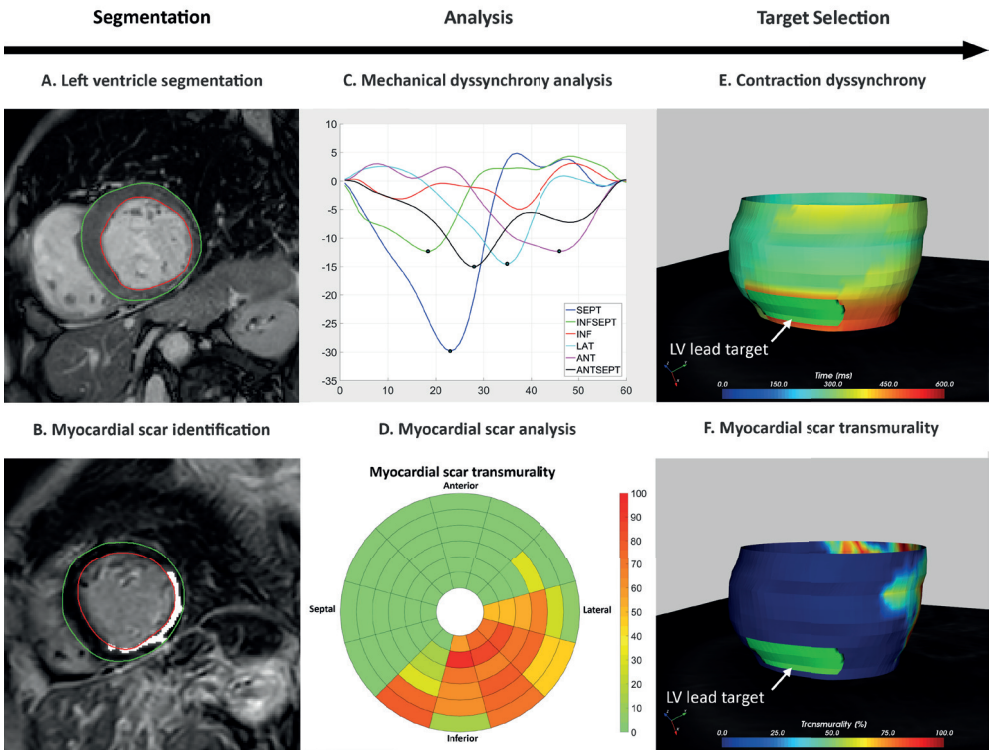

Figure 3: CARTBox workflow in images. **A** Segmentation of left ventricle. **B** Myocardial scar detected on CMR LGE scans. **C** Contraction timing analysis displaying delayed contraction of anterior and lateral segments. **D** Transmurality of scar showing inferolateral infarct of the left ventricle. **E-F** 3D-Model of contraction timing (**E**) and scar transmurality (**F**) with manual selected target segment (green). ANT: anterior; ANTSEPT: anteroseptal; INF: inferior; INFSEPT: Inferoseptal; LAT: lateral; LV: left ventricle; SEPT: septal.

CRT implantation

CRT device implantation was performed transvenously under local anesthesia based on the pre-defined target areas. The right atrial and right ventricular leads were placed at conventional locations in the right atrium appendage and the right ventricular apicoseptal segment, respectively. After CS cannulation and coronary venous angiogram, a quadripolar LV lead was placed in one of the coronary veins overlying the LV free wall. After LV lead placement, all leads were connected to a CRT device.

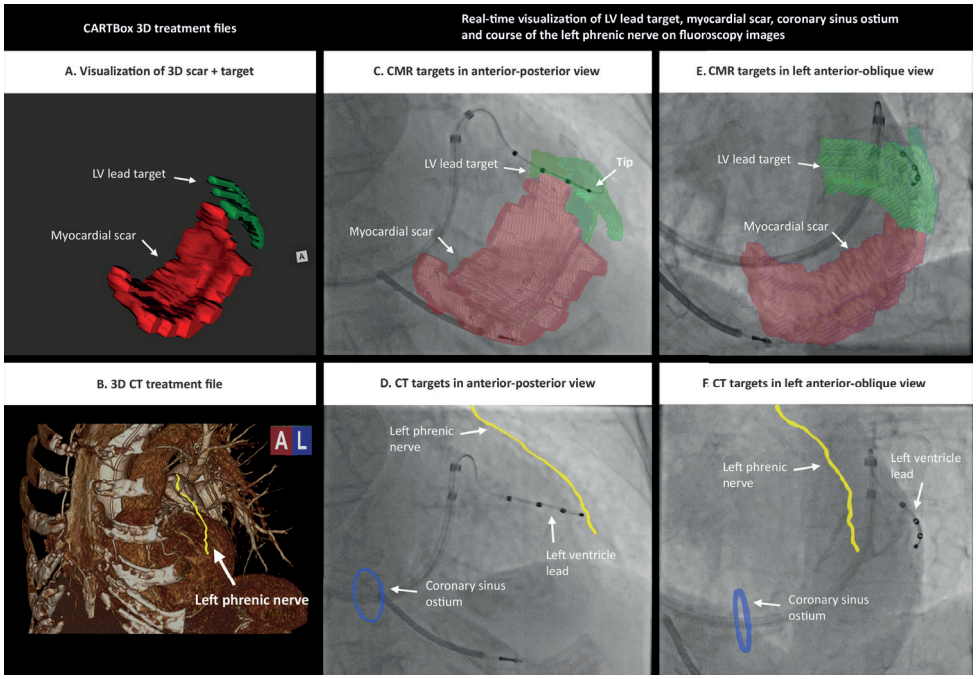

Figure 4: Real-time visualization of CMR and CT targets. A-B 3D-treatment file of CMR data (**A**) and CT data (**B**). **C-F** After 3D image fusion of the 3D-treatment dataset with fluoroscopy, the LV lead targets and scar segments (**C,E**) together with left phrenic nerve and coronary ostium (**D,F**) are visualized on live fluoroscopy during the LV lead implantation. CMR: cardiac magnetic resonance; CT: computed tomography.

Statistical analysis

Statistical analysis was performed with SPSS (SPSS statistics 23.0, IBM, New York, USA). Each variable was tested for normality with a Shapiro-Wilk test. Continuous variables with a Gaussian distribution were described using mean, standard deviation and those with non-normal distribution were described with the median, interquartile range (IQR). Categorical data were described by an absolute number of occurrences and associated frequency (%). Differences between groups were assessed using nonparametric testing with Mann-Whitney U test for continuous data with non-normal distribution, and unpaired Student t-test for continuous variables with a Gaussian distribution. Pearson Chi-Square test was used for dichotomous variables. A p-value below 0.05 was considered significant.

Table 1: Demographic data

	All patients (n=15)	Target group (n=6)	Non-target group
Male gender (%)	10 (67)	3 (50)	7 (78)
Age (years)	68 ± 11	67 ± 13	69 ± 9
Body mass index (kg/m^2)	26 ± 5	27 ± 6	26 ± 4
NYHA functional class (n, %)			
II	12 (80)	5 (83)	7 (78)
III	3 (20)	1 (17)	2 (22)
Left bundle branch block* (n, %)	11 (73)	5 (83)	6 (67)
QRS duration (ms)	162 ± 23	165 ± 26	160 ± 22
PR interval (ms)	188 ± 34	164 ± 27†	203 ± 29†
LV ejection fraction (%)	26 ± 5	27 ± 6	25 ± 5
LV end diastolic volume (ml)	209 [165-250]	175 [142-216]	222 [184-327]
LV end systolic volume (ml)	149 [123-198]	128 [96-169]	162 [135-250]
Ischemic cardiomyopathy (n, %)	7 (47)	2 (33)	6 (67)
Scar burden (%)	18 [13-28]	30 [15-45]	18 [7-28]

Values are in mean ± SD, median [interquartile range] and n (%). * Definition according to Strauss criteria. Significant differences between groups ($p < 0.05$) are indicated with a †. LV: left ventricular; NYHA: New York Heart Association.

Results

Fifteen patients, of whom baseline characteristics are provided in **Table 1**, underwent de novo CRT implantation with a quadripolar LV lead. Patients were aged 68 ± 11 years, ten were male, eleven had a left bundle branch block, and seven had ischemic cardiomyopathy (ICM) with a mean scar burden of 21 ± 13% (**Table 1**). Median size of the pre-procedurally defined LV target area was 10% [6–11] of total LV surface. In all patients, CARTBox was successfully applied and merging of the treatment file with live fluoroscopy images did not lengthen the procedure. Merging was performed during pocket preparation and right ventricular lead implantation. Image fusion took an average of 14 ± 4 minutes for merging of the CT-scan, and 10 ± 6 minutes for merging the CMR scan. CSO visualization was successful in all patients that received a pre-procedural CT and had an overall fair agreement with the CSO at fluoroscopy images. There were no intra- or post-operative complications and no reported adverse effects on renal function.

LV implantation characteristics

The implantation characteristics and outcome data of patients who received real-time image-guided LV lead placement (target group) are displayed in **Table 2**. Total and LV implantation duration in this group were 146 ± 38 minutes and 47 ± 18 minutes respectively, fluoroscopy time was 36 ± 15 minutes. CRT implantation duration and fluoroscopy times were not statistically different from recent historical controls (185 ± 40 minutes, p = 0.07, and 27 ± 12 minutes, p = 0.17 respectively). Total radiation dose was 6758 ± 4201 cGy·cm^2, the radiation dose of the pre-implantation and post-implantation 3D-rotational scan were 1188 ± 262 cGy·cm^2 and 1313 ± 333 cGy·cm^2 (**Table 2**). The radiation dose of the CRT implantation without 3D-rotational scan was 5753 ± 3038 cGy·cm^2.

Results of image-guided CRT implantation

In all patients that received real-time image guidance, LV leads were placed out of scar, away from the LPN and within, or in close proximity to the CMR defined target area. In three out of six patients the LV lead was implanted within the target segment, in the other three patients, the LV lead was placed adjacent to the target area. In patients from the target group, LV leads were placed significantly closer to the target area compared to patients from the non-target group (8 mm [IQR: 0 – 22] versus 26 mm [IQR: 17 – 46], p = 0.04), while distance of the LV lead to scar and the LPN did not differ between groups. The electrical properties in the target group did not vary from the non-target group and they were as follows: mean pacing thresholds: 0.65 ± 0.39V vs 0.58 ± 0.20V, paced QRS duration: 153 ± 22 ms versus 170 ± 22 ms, change in QRS duration from baseline: -12 ± 13 ms versus -9 ± 27 ms, and QLV: 150 ± 8 ms versus 130 ± 30 ms (QLV/QRS ratio 85 ± 10% versus 81 ± 16) (**Table 2**). At six months follow up, all patients from the target group showed echocardiographic response to CRT with a mean LVESV change of -30 ± 10% and a mean LVEF improvement of 15 ± 5%.

Table 2: CRT implantation and follow up characteristics.

	TARGET group (n = 6)	NON-TARGET group (n = 9)	p-value
Distance to target sites			
Distance to target (mm)	8 [0-22]	26 [17-46]	0.04
Distance to infarct (mm)	22 [21-23] (n=2)	26 [14-51]	0.51
Distance to left phrenic nerve (mm)	44 [18-54]	44 [36-n/a]	0.61
Implantation characteristics			
Implantation duration (min)	146 ± 38	127 ± 35	0.38
LV lead implantation duration (min)	47 ± 18	55 ± 28	0.57
Fluoroscopy time (min)	36 ± 15	28 ± 12	0.30
Total radiation dose (cGy·cm2)	6758 ± 4201	8242 ± 6446	0.70
Pre-procedural 3D-angiogram radiation (cGy·cm2)	1188 ± 262	1449 ± 452	0.41
Post-procedural 3D-angiogram radiation (cGy·cm2)	1313 ± 333	1491 ± 439	0.57
Radiation dose CRT only (cGy·cm2)	5753 ± 3038	5303 ± 5847	0.91
LV lead electrical properties			
Paced QRS duration (ms)	153 ± 22	170 ± 22	0.18
Decrease QRS duration (ms)	-12 ± 13	-9 ± 27	0.10
Pacing threshold (V)	0.65 ± 0.39	0.58 ± 0.20	0.64
QLV (ms)	150 ± 8	130 ± 30	0.23
Ratio QLV/QRS (%)	85 ± 10	81 ± 16	0.66
Echocardiographic follow up			
LV end-systolic volume change (%)	-30 ± 10	-19 ± 19	0.28
LV ejection fraction change from baseline (%)	15 ± 5	10 ± 12	0.30

Values are in mean ± SD, median [interquartile range]. LV: left ventricular; QLV: Interval from Q on the surface ECG to local sensing at the LV electrogram

Discussion

This study demonstrates the feasibility of multimodality image fusion, for treatment planning and real-time image-guided LV lead delivery towards optimal pacing sites during CRT implantation procedures. Optimal pacing sites were pre-procedurally identified on CMR (i.e. latest contracting segment and scar location) and CT scans (i.e. anatomy of the LPN and CSO) and were intra-procedurally fused with live fluoroscopic projections. This allowed the implanting cardiologist to place the LV lead out of scar, away from the LPN and closer to the

CMR defined target area compared to CRT implantation without real-time image-guidance, while implantation duration and fluoroscopy time were not increased compared to historical controls.

Targeting LV lead towards predefined optimal pacing sites

Previous work demonstrated significantly more LV reverse remodeling, lower cardiac mortality and fewer heart failure hospitalizations in patients paced from within a target segment with significant electrical or mechanical delay.[2,3,6,14] Measuring the QLV is a relatively simple technique for assessing LV activation delay, however, it provides limited information of total LV electrical activation because usually measurements are only performed at the LV anatomical target region. CMR-scans on the other hand can provide detailed information with regards to mechanical dyssynchrony and myocardial scar location. This supports the role of CMR for image-guided LV lead delivery in patients undergoing CRT implantations. Yet, only two previous studies established real-time visualization of target areas on fluoroscopy images during CRT implantation.[15,16] Using a similar approach to our study, both studies showed the feasibility of real-time image-guided LV lead implantation. Importantly, they did not assess the course of the LPN, moreover, they assessed latest contracting segments by an automatic segmentation algorithm differentiating between the myocardium and the blood pool and in doing so assessed the time to minimum segmental endocardial volume. In our study, we used CMR-FT, the CMR equivalent of speckle-tracking echocardiography for contraction timing analysis. CMR-FT is a relatively easy technique for myocardial contraction timing analysis since the cine images are obtained during standard cardiac imaging protocols.[6,17] In validation studies CMR-FT showed good agreement with CMR-tagging, the gold standard technique for the non-invasive assessment of myocardial deformation which requires separate acquisition of images.[13,18]

In the present study, real-time image-guided LV lead implantation enabled placing the LV lead closer to the target segment compared to LV lead implantation without real-time image-guidance (treatment planning only). LV lead delivery within a pre-procedurally defined target segment, however, remains challenging. We were able to place three out of six LV leads within the CMR target segment using the overlay with fluoroscopy. The lack of

a suitable coronary vein at the target site can be an important factor that may prevent LV lead delivery to a target segment. Additionally, in the present study, we did not adhere to the American Heart Association (AHA) 17-segment to determine LV lead target segments,[19] but we performed the data processing into smaller LV segments and allowed the cardiologist to freely choose a subset of the LV segments to construct a well visible LV target area. Data processing into smaller segments allows for a more precise delineation of scar tissue, and subsequently, more precise target area definition. Placing the LV within a smaller target segment, however, is more challenging. Real-time image-guidance enabled us to place the LV lead as close to the target site as possible in all patients. Whether more precise targeting leads to improved CRT outcomes needs yet to be determined.

Limitations and challenges

This study was designed to demonstrate the feasibility of a novel treatment guidance platform for real-time visualization of optimal pacing sites during CRT implantation. Because the study was not designed or powered to demonstrate the superiority of real-time image-guided LV lead placement, no definite conclusions can be drawn regarding outcome data on implantation characteristics and end points. While, all patients that received real-time image-guided LV lead implantation were echocardiographic responder at follow up, other important factors probably have attributed to the high rate of reverse remodeling in patients from the target group. For instance, patients with persistent atrial fibrillation were excluded from study participation and patients from the target group had relatively favourable patient characteristics (e.g. more frequently LBBB, non-ICM and lower intracardiac volumes).

Furthermore, we recognize that a relatively high radiation dose was used due to the additional 3D-rotational scans and pre-implantation CT imaging. The radiation dose of the CRT implantation without 3D-rotational scans was comparable to previous work.[20,21] In the present study, 3D-rotational scans were acquired before and after CRT implantation, however for visualization of optimal pacing sites onto fluoroscopic projections, performing a single 3D-rotational scan is sufficient. This adds approximately 20% of radiation dose to a CRT implantation. Detrimental effects of radiation, occur at a dose area product larger than

40 000 cGy·cm^2 (assuming an effective radiation area of 100 cm^2)[20] whereas, the threshold dose for skin erythema is 20 000 cGy·cm^2.[21] Using CARTBox, in the present study radiation dose thus remained well below the above-mentioned thresholds. In addition, performing a CT-scan is not standard care in patients undergoing CRT device implantation and is associated with increased cost and a slightly increased healthcare risk due to ionizing radiation (average 20-80 cGy·cm^2) and the use of an iodinated contrast agent. Iodinated contrast agents may cause kidney dysfunction, especially in patients with pre-existing renal impairment. According to large, epidemiologically representative patient populations with chronic heart failure, about 10% of patients will have severe renal dysfunction (GFR < 30 ml·min·1.73 m^2).[22] Therefore, performing both a CT scan and a CRT implantation may not be feasible in all patients eligible for CRT. While the CARTBox platform can easily be implemented using CMR only, we chose to implement the CT scan in the current study, because visualizing the course of the LPN and CSO before implantation could potentially simplify CS cannulation, prevent LPN stimulation and accompanied LV lead relocation, and consequently, reduce implant times. Pre-procedural detailed evaluation of the coronary venous anatomy on CT images could take the concept for targeted LV lead implantation even further. However, the timing of the intravenous contrast administration to the venous phase is not a standard procedure and is especially difficult in heart failure patients. Furthermore, even when performed optimally, it does not permit the visualization of the smaller venous branches. Therefore in the present study, we did not evaluate the CS anatomy preoperatively on CT, but chose to use the CS venogram instead, which is acquired during CRT implantation and which is the current standard to visualize complete CS anatomy. Importantly, emerging technologies in CMR and CT scan protocols and image analysis algorithms (i.e. detection of myocardial scar and dyssynchrony on cardiac CT[23] and the anatomy of the LPN and coronary sinus on CMR[24]) could in the near future negate the necessity for both pre-procedural CMR and CT. This would especially be of value in patients with a contra-indication for CMR or CT, such as patients with impaired renal function, claustrophobia, documented allergy to gadolinium, or patients with non-MRI conditional devices.

Future implications

Despite the aforementioned challenges, and based on the superior patient outcomes of targeted LV lead placement, demonstrated by previous studies [2,3,6,15], we believe that the technology of real-time image-guided LV lead implantation towards optimal pacing sites is clinically promising. Technical advancements such as the development of the snare technique and octopolar LV leads, together with other pacing techniques, such as endocardial pacing, will probably allow for a more precise delivery of LV leads into predefined, smaller, target areas. While, the CARTBox toolbox can be further improved to enable widespread clinical application, technologies that enable visualization of optimal pacing sites, may become of high value for implanting physicians.

Conclusions

Real-time image-guided LV lead placement by fusion of CMR- and CT-images with fluoroscopy images during CRT device delivery is feasible and endorses placing the LV lead closer to the target segment and out of scar compared to treatment planning only. Merging of target segments on to live fluoroscopy can be performed rapidly without prolongation of procedure time. Further investigation of this technology in clinical practice with larger patient cohorts is necessary to determine whether real-time image-guided LV lead delivery leads to improved patient outcomes and whether this approach is cost effective.

Notes

Acknowledgements

The authors acknowledge Niels Blanken who contributed with the CMR scanning. CARTBox is a CE-certified software product.

Disclosures, Conflict of interest

Authors F.J. van Slochteren and P. Leufkens are co-founders and shareholders of CART-Tech B.V. M. Meine and F.J. van Slochteren are inventors and beneficiaries of a patent license arrangement between the University Medical Center Utrecht and CART-Tech B.V. according to the rules of the University Medical Center Utrecht. The other authors have no conflict of interest.

Ethical standards

This study has been approved by the appropriate ethics committee and has therefore been performed in accordance with the ethical standards laid down in the 1964 Declaration of Helsinki and its later amendments. Informed consent was obtained from all individual participants included in the study.

References

1. Daubert J-C, Saxon L, Adamson PB, Auricchio A, et al. 2012 EHRA/HRS expert consensus statement on cardiac resynchronization therapy in heart failure: implant and follow-up recommendations and management. *Hear Rhythm* 2012;**9**(9):1524–1576. doi:10.1016/j.hrthm.2012.07.025.

2. Saba S, Marek J, Schwartzman D, Jain S, et al. Echocardiography-Guided Left Ventricular Lead Placement for Cardiac Resynchronization Therapy: Results of the Speckle Tracking Assisted Resynchronization Therapy for Electrode Region Trial. *Circ Hear Fail* 2013;**6**(3):427–434. doi:10.1161/CIRCHEARTFAILURE.112.000078.

3. Khan FZ, Virdee MS, Palmer CR, Pugh PJ, et al. Targeted Left Ventricular Lead Placement to Guide Cardiac Resynchronization Therapy. *J Am Coll Cardiol* 2012;**59**(17):1509–1518. doi:10.1016/j.jacc.2011.12.030.

4. Leyva F. Cardiac resynchronization therapy guided by cardiovascular magnetic resonance. *J Cardiovasc Magn Reson* 2010;**12**(1):64. doi:10.1186/1532-429X-12-64.

5. Delgado V, Bommel RJ van, Bertini M, Borleffs CJW, et al. Relative Merits of Left Ventricular Dyssynchrony, Left Ventricular Lead Position, and Myocardial Scar to Predict Long-Term Survival of Ischemic Heart Failure Patients Undergoing Cardiac Resynchronization Therapy. *Circulation* 2011;**123**(1):70–78. doi:10.1161/CIRCULATIONAHA.110.945345.

6. Taylor RJ, Umar F, Panting JR, Stegemann B, Leyva F. Left ventricular lead position, mechanical activation, and myocardial scar in relation to left ventricular reverse remodeling and clinical outcomes after cardiac resynchronization therapy: A feature-tracking and contrast-enhanced cardiovascular magnetic r. *Hear Rhythm* 2016;**13**(2):481–489. doi:10.1016/j.hrthm.2015.10.024.

7. Es R van, Broek HT van den, Naald M van der, Jong L de, et al. Validation of a novel stand-alone software tool for image guided cardiac catheter therapy. *Int J Cardiovasc Imaging* 2019;**0**(0):0. doi:10.1007/s10554-019-01541-9.

8. Brignole M, Auricchio A, Baron-Esquivias G, Bordachar P, et al. 2013 ESC Guidelines on cardiac pacing and cardiac resynchronization therapy. *Eur Heart J* 2013;**34**(29):2281–2329. doi:10.1093/eurheartj/eht150.

9. Gho JMIH, Es R van, Slochteren FJ van, Jansen of Lorkeers SJ, et al. A systematic comparison of cardiovascular magnetic resonance and high resolution histological fibrosis quantification in a chronic porcine infarct model. *Int J Cardiovasc Imaging* 2017;**33**(11):1797–1807. doi:10.1007/s10554-017-1187-y.

10. Pedrizzetti G, Claus P, Kilner PJ, Nagel E. Principles of cardiovascular magnetic resonance feature tracking and echocardiographic speckle tracking for informed clinical use. *J Cardiovasc Magn Reson* 2016;**18**(1):1–12. doi:10.1186/s12968-016-0269-7.

11. Taylor RJ, Moody WE, Umar F, Edwards NC, et al. Myocardial strain measurement with feature-tracking cardiovascular magnetic resonance: Normal values. *Eur Heart J Cardiovasc Imaging* 2015;**16**(8):871–881. doi:10.1093/ehjci/jev006.

12. Morton G, Schuster A, Jogiya R, Kutty S, et al. Inter-study reproducibility of cardiovascular magnetic resonance myocardial feature tracking. *J Cardiovasc Magn Reson* 2012;**14**(1):1. doi:10.1186/1532-429X-14-43.

13. Moody WE, Taylor RJ, Edwards NC, Chue CD, et al. Comparison of magnetic resonance feature tracking for systolic and diastolic strain and strain rate calculation with spatial modulation of magnetization imaging analysis. *J Magn Reson Imaging* 2015;**41**(4):1000–1012. doi:10.1002/jmri.24623.

14. Zanon F, Baracca E, Pastore G, Fraccaro C, et al. Determination of the longest intrapatient left ventricular electrical delay may predict acute hemodynamic improvement in patients after cardiac resynchronization therapy. *Circ Arrhythmia Electrophysiol* 2014;**7**(3):377–383. doi:10.1161/CIRCEP.113.000850.

15. Shetty AK, Duckett SG, Ginks MR, Ma Y, et al. Cardiac magnetic resonance-derived anatomy, scar, and dyssynchrony fused with fluoroscopy to guide LV lead placement in cardiac resynchronization therapy: A comparison with acute haemodynamic measures and echocardiographic reverse remodelling. *Eur Heart J Cardiovasc Imaging* 2013;**14**(7):692–699. doi:10.1093/ehjci/jes270.

16. Behar JM, Mountney P, Toth D, Reiml S, et al. Real-Time X-MRI-Guided Left Ventricular Lead Implantation for Targeted Delivery of Cardiac Resynchronization Therapy. *JACC Clin Electrophysiol* 2017; doi:10.1016/j.jacep.2017.01.018.

17. Harrild DM, Han Y, Geva T, Zhou J, et al. Comparison of cardiac MRI tissue tracking and myocardial tagging for assessment of regional ventricular strain. *Int J Cardiovasc Imaging* 2012;**28**(8):2009–2018. doi:10.1007/s10554-012-0035-3.

18. Everdingen WM van, Zweerink A, Nijveldt R, Salden OAE, et al. Comparison of strain imaging techniques in CRT candidates: CMR tagging, CMR feature tracking and speckle tracking echocardiography. *Int J Cardiovasc Imaging* 2018;**34**(3):443–456. doi:10.1007/s10554-017-1253-5.

19. Cerqueira MD, Weissman NJ, Dilsizian V, Jacobs AK, et al. Standardized myocardial segmentation and nomenclature for tomographic imaging of the heart. *J Cardiovasc Magn Reson* 2002;**4**(2):203–210. doi:10.1081/JCMR-120003946.

20. Butter C, Schau T, Meyhoefer J, Neumann K, et al. Radiation exposure of patient and physician during implantation and upgrade of cardiac resynchronization devices. *PACE - Pacing Clin Electrophysiol* 2010;**33**(8):1003–1012. doi:10.1111/j.1540-8159.2010.02765.x.

21. Perisinakis K, Theocharopoulos N, Damilakis J, Manios E, et al. Fluoroscopically Guided Implantation of Modern Cardiac Resynchronization Devices. *J Am Coll Cardiol* 2005;**46**(12):2335–2339. doi:10.1016/j.jacc.2005.01.070.

22. Cleland JGF, Carubelli V, Castiello T, Yassin A, et al. Renal dysfunction in acute and chronic heart failure: Prevalence, incidence and prognosis. *Heart Fail Rev* 2012;**17**(2):133–149. doi:10.1007/s10741-012-9306-2.

23. Behar JM, Rajani R, Pourmorteza A, Preston R, et al. Comprehensive use of cardiac computed tomography to guide left ventricular lead placement in cardiac resynchronization therapy. *Hear Rhythm* 2017;**14**(9):1364–1372. doi:10.1016/j.hrthm.2017.04.041.

24. Duckett SG, Chiribiri A, Ginks MR, Sinclair S, et al. Cardiac MRI to investigate myocardial scar and coronary venous anatomy using a slow infusion of dimeglumine gadobenate in patients undergoing assessment for cardiac resynchronization therapy. *J Magn Reson Imaging* 2011;**33**(1):87–95. doi:10.1002/jmri.22387.

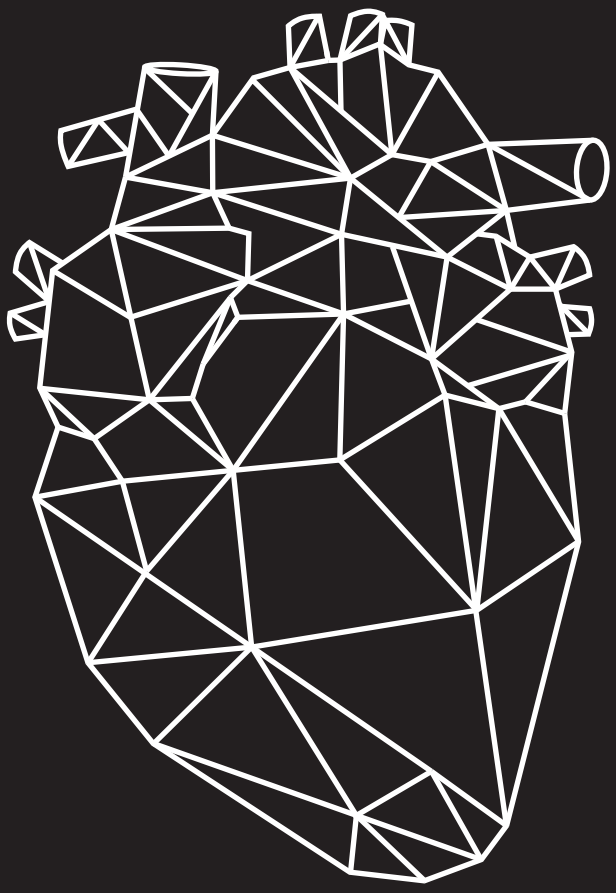

Chapter 6

3D Myocardial Scar Prediction Model Derived from Multimodality Analysis of Electromechanical Mapping and Magnetic Resonance Imaging

Journal of Cardiovascular Translational Research, 2019, accepted

HT. van den Broek MSc [1], S. Wenker MD 1, R. van de Leur BSc [1], P.A. Doevendans MD PhD [1,2], S.A.J. Chamuleau MD PhD [1], F.J. van Slochteren PhD [1]*, R. van Es PhD [1]*
* These authors contributed equally to this work

[1] Department of Cardiology, University Medical Center Utrecht, Utrecht, The Netherlands
[2] Netherlands Hearts Institute / Central Military Hospital Utrecht, Utrecht, The Netherlands

Abstract

Many cardiac catheter interventions require accurate discrimination between healthy and infarcted myocardium. The gold-standard for infarct imaging is late-gadolinium enhanced MRI (LGE-MRI), but during cardiac procedures electroanatomical or electromechanical mapping (EAM/EMM, respectively) is usually employed. We aimed to improve the ability of EMM to identify MI by combining multiple EMM-parameters in a statistical model. From a porcine infarction model, 3D electromechanical maps were 3D registered to LGE-MRI. A multivariable mixed-effects logistic regression model was fitted to predict the presence of infarct based on EMM-parameters. Furthermore, we correlated feature-tracking strain-parameters to EMM-measures of local mechanical deformation. We registered 787 EMM-points from 13 animals to the corresponding MRI-locations. The mean registration error was 2.5 ± 1.16 mm. Our model showed a strong ability to predict the presence of infarction (C-statistic = 0.85). Strain-parameters were only weakly correlated to EMM-measures. The model is accurate in discriminating infarcted from healthy myocardium. Unipolar and bipolar voltage were the strongest predictors.

Introduction

For many cardiac catheter interventions, accurate discrimination between healthy and infarcted myocardium is crucial.[1] For example, ablation of ventricular tachycardia may require ablation lesions to be placed in and around the myocardial infarction (MI) area to eliminate electrical signals conducted via viable cells contributing to the arrhythmia.[2] Furthermore, in trials evaluating cardiac regenerative therapy, therapeutics are often targeted specifically to the infarct border zone.[3] The current gold-standard for infarct imaging is late gadolinium-enhanced magnetic resonance imaging (LGE-MRI). Pre-procedural LGE-MRI may inform operators about the location of the diseased areas, but reviewing MRI data pre-procedurally is not sufficient to ensure accurate identification of target tissue intra-procedurally.[4] Both interventional MRI[5] and image fusion techniques[6,7] are active fields of research that offer the possibility to incorporate MR-imaging during interventional procedures. However, MRI guidance for cardiac treatment is currently not widely available and, therefore, interventional cardiologists in clinical practice have to rely on other techniques to identify target tissues intra-procedurally.

Within electrophysiology, electroanatomical mapping (EAM) is the standard technique to identify the origin of arrhythmia and to distinguish healthy from scarred myocardium.[8,9] This technique is performed using a mapping catheter that is positioned inside the left ventricle (LV) and that is able to measure local electrical characteristics of the myocardium.[10] Using three magnetic fields, the system is able to deduct the position of the catheter and register the measurements to a 3D location. Electromechanical mapping (EMM) is an extension of this technique that allows for measurements of local mechanical properties as well.[11] Using these measurements, a 3D electromechanical map of the LV can then be constructed.

Previous research evaluated the ability of (individual) EAM/EMM-parameters to discriminate between areas of MI and healthy tissue, using LGE-MRI as the gold standard.[12–15] In practice, MI is not a dichotomous phenomenon. Interspersed between areas that are healthy and areas that are completely infarcted (transmurally infarcted), are often areas in which the infarction does not extend completely through the myocardial wall (non-transmural infarction). Research has shown that different individual EMM parameters

identify different regions of the MI and the threshold of infarct transmurality at which the parameters offer the best diagnostic accuracy differs between the varying parameters.[13–15] For example, one study found that unipolar voltage (UV) best discriminates at a threshold of 5% infarct transmurality, while bipolar voltage (BV) has the highest diagnostic accuracy at a threshold of 97.5% transmurality.[15] Because MI is heterogeneous of nature and individual EMM parameters enable the differentiation of distinct regions, we propose that a prediction model that incorporates multiple EMM parameters could improve the detection and differentiation of MI.

Strain analysis, MRI feature tracking (MRI-FT), allows quantification of myocardial deformation on MRI. While other advanced deformation imaging methods require additional, often time-consuming imaging sequences, FT is based on standard cine MR imaging sequences that are routinely acquired. The reduced mechanical activity coincides with myocardial scar on LGE-MRI[16] and is even a sensitive marker for sub-clinical myocardial dysfunction.[17] However, as of yet, there is no data comparing the resulting strain parameters with EMM-derived parameters of local mechanical activity (local linear shortening (LLS) and local activation time (LAT)).

In this retrospective study, we investigated the use of a logistic prediction model based on multiple EMM-parameters to distinguish infarcted from healthy myocardium with the most accuracy, and we evaluated the predictive accuracy of this model in a porcine model of chronic MI. Furthermore, we compared the EMM-derived parameters of local mechanical activity to MRI-FT derived parameters.

Methods

Animals

We re-analyzed thirteen EMM and MRI datasets acquired in a porcine model of chronic MI. The experiments have been described in more detail previously.[15,18] In short, MI was induced by 90-minute occlusion of the left anterior descending coronary artery distal to the second diagonal branch.

Data acquisition

Electromechanical mapping (EMM)

The EMM procedure was described in detail previously.[15] In short, the NOGA® XP system (Biosense Webster, Johnson & Johnson, Diamond Bar, USA) was used to create an EMM of the LV by using a conventional 7 French deflectable-tip mapping catheter (NogaStar, Biosense Webster). Under fluoroscopy guidance, the catheter was introduced into the LV after retrograde passage through the aortic valves. To ensure complete LV endocardium coverage, EMM parameters (UV, BV, LAT, and LLS) were recorded at 80 to 200 LV endocardial locations. Electrocardiograms were filtered at 30–400Hz (bipolar) and 1–240Hz (unipolar). EMM measurement points were accepted if they were triggered on the R-wave in combination with acceptable catheter stability, in accordance with the criteria for good electromechanical mapping.[11]

MRI acquisition

Detailed acquisition settings can be found in the appendix. CMR images were acquired using a 1.5T Ingenia system and a 3T Achieva XT system (Philips Healthcare, Best, The Netherlands). Imaging planes were selected according to standard cardiac views (four-chamber, two-chamber, and short-axis view). Fifteen minutes after injection of 3.0 mmol/kg gadolinium an LGE inversion-recovery sequence was acquired in the short-axis orientation.

Data processing

Image segmentation

LV segmentations were created using Segment for Matlab (version 2.1 R5768).[19] Automatic segmentation of the epicardial and endocardial contours was performed on the short axis cine-images in the end-diastolic phase and end-systolic phase. Segmentation quality was visually assessed using long-axis images and adjusted if necessary. Wall thickness was measured on the short axis cine-images. Wall thickening (WT) was calculated as the difference between wall thickness in the end-diastolic and end-systolic phase. Fractional wall thickening (WT%) was calculated relative to the end-diastolic phase wall thickness.

Automatic identification, segmentation, and quantification of LGE lesions were performed using the full-width at half maximum (FMWH) algorithm. Area-based infarct transmurality (TM), WT and WT% values were calculated in 80 circumferential segments per slice. In all segmentation steps, manual correction was performed if necessary.

Strain analysis

Myocardial deformation analysis was performed on short-axis cine images using FT software (TomTec Arena, 2D Cardiac Performance Analysis MR, version 1.2, Unterschleissheim, Germany). Circumferential strain curves were exported into a custom Matlab script to automatically determine time-to-peak-strain (TTP_{max}) and maximum strain ($strain_{max}$) for 48 sectors per slice. Identification of the timing-of-onset (T_{onset}) was performed using a modified algorithm for estimation of the onset time of shortening as described in the appendix.[20] To prevent erroneous strain values in akinetic sectors affected by MI due to poor tracking of the image features, sectors with mean strain values below a pre-determined -7.5% threshold were excluded from the strain analysis. The sectors were included in the univariable linear analysis as akinetic sectors.

Image registration

A 3D surface mesh was constructed from the end-diastolic LV cine MRI segmentation. The EMM points were registered to this mesh based on iterative closest point (ICP) algorithm.[21] The registration was manually optimized if necessary. **Figure 1** shows an example of the registration of the LV-endocardial mesh with EMM-points. The algorithm and registration steps have previously been described in detail.[22] Registration error was expressed as the shortest distance of each EMM point to the closest point on the mesh surface. As a first step of the registration both datasets where placed in patient coordinates, and the apex of both the EMM data and the 3D surface mesh were registered. Furthermore, during the ICP registration the rotation parameter was constrained to 10 degrees. EMM-points that were located more basal than the most basal segmentation of the MR-images (and therefore also outside of the mesh) were excluded.

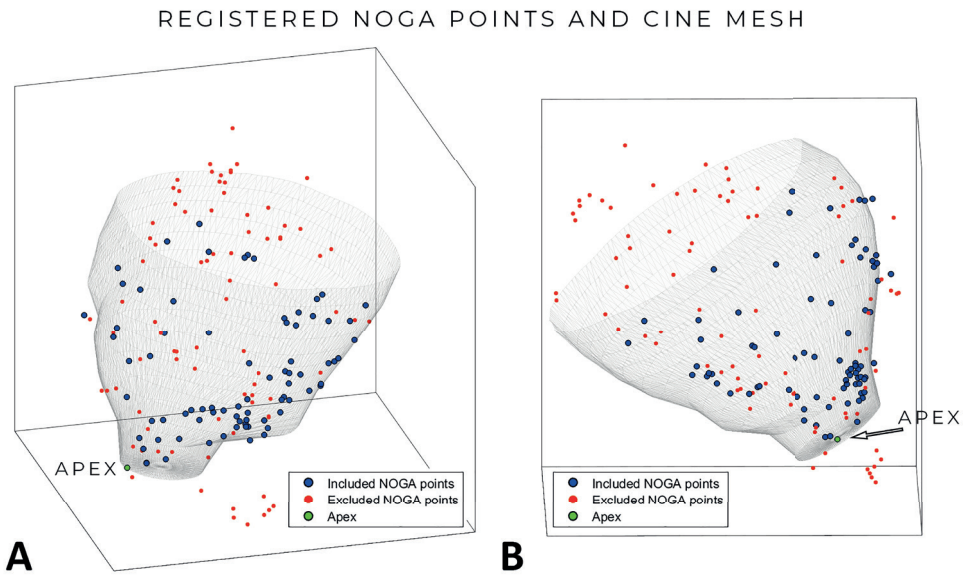

Figure 1: Projection of the NOGA-derived EMM-points on the endocardial surface mesh created from the MR-images in LAO (**A**) and RAO (**B**) view Red points are excluded based on their distance (>5 mm) to the mesh.

After the EMM-MRI registration, MRI-derived (WT, WT%, TM) values were calculated for each EMM point as an inverse distance weighted average of all vertices of the surface mesh within 5mm. EMM points without vertices within the 5mm range were excluded for the model.

Statistical analysis

Scar prediction model

Infarct transmurality was dichotomized at a threshold of 50%. A multivariable prediction model for scar location on MRI with the EMM parameters as input was fitted using a logistic mixed-effects model with a random intercept per subject. All EMM-parameters were scaled and centered and used as predictors in the model. Backward predictor selection was performed using Akaike's Information Criterion (AIC). 95% confidence intervals around the odds ratios were derived using 500 bootstrap samples for all models.[23]

Predicted probabilities for scar were derived using the fixed effects and a mean random intercept since the random cluster effect will be unknown for new subjects. Performance of the prediction model (i.e. discrimination and calibration) was assessed using the C-statistic (equivalent to the area under the receiver operating curve) and calibration slope. The within-subject C-statistic was estimated as a mean of the C-statistic for each subject (i.e. each animal), weighted for the amount of EMM points per subject.[24] The within-subject calibration slope was derived from a logistic mixed-effects model with a random slope for the linear predictor and random intercept per subject.[25] Considering the small number of subjects, internal validation and correction for optimism in performance were performed using bootstrapping (n = 500) of individual data points (in contrast to bootstrapping complete clusters as would be preferable with a large number of subjects). A more comprehensive description of the internal validation approach can be found in supplementary information 2.

Correlating EMM-parameters to feature tracking

A univariable linear mixed-effects model, with a random intercept per subject, was fitted for a one-to-one comparison of EMM parameters with MRI-parameters. A fixed-effect R-squared value is a statistical measure that represents the reduction in residual variance after adding parameters to a null model with only the random intercept. We approximated these values using a method as described by Snijders and Bosker.[26]

All statistical analyses were performed using *R* (version 3.5, R Foundation for Statistical Computing, Vienna, Austria)[27] and the *lme4* package.[28] Data are presented as mean±SD or median with interquartile range (IQR) where appropriate. Point estimates are presented with a 95% confidence interval in square brackets. A p-value of <0.05 was considered statistically significant.

Table 1: Results of cine and late gadolinium enhancement magnetic resonance imaging of 15 animals.

LV volumetric		
LV end-diastolic volume	110.7 ± 20.2	(ml)
LV end-systolic volume	59.5 ± 17.1	(ml)
LV ejection fraction	47.3 ± 9.7	(%)
Heart rate	54 ± 8	(bpm)
LV mass	118.2 ± 20.5	(g)
Infarct mass	16.8 ± 6.5	(g)
Infarct size	28.3 ± 12.3	(%)

All results are presented in mean ± standard deviation.

Results

Imaging

Chronic MI was present in all animals at the time of the EMM procedure as evidenced by a clear hyperintense area on LGE-MRI. In all animals, the infarctions were located apicoseptal and mid-apicoanterior. The MRI results are summarized in **Table 1**.

After dichotomization the mean endocardial surface area for MI was 18.5 ± 8.2 cm^2 compared to 66.6 ± 10.2 cm^2 for healthy tissue, thereby covering 21.2 ± 8.4% and 78.8 ± 8.4% of the total LV respectively. The mean infarct volume was 17.2 ± 5.3 cm^3.

An average of 49.1 ± 25.3 sectors were filtered in the strain analysis and marked as akinetic sectors, thereby covering 13.2 ± 6.9% of the total LV. In healthy tissue the median circumferential $strain_{max}$ was -26.0% (IQR = -34.9, -17.6) and within myocardial scar the median value was -15.7% (IQR = -25.3, -9.0).

Image registration

EMM points were homogeneously distributed over the LV endocardial surface. The total number of EMM points in the 13 datasets after filtering was 1459 (112 ± 41 per subject) and these were used for registration and projection. Of the registered points, 672 (46,1%) were not located within 5 mm of the mesh and were excluded from the model. The resulting registration error, after exclusion of these points, was 2.5 ± 1.2 mm. Ultimately high density maps with a total of 787 (61 ± 19 per subject, on average 5.0 ± 1.6 points per segment) points were matched to corresponding MR-derived values and were used for fitting the model.

Linear relationships between EMM and LGE-MRI

We assessed the relationship between T_{onset}, TTP_{max} and LAT time as well as between (fractional) WT, $strain_{max,}$ and LLS. Results from the univariable linear regression analysis are shown in the supplemental data**.** Both T_{onset} and TTP_{max} were significantly correlated with LAT (p=0.05 and p=0.02 respectively) and WT, fractional WT, and $strain_{max}$ were all statistically significant predictors of LLS (p<0.001 for all), although in all these correlations the explained variance was small (R^2-values ranged between 0.006 and 0.029).

Table 2: Odds ratio results of the multivariable logistic mixed model analysis for four EMM parameters.

Parameter	Odds ratio	
Unipolar voltage	0.14	[0.08 – 0.21]
Bipolar voltage	0.36	[0.23 – 0.52]
Local linear shortening	0.76	[0.61 – 0.92]
Local activation time	0.80	[0.61 – 1.06]

All results are presented in odds ratio with 95% Confidence Interval.

Table 3: Internal validation results of the multivariable prediction model.

Original c-statistic	0.85 [0.82 – 0.89]
Optimism-corrected c-statistic	0.84
Original slope	1.10 [1.00 – 1.21]
Optimism-corrected slope	1.01

Data is presented as the point estimate with 95% confidence interval.

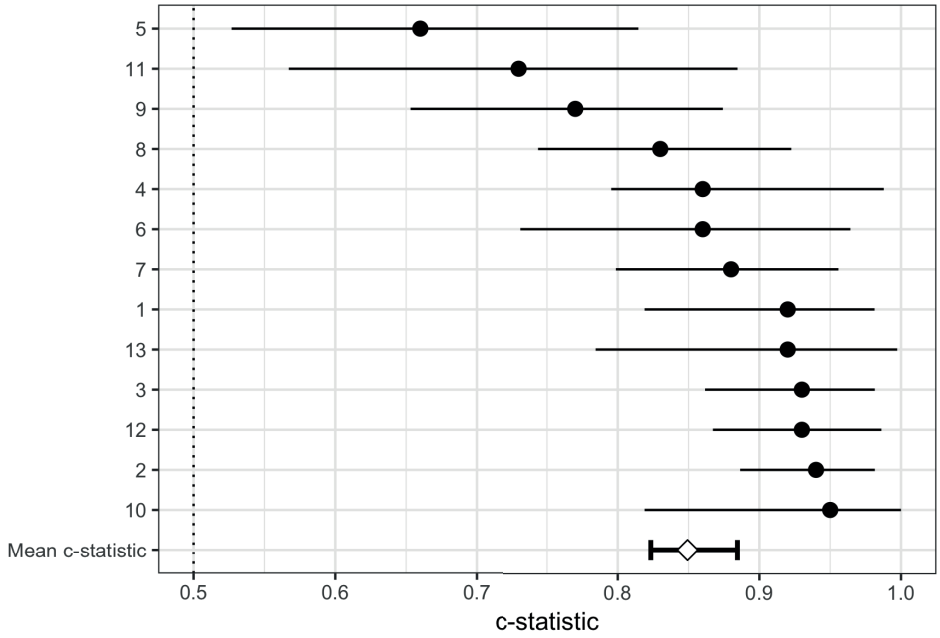

Figure 2: The within-subject model discrimination with 95% CI and the mean weighted c-statistic. Subject numbers are shown on the Y-axis.

Prediction model

The odds ratios (OR) of the normalized EMM parameters are shown in **Table 2**. UV, BV, and LAT were statistically significant predictors for the presence of myocardial scar on LGE-MRI. In our dataset, UV was the strongest predictor for myocardial scar (OR = 0.14 [0.08 – 0.21]) followed by BV (OR = 0.36 [0.23 – 0.52]). The association with scar was less pronounced for LLS (OR = 0.76 [0.61 – 0.92]) and did not reach statistical significance for LAT (OR = 0.80 [0.61 – 1.06]). The combination of UV, BV, LLS, and LAT shows a strong predictive ability to discriminate between scar and no scar (C-statistic = 0.85 [0.82 – 0.89]). Internal validation of the prediction model showed a comparable optimism-corrected C-statistic value 0.84 and good calibration (calibration slope = 1.01), as shown in **Table 3**. Within-subject results of the multivariable logistic mixed model (evaluated without the random intercept) can be appreciated from **Figure 2**. The sensitivity and specificity of the combined EMM parameters to distinguish between scar and no scar were 72% and 85%.

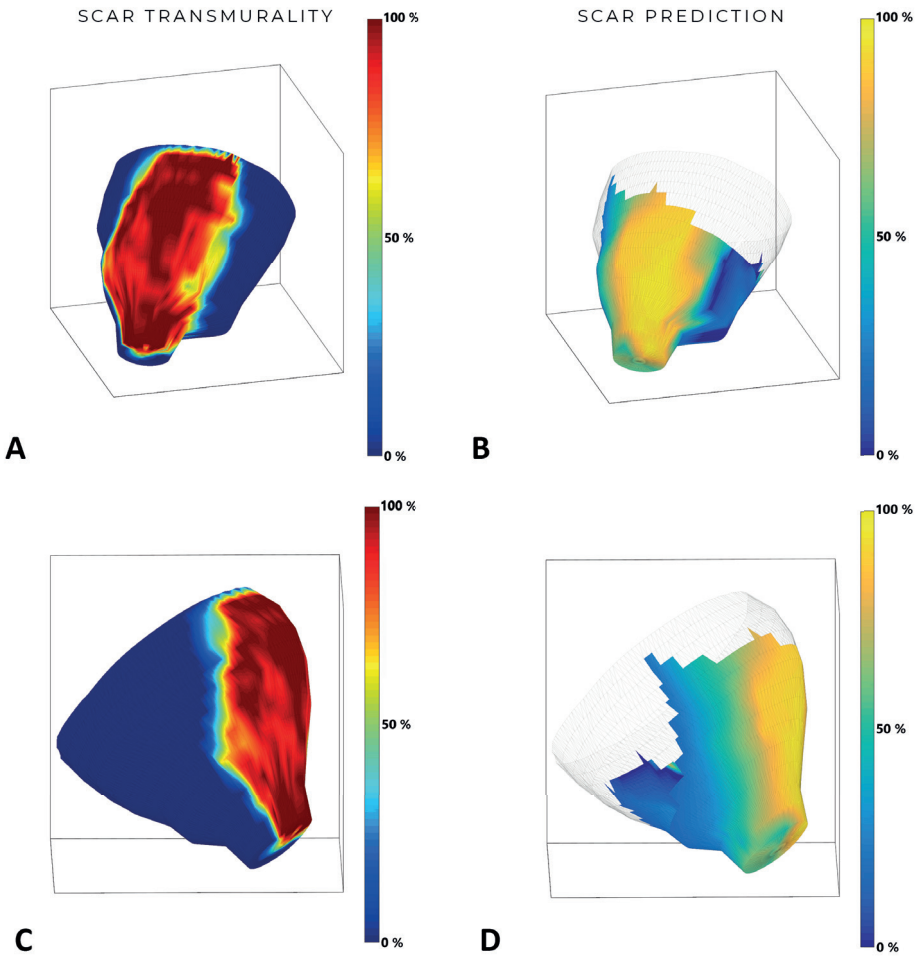

Figure 3: The LGE-MRI derived scar transmurality versus the NOGA predicted SCAR model for animal 2. **A** and **C**: LGE-MRI derived myocardial infarct transmurality projected on a cine surface mesh. The values of the scar transmurality are reflected in the colorbar. **B** and **D**: Predicted scar transmurality based on EMM-derived parameters projected on a cine surface mesh. The values of the predicted scar transmurality are reflected in the colorbar.

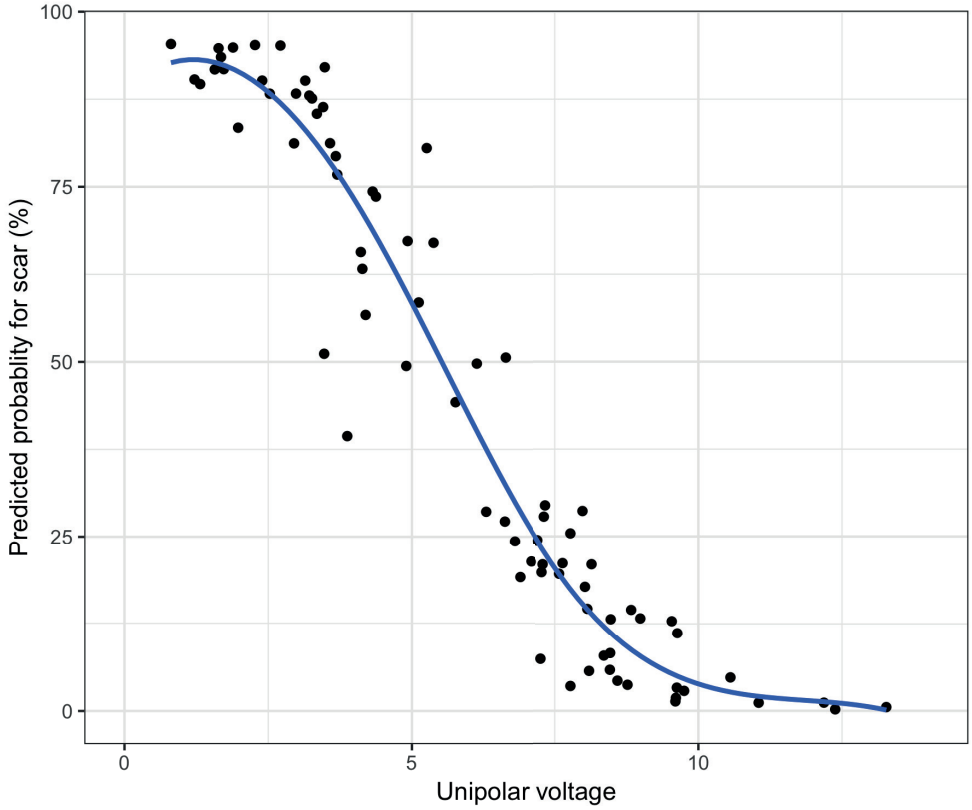

Figure 4: Predicted probability plot for myocardial scar determined by unipolar voltage for one for the animals (subject 2).

The relationship between the predictions made by our model and the presence of scar on MRI can visually be appreciated from **Figure 3**, which shows both the MRI-derived values plotted on the mesh (A and C) and the prediction of our model (B and D) for one of the animals. The predicted probabilities of scar, for the same animal, is plotted in **Figure 4** as a function of unipolar voltage. **Figure 5** shows the relationship between the predicted probability of the model and the actual transmurality.

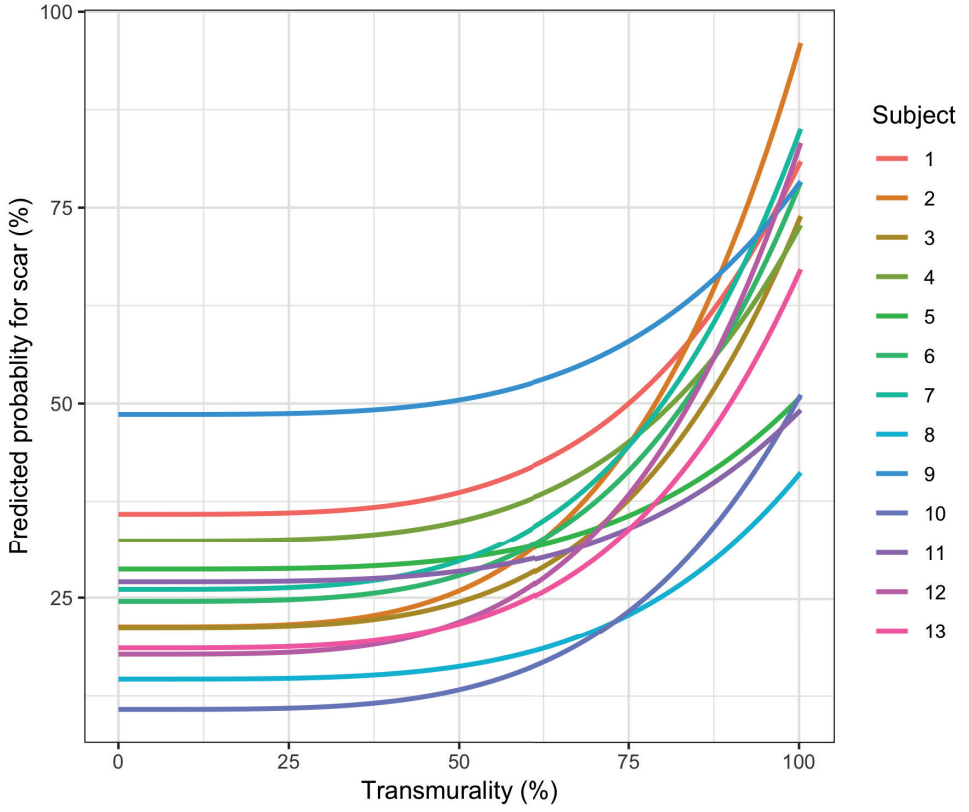

Figure 5: Relationship of the predicted probabilities by the full model with the transmurality percentage.

Discussion

In this study, 13 NOGA and MRI datasets of a porcine model of chronic MI were retrospectively analyzed. Parameters derived from electromechanical mapping (UV, BV, LAT, LLS) were registered in 3D and combined with MRI parameters in a multivariate mixed model for prediction of myocardial scar. The animal model used in this study provided large transmural myocardial infarct areas with only small non-transmurally infarcted areas. To prevent the effect introduced by the variation of samples measured in the small non-transmurally infarcted areas on the model, the outcome parameter was dichotomized to transmural infarction or healthy myocardium and logistic regression was fitted. Consequently, the resulting scar prediction model has the highest predictive ability to discriminate between infarcted and non-infarcted myocardium.

The accuracy of the electromechanical map depends on the number, quality, and distribution of the measurements acquired. A homogenous distribution of EMM points importantly determines the result of the interpolation between measurement points and thus the accuracy of the 3D map. Because the NOGA-system only acquires a single point per measurement, the mapping procedure requires time and patience to create complete and representative maps. A strength of our study is the high density of the acquired NOGA-maps. In all animals, the electromechanical maps were more densely populated than the recommended minimum of 3 points per cardiac segment[11] allowing accurate comparison to MR-images over a large number of sampled points. Even though electromechanical maps with an overall high number of points were used in this study, the shape of the EMM surface mesh is interpolated between the measured points and, therefore, never exactly represents the LV endocardial surface. Furthermore, because MR and EMM are not performed at the same time, hemodynamic- and LV filling conditions may have changed between the two individual data acquisitions. Aforementioned factors inevitably result in a registration error.

To fit a statistical model that predicts transmurality from EMM-parameters, it is important to match the EMM-parameters to the transmurality values of the same location. Therefore, it is important to keep the registration error as low as possible. The registration error in our study is lower than in previous publications that used a similar approach (3.0 ± 1.9 mm[15] and 4.6 ± 3.6 mm[12]). Although there is no generally accepted cutoff we consider the registration error to be well within the acceptable range.

The overall model based on multiple EMM parameters shows a good predictive ability to identify areas with scar on LGE-MRI. From **figure 2** we can appreciate that the predictive accuracy was very good in most animals. In one subject (animal 5) the model performed moderate. This might be due to a residual registration error. In one of the animals (subject number 1), all UV-values (both in healthy and infarcted myocardium) were significantly lower than the values the rest of the dataset while BV, LLS, and LAT values were within normal ranges. The reason for this is unknown. Accurate prediction in this animal was preserved because UV values were still consistently lower within scar than within healthy tissue. Previous research demonstrated poor overlap between the individual EMM-derived parameters and LGE-MRI derived TM. However, due to the dichotomization of the TM and

use of a logistic mixed-model used in this study, direct comparison between the two studies is not possible.

In this study we used LGE-MRI as the gold standard for scar detection. Therefore, we could not perform a comparison between accuracy in detecting scar between LGE-CMR and our model. Despite the NOGA-derived measurements of local mechanical activity and MR-derived values of local mechanical activity were statistically correlated, they showed at best very weak correlations. Even though circumferential strain and LLS are fundamentally different quantities, both are thought to represent local mechanical myocardial function.[29] In previous research, both were shown to correlate with the myocardial scar on LGE-MRI.[16,30] It is therefore surprising to find only a weak correlation between these parameters. Although we can never exclude registration error as a possible explanation, the performance of our scar prediction model makes that unlikely to be the only explanation. Another possibility is that MRI-FT, even though its reasonably agreement with MRI tagging[31], has difficulties tracking features in the circumferential direction since in the circumferential direction there is less contrast in the direction of the myocardial deformation. A more in-depth evaluation of the relationship between strain and LLS is an interesting topic for future research.

In human subjects, the normal value for the global circumferential strain is estimated to be -23% (95% CI: -24.3% to -21.7%).[32] Reference ranges for endocardial circumferential strain in pigs (in either healthy pigs or in a porcine model of MI) have not been previously described. In the literature, various thresholds for circumferential strain have been reported to differentiate between infarcted and non-infarcted segments, for example, Ogawa *et al* found a sensitivity of 72% a specificity of 71% at a cutoff of -11,2%.[16,33] Our group has previously shown FT-derived strain has moderate ability to discriminate healthy from scarred myocardium.[34] In the current study, absolute values for endocardial circumferential strain were higher than expected within both healthy and infarcted myocardium. However, the scar area presented lower average circumferential strain values than in the healthy myocardial segments. Analysis of the diagnostic capability of endocardial circumferential strain to detect MI was not performed.

We calculated circumferential strain in 48 segments per short axis slice, compared to the usual practice of defining the 6 anatomical cardiac segments per short axis slice. This method allows us to compare strain parameters with increased accuracy, but is also more sensitive to errors in the FT analysis, segmentation, and image registration. Furthermore, recent studies have shown that intervendor agreement and intravendor reproducibility for MRI strain analysis is at most reasonable.[35,36] Comparing strain results from this study with results from studies in literature and previous studies from our department may, therefore, not be comparable and must be performed with caution.

Limitations

The animal model used in this study provides large transmural myocardial infarcted areas resulting in small areas with non-transmurally infarcted tissue. Therefore, we excluded the non-transmurally infarcted tissue and dichotomized the resulting measurements to fit a multivariable, mixed effects model. This model predicts the likelihood of finding an infarction at a given location based on all EMM parameters. In **figure 5** we show the relation between the predicted transmurality and presence of scar as a continuous variable. It seems plausible that intermediate likelihood for the presence of scar predicted by our model correspond to non-transmural infarction on MRI, but the model was not calibrated towards those predictions and we were not able to verify the performance of the model in areas with intermediate scar transmurality.

Future research should evaluate the performance of our model in a clinical dataset. In a clinical dataset a linear model and a dataset which includes non-transmural infarctions might be better suited to predict areas with non-transmural infarction.

Clinical implications

LGE-MRI is considered the gold-standard imaging tool for localization of myocardial scar. However, MRI is unavailable in many cardiac disease patients, such as in patients with an implantable cardioverter defibrillator or in patients with advanced renal failure. Furthermore, when preprocedural LGE-MRI images are available, tools for intraprocedural image fusion are not widely available. Modern EAM systems provide the functionality to derive the cardiac anatomy from pre-procedural imaging (e.g. cardiac MRI) but scar

information is not extracted. Therefore electrophysiologists often use EAM to identify scarred regions of the myocardium based on bipolar voltage. A more elaborate model, using all parameters gathered during the mapping procedure, may improve scar identification. The presented scar prediction model enables more accurate differentiation between healthy and infarcted myocardium based on a combination of all EMM-parameters and may be instrumental in improving cardiac procedures such as application of regenerative therapy, ablation of ventricular arrhythmia or cardiac biopsy. For example, several studies have proposed the use of EAM to guide endocardial biopsy procedures and showed improved biopsy yield compared to the X-ray guided approach.[37,38] Both studies highlighted the differences in identification capabilities of diseased myocardium by different EAM parameters and suggest a combination of multiple parameters to further improve identification of diseased or infarcted myocardium. Furthermore, EMM is the clinical standard for trans-endocardial delivery of cardiac regenerative therapy into the myocardial infarct border zone[39] and continues to be used in multiple current studies[3]. A recent publication suggested that EAM-guided LV-lead implantation improves response to cardiac resynchronization.[40] An additional advantage is the ability to directly identify the area of latest activation on the LV endocardium using EAM during the implantation.

Conclusion

The scar prediction model, based on the combination of unipolar voltage, bipolar voltage, local activation time and linear local shortening by NOGA, can accurately distinguish areas with MI from healthy myocardium as defined by LGE-MRI. In this dataset, unipolar voltage and bipolar voltage were the strongest predictors for the presence of MI. In the future, the scar prediction model may prove to be useful in VT-ablations, biopsy procedures, or regenerative therapy. Surprisingly, EMM-derived parameters were not significantly correlated with MRI-derived strain parameters.

References

1. Marchlinski FE, Callans DJ, Gottlieb CD, Zado E. Linear Ablation Lesions for Control of Unmappable Ventricular Tachycardia in Patients With Ischemic and. *Control* 2006;1288–1296.

2. Verma A, Verma A, Marrouche NF, Marrouche NF, et al. Relationship Between Successful Ablation Sites and the Scar Border Zone Defined by Substrate Mapping for Ventricular Tachycardia Post-Myocardial Infarction - VERMA - 2005 - Journal of Cardiovascular Electrophysiology - Wiley Online Library. *J …* 2005;(November 2004):465–471. doi:10.1111/j.1540-8167.2005.40443.x.

3. Paitazoglou C, Bergmann MW, Vrtovec B, Chamuleau SAJ, et al. Rationale and design of the European multicentre study on Stem Cell therapy in IschEmic Non-treatable Cardiac diseasE (SCIENCE). *Eur J Heart Fail* 2019;1–10. doi:10.1002/ejhf.1412.

4. Rogers T, Ratnayaka K, Karmarkar P, Campbell-Washburn AE, et al. Real-Time Magnetic Resonance Imaging Guidance Improves the Diagnostic Yield of Endomyocardial Biopsy. *JACC Basic to Transl Sci* 2016;**1**(5):376–383. doi:10.1016/j.jacbts.2016.05.007.

5. Pushparajah K, Chubb H, Razavi R. MR-guided Cardiac Interventions. *Top Magn Reson Imaging* 2018;**27**(3):115–128. doi:10.1097/RMR.0000000000000156.

6. Es R van, Broek HT van den, Naald M van der, Jong L de, et al. Validation of a novel stand-alone software tool for image guided cardiac catheter therapy. *Int J Cardiovasc Imaging* 2019;**0**(0):0. doi:10.1007/s10554-019-01541-9.

7. Salden OAE, Broek HT van den, Everdingen WM van, Mohamed Hoesein FAA, et al. Multimodality imaging for real-time image-guided left ventricular lead placement during cardiac resynchronization therapy implantations. *Int J Cardiovasc Imaging* 2019;**0**(0):0. doi:10.1007/s10554-019-01574-0.

8. Calkins H, Hindricks G, Cappato R, Kim YH, et al. 2017 HRS/EHRA/ECAS/APHRS/SOLAECE expert consensus statement on catheter and surgical ablation of atrial fibrillation: Executive summary. *Europace* 2018;**20**(1):157–208. doi:10.1093/europace/eux275.

9. Cronin EM, Bogun FM, Maury P, Peichl P, et al. 2019 HRS/EHRA/APHRS/LAHRS expert consensus statement on catheter ablation of ventricular arrhythmias. *Europace* 2019;1–147. doi:10.1093/europace/euz132.

10. Ben-Haim SA, Osadchy D, Schuster I, Gepstein L, et al. Nonfluoroscopic, in vivo navigation and mapping technology. *Nat Med* 1996;**2**(12):1393–1395. doi:10.1038/nm1296-1393.

11. Gyöngyösi M, Dib N. Diagnostic and prognostic value of 3D NOGA mapping in ischemic heart disease. *Nat Rev Cardiol* 2011;**8**(7):393–404. doi:10.1038/nrcardio.2011.64.

12. Wijnmaalen AP, Geest RJ Van Der, Huls Van Taxis CFB Van, Siebelink HMJ, et al. Head-to-head comparison of contrast-enhanced magnetic resonance imaging and electroanatomical voltage mapping to assess post-infarct scar characteristics in patients with ventricular tachycardias: Real-time image integration and reversed registration. *Eur Heart J* 2011;**32**(1):104–114. doi:10.1093/eurheartj/ehq345.

13. Codreanu A, Odille F, Aliot E, Marie PY, et al. Electroanatomic Characterization of Post-Infarct Scars. Comparison With 3-Dimensional Myocardial Scar Reconstruction Based on Magnetic Resonance Imaging. *J Am Coll Cardiol* 2008;**52**(10):839–842. doi:10.1016/j.jacc.2008.05.038.

14. Desjardins B, Crawford T, Good E, Oral H, et al. Infarct architecture and characteristics on delayed enhanced magnetic resonance imaging and electroanatomic mapping in patients with postinfarction ventricular arrhythmia. *Hear Rhythm* 2009;**6**(5):644–651. doi:10.1016/j.hrthm.2009.02.018.

15. Slochteren FJ van, Es R van, Gyöngyösi M, Spoel TIG van der, et al. Three dimensional fusion of electromechanical mapping and magnetic resonance imaging for real-time navigation of intramyocardial cell injections in a porcine model of chronic myocardial infarction. *Int J Cardiovasc Imaging* 2016;1–11. doi:10.1007/s10554-016-0852-x.

16. Ogawa R, Kido T, Nakamura M, Kido T, et al. Diagnostic capability of feature-tracking cardiovascular magnetic resonance to detect infarcted segments: a comparison with tagged magnetic resonance and wall thickening analysis. *Clin Radiol* 2017;**72**(10):828–834. doi:10.1016/j.crad.2017.05.010.

17. Liu B, Dardeer AM, Moody WE, Hayer MK, et al. Reference ranges for three-dimensional feature tracking cardiac magnetic resonance: comparison with two-dimensional methodology and relevance of age and gender. *Int J Cardiovasc Imaging* 2018;**34**(5):761–775. doi:10.1007/s10554-017-1277-x.

18. Koudstaal S, Jansen of Lorkeers SJ, Gho JMIH, Hout GPJ van, et al. Myocardial infarction and functional outcome assessment in pigs. *J Vis Exp* 2014;(86):1–10. doi:10.3791/51269.

19. Heiberg E, Sjögren J, Ugander M, Carlsson M, et al. Design and validation of Segment - freely available software for cardiovascular image analysis. *BMC Med Imaging* 2010;**10**:1–13. doi:10.1186/1471-2342-10-1.

20. Zwanenburg JJM. Timing of cardiac contraction in humans mapped by high-temporal-resolution MRI tagging: early onset and late peak of shortening in lateral wall. *AJP Hear Circ Physiol* 2004;**286**(5):H1872–H1880. doi:10.1152/ajpheart.01047.2003.

21. Besl PJ, McKay HD. A method for registration of 3-D shapes. *IEEE Trans Pattern Anal Mach Intell* 1992;**14**(2):239–256. doi:10.1109/34.121791.

22. Slochteren FJ van, Es R van, Koudstaal S, Spoel TIG van der, et al. Multimodality infarct identification for optimal image-guided intramyocardial cell injections. *Neth Heart J* 2014;493–500. doi:10.1007/s12471-014-0604-2.

23. Bouwmeester W, Moons KGM, Kappen TH, Klei WA Van, et al. Internal validation of risk models in clustered data: A comparison of bootstrap schemes. *Am J Epidemiol* 2013;**177**(11):1209–1217. doi:10.1093/aje/kws396.

24. Oirbeek R Van, Lesaffre E. Assessing the predictive ability of a multilevel binary regression model. *Comput Stat Data Anal* 2012;**56**(6):1966–1980. doi:10.1016/j.csda.2011.11.023.

25. Bouwmeester W, Twisk JW, Kappen TH, Klei WA Van, et al. Prediction models for clustered data: Comparison of a random intercept and standard regression model. *BMC Med Res Methodol* 2013;**13**(1):1. doi:10.1186/1471-2288-13-19.

26. Snijders TAB, Bosker RJ. Multilevel analysis : an introduction to basic and advanced multilevel modeling. 2012;(January):354.

27. Team RDC. R: A language and environment for statistical computing. [Vienna, Austria]: R Foundation for Statistical Computing; 2008.

28. Bates D, Mächler M, Bolker B, Walker S. Fitting Linear Mixed-Effects Models Using lme4. *J Stat Softw* 2015;**67**(1) doi:10.18637/jss.v067.i01.

29. Langenhove G Van, Hamburger JN, Diamantopoulos L, Smits PC, et al. Validation of the local shortening function as assessed by nonfluoroscopic electromechanical mapping: A comparison with computerized left ventricular angiography. *Int J Cardiol* 2001;**77**(1):33–41. doi:10.1016/S0167-5273(00)00385-5.

30. Gepstein L, Goldin a, Lessick J, Hayam G, et al. Electromechanical characterization of chronic myocardial infarction in the canine coronary occlusion model. *Circulation* 1998;**98**(19):2055–2064. doi:10.1161/01.CIR.98.19.2055.

31. Everdingen WM van, Zweerink A, Nijveldt R, Salden OAE, et al. Comparison of strain imaging techniques in CRT candidates: CMR tagging, CMR feature tracking and speckle tracking echocardiography. *Int J Cardiovasc Imaging* 2018;**34**(3):443–456. doi:10.1007/s10554-017-1253-5.

32. Vo HQ, Marwick TH, Negishi K. MRI-Derived Myocardial Strain Measures in Normal Subjects. *JACC Cardiovasc Imaging* 2018;**11**(2P1):196–205. doi:10.1016/j.jcmg.2016.12.025.

33. Buss SJ, Krautz B, Hofmann N, Sander Y, et al. Prediction of functional recovery by cardiac magnetic resonance feature tracking imaging in first time ST-elevation myocardial infarction. Comparison to infarct size and transmurality by late gadolinium enhancement. *Int J Cardiol* 2015;**183**:162–170. doi:10.1016/j.ijcard.2015.01.022.

34. Gho JMIH, Es R van, Slochteren FJ van, Jansen of Lorkeers SJ, et al. A systematic comparison of cardiovascular magnetic resonance and high resolution histological fibrosis quantification in a chronic porcine infarct model. *Int J Cardiovasc Imaging* 2017;**33**(11):1797–1807. doi:10.1007/s10554-017-1187-y.

35. Schuster A, Stahnke VC, Unterberg-Buchwald C, Kowallick JT, et al. Cardiovascular magnetic resonance feature-tracking assessment of myocardial mechanics: Intervendor agreement and considerations regarding reproducibility. *Clin Radiol* 2015;**70**(9):989–998. doi:10.1016/j.crad.2015.05.006.

36. Bourfiss M, Vigneault DM, Aliyari Ghasebeh M, Murray B, et al. Feature tracking CMR reveals abnormal strain in preclinical arrhythmogenic right ventricular dysplasia/ cardiomyopathy: a multisoftware feasibility and clinical implementation study. *J Cardiovasc Magn Reson* 2017;**19**(1):66. doi:10.1186/s12968-017-0380-4.

37. Liang JJ, Hebl VB, DeSimone C V., Madhavan M, et al. Electrogram guidance: a method to increase the precision and diagnostic yield of endomyocardial biopsy for suspected cardiac sarcoidosis and myocarditis. *JACC Heart Fail* 2014;**2**(5):466–473. doi:10.1016/j.jchf.2014.03.015.

38. Casella M, Pizzamiglio F, Russo A Dello, Carbucicchio C, et al. Feasibility of Combined Unipolar and Bipolar Voltage Maps to Improve Sensitivity of Endomyocardial Biopsy. *Circ Arrhythmia Electrophysiol* 2015;**8**(3):625–632. doi:10.1161/CIRCEP.114.002216.

39. Psaltis PJ, Zannettino ACW, Gronthos S, Worthley SG. Intramyocardial Navigation and Mapping for Stem Cell Delivery. *J Cardiovasc Transl Res* 2010;**3**(2):135–146. doi:10.1007/s12265-009-9138-1.

40. Sieniewicz BJ, Behar JM, Gould J, Claridge S, et al. Guidance for Optimal Site Selection of a Leadless Left Ventricular Endocardial Electrode Improves Acute Hemodynamic Response and Chronic Remodeling. *JACC Clin Electrophysiol* 2018;**4**(7):860–868. doi:10.1016/j.jacep.2018.03.011.

Supplementary data

MRI parameters

In eleven animals MRI acquisition was performed using a clinical 1.5T scanner (Ingenia TX, Philips Healthcare, Best, the Netherlands). BTFE acquisition parameters: Repetition time [TR]/echo time [ET] = 3.39 ms/1.69 ms. Flip angle = 60°, Pixel size = 1.25 x 1.25 mm, Field of view [FOV] = 320 x 320 mm, 256 x 256 matrix, 8 mm slice thickness, 30 phases/R-to-R interval. LGE acquisition parameters: [TR]/[ET] = 3.64 ms/1.19 ms. Flip angle = 25°, Pixel size = 1.25 x 1.25 mm, [FOV] = 296 x 296 mm, 256 x 256 matrix, 4 mm slice thickness.

In four animals MRI acquisition was performed using a clinical 3T scanner (Achieva TX, Philips Healthcare, Best, the Netherlands).[1] The BTFE acquisition parameters were as follows: Repetition time [TR]/echo time [ET] = 3.2 ms/1.6 ms. Flip angle = 45°, Pixel size = 2 x 2 mm, Field of view [FOV] = 320 x 320 mm, 256 x 256 matrix, 8 mm slice thickness, 30 phases/R-to-R interval.

Timing of onset algorithm

The algorithm automatically determines the timing of onset shortening, defined as the beginning of the downslope of the endocardial circumferential strain curve. In this study, a modified version of the algorithm for estimation of onset time of shortening described by Zwanenburg *et al* was used.[2] In this study instead of MR tagging, the curves were calculated using MR feature tracking on standard cardiac cine images triggered on the R-to-R interval. Thus omitting the necessity to correct for a strain offset caused by variations in tag distance nor to account for the dependency of the accuracy on the tagging contrast. The line fit model *L* was defined as described by Zwanenburg *et al*. Akinetic segments with a circumferential strain amplitude of >-7.5% were excluded from the analysis. The strain curves were interpolated using the *spline* function. The endpoint of the time interval was defined as the moment of peak strain rate. The line fit model, *L*, was fitted to the automatically selected data with a step size of 1 ms. The onset time of shortening T_{onset} was defined by the timing corresponding to the lowest residual error (sum of squares).

Performance of the prediction model

Performance of a model can be assessed using measures for discrimination and calibration. Discrimination gives an indication of how well the model can classify patients in those with and those without the outcome. The most commonly used measure for discrimination is the c-statistic, which for a binary problem is equivalent to the area under the receiver operating curve. A c-statistic of 0.5 indicates that the model performs as well as a coin flip, while a value of almost 1 indicates perfect discrimination. Calibration, on the other hand, gives an indication of the agreement between predicted and observed outcomes. This means that if the model predicts a 50% chance of the outcome, that for a sample of 100 data points the observed frequency of the outcome is 50. Calibration can be assessed with a calibration slope, which should be 1 for a perfect calibration. A calibration slope larger than 1 in the validation step is an indication of overfitting.[3,4]

For a mixed-effects model, the overall performance measures are not appropriate, as they do not take the clustering of the data into account. Therefore, the c-statistic is derived within each cluster or subject and then the average, weighted for the amount of data point within each cluster, is used.[5] The within-subject calibration slope is assessed by fitting a new mixed-effects logistic regression model, with only input the linear predictor from the original model and a random intercept and slope.[6]

Internal validation

The performance measures described above can be overly optimistic when determined in the sample where the model is based on. We can correct for this optimism by refitting the model repeatedly in new bootstrap samples and subsequently validate it in the original sample. The difference between c-statistic and calibration slope in the bootstrap and the original sample is called the optimism and will be subtracted from the values derived in the development set. In this paper, 500 bootstrap samples are used for this step.

For a mixed-effects model, bootstrap sampling can be done by sampling individual data points, whole clusters of data or a 2-step approach where both sampling methods are combined. If there are less than 20 clusters present, the regular bootstrap scheme with individual data points is most appropriate.[7] External validation in a new population remains necessary to verify the performance of the model in related populations.

References supplemental data

1. Es R van, Slochteren FJ van, Jansen of Lorkeers SJ, Blankena R, et al. Real-time correction of respiratory-induced cardiac motion during electroanatomical mapping procedures. *Med Biol Eng Comput* 2016;**54**(11):1741–1749. doi:10.1007/s11517-016-1455-3.

2. Zwanenburg JJM. Timing of cardiac contraction in humans mapped by high-temporal-resolution MRI tagging: early onset and late peak of shortening in lateral wall. *AJP Hear Circ Physiol* 2004;**286**(5):H1872–H1880. doi:10.1152/ajpheart.01047.2003.

3. Harrell FE, Lee KL, Mark DB. Tutorial in biostatistics multivariable prognostic models, evaluating assumptions and adequacy, and measuring and reducing errors. *Stat Med* 1996;**15**:361–387. doi:10.1002/(SICI)1097-0258(19960229)15:4<389::AID-SIM285>3.0.CO;2-J STATISTICS.

4. Steyerberg EW, Vickers AJ, Cook NR, Gerds T, et al. Assessing the performance of prediction models: A framework for traditional and novel measures. *Epidemiology* 2010;**21**(1):128–138. doi:10.1097/EDE.0b013e3181c30fb2.

5. Oirbeek R Van, Lesaffre E. Assessing the predictive ability of a multilevel binary regression model. *Comput Stat Data Anal* 2012;**56**(6):1966–1980. doi:10.1016/j.csda.2011.11.023.

6. Klaveren D Van, Steyerberg EW, Perel P, Vergouwe Y. Assessing discriminative ability of risk models in clustered data. *BMC Med Res Methodol* 2014;**14**(1):1–10. doi:10.1186/1471-2288-14-5.

7. Bouwmeester W, Moons KGM, Kappen TH, Klei WA Van, et al. Internal validation of risk models in clustered data: A comparison of bootstrap schemes. *Am J Epidemiol* 2013;**177**(11):1209–1217. doi:10.1093/aje/kws396.

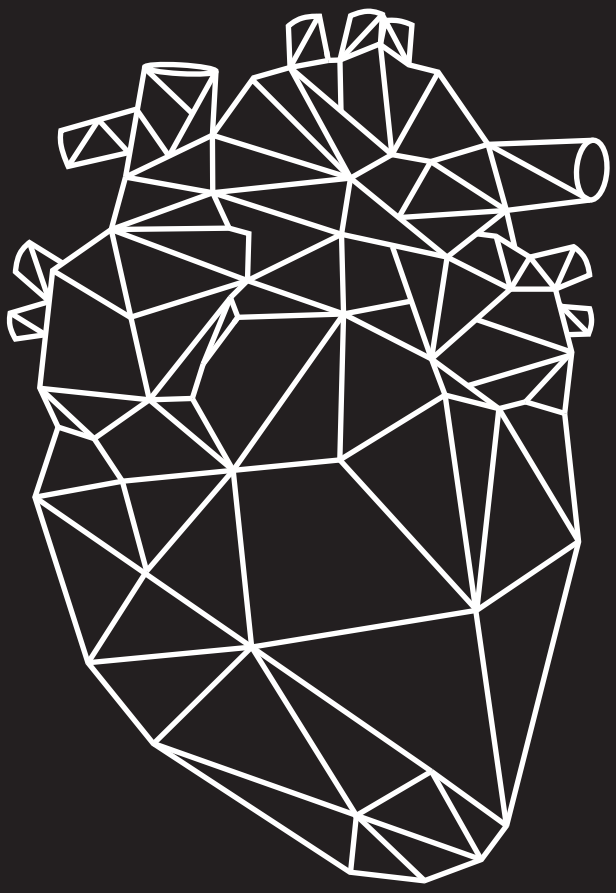

Chapter 7

General Discussion

Advancing medical devices for novel image-guided percutaneous cardiac interventions

In the preceding decade, the number of patients developing chronic heart failure (HF) has increased and will continue to increase in the coming years.[1] This is a significant economic and healthcare burden that drives the need for novel and optimized cardiovascular treatment strategies. Current treatment strategies focus on prevention of further left ventricle (LV) deterioration and/or improvement of LV function, symptom relief, and to prolong life. The complexity of cardiac interventions has increased due to technological development and the shift from complex surgical procedures to less invasive transcatheter-based procedures in combination with the rapid introduction of novel medical technology in clinical practice.

This thesis describes the development of a new 3D navigation technique for image-guided cardiac interventions. From bench to bedside we have developed the imaging technology, designed the testing methods, and performed the (pre-)clinical studies to assess its accuracy and clinical safety and feasibility. In this process, we can distinguish four sections: 1. development of a validation tool, 2. Pre-clinical assessment of the technique, 3. clinical validation of the technique, and 4. novel clinical insights from pre-clinical voltage mapping.

Development of a validation tool

Cardiac interventions targeted towards a specific lesion or substrate requires interventional imaging for accurate identification and visualization of the target as well as the interventional device. Assessment of the accuracy of new techniques for image-guided therapy is important and the assessment method should depend on the specific clinical use. The numerous clinical applications contribute to the use of various validation methods as well as different end-point definitions as seen across validation studies.[2–4] The use of distinct validation methods prevents the comparison of similar techniques.
We hypothesized that a standardized validation protocol can be of help to accurately and uniformly assess the targeting accuracy of treatment techniques and efficiently contribute to the pre-clinical phase of medical device development.

Important prerequisites of the validation method are the accuracy of the method and that the method ideally is representative for multiple applications. For the clinical application of injections, the targeting of a local transition of tissue characteristics is the most applicable and also the most usable method. Other cardiac applications either specifically target tissue lesions or aim to avoid these tissue characteristics such as endomyocardial biopsies (EMB)[5] and LV lead delivery in cardiac resynchronization therapy (CRT)[6], respectively. In **Chapter 3**, we presented a novel, standardized, and reproducible whole-heart myocardial tissue processing method to perform validation of the injection targeting accuracy of a 3D navigation tool in both 2D and 3D. To assess the targeting accuracy we measured the linear distance from the injection location to the infarct border zone. Measuring the distance from the injection location to the target location is the most direct method to obtain injection accuracy. Injection of fluorescent microbeads enabled assessment of targeting accuracy at high-resolution fluorescent imaging compared to the lower resolution images from other imaging modalities such as MRI.

In this study, only the assessment of the targeting accuracy of intramyocardial injections was performed. Even though other applications require different catheters, pacing leads, or bioptomes, these are likely subjected to similar flexibility and bending stiffness and require similar catheter manipulations. Therefore, we believe a similar targeting accuracy can be expected in other applications like LV lead delivery and EMB. Important for the development of novel navigation techniques is the clinical accuracy.[7] There is no generally accepted threshold to define clinical accuracy. The clinical accuracy is also dependent on the clinical application. For example, consider EMB targets consist of 4 border zones. To target all 4 borders with an uncertainty of 0.5 mm in all directions, a target area of 1 cm^2 is needed to, in theory, always accurately target. The prerequisite is that the target is the same size in all directions. In addition, it is of course necessary to take an (un-)certainty margin. The question what the minimum lesion size must be to be able to navigate towards and correctly target with certainty is an interesting research topic for future research.

Instead of intramyocardial injections, ablation points could be used to validate the targeting accuracy of new navigation techniques. The latter approach requires, however, an additional procedure for the lesions to be placed which are then used as target sites in a consecutive procedure. Thereby adding the opportunity to validate the targeting accuracy twice. The procedure to create 'target lesions' is subject to the success rate of the ablation and is, therefore, not a guarantee to create a pre-determined number of ablation points per subject. Moreover, in the histological assessment of measuring the targeting accuracy distinguishing the 'target lesion' from the 'targeted lesion' is more difficult since similar lesions are created.

Pre-clinical assessment of the technique

The validation tool was subsequently used in **Chapter 4** in which we investigated the accuracy of a new 3D navigation technique. We compared the targeting accuracy of CARTBox2 to the NOGA® XP electroanatomical mapping (EMM) system and demonstrated non-inferiority to accurately facilitate intramyocardial injections into the infarct border zone based on gold standard MR-imaging and live XRF. Intramyocardial injections have been used in (pre-)clinical research focussing on cardiac regeneration, and the use of bone marrow-derived stem/progenitor cells has, in this respect, been of limited success.[8] A recent study found no evidence for the existence of a passive cardiac stem cell population.[9] Thereby it questions the paradigm of cardiac regeneration. Research has yet to show the clinical relevance of other cardiac regenerative therapeutics such as pluripotent stem cells, adipose-derived stem cells, or secretome-rich injectables.[10–14] In anticipation of the effect and clinical relevance of regenerative therapy, the 3D navigation technique for accurate local therapies inside the heart stands on itself and can be adapted for other therapies like LV lead placement or biopsies. The validation method, therefore, must also reflect the necessary accuracy measures for these other therapies.

The developed technology requires registration of the CARTBox treatment dataset and 3D rotational angiography (3DRA). The registration was performed by a 3D/3D registration method available in the multimodality imaging software package of the X-ray system. The workflow involves several steps that are prone to introducing registration errors including the semi-automatic registration process. During testing and research use we did not experience a structural shift after registration which suggests adequate registration and that is reflected by the results. Standardized imaging and image registration protocols can minimize the errors and integration of machine learning approaches have the potential to further automate and standardize the registration process.[15]

Considering CARTBox is vendor-independent and uses standard diagnostic and interventional imaging, the technique is smoothly integrated in clinical practice. Novel techniques, e.g. MediGuide (Abbott) and CARTO-UNIVU (Biosense Webster), use pre-recorded XRF movies from two angles to facilitate XRF guidance.[16,17] The single heartbeat fluoroscopic movies are continuously repeated which limits the radiation exposure to two fluoroscopic acquisitions and thus overall radiation burden. Live tracking of the catheter is performed by 3D magnetic and/or electric tracking and a rendered 3D catheter is superimposed onto the XRF movies. Such radiation reducing imaging techniques can be easily combined with the CARTBox navigation technique.

Transition from the pre-clinical to the clinical phase

After pre-clinical evaluation of CARTBox by assessing the safety, feasibility, and targeting accuracy of the navigation technique compared to the clinical standard technique. After the first two cycles of the concept, prototyping, and pre-clinical phase (**Figure 1**), the software had become a stand-alone software toolbox fully integrating the MR-imaging post-processing workflow and had received CE-marking. In the medical device development cycle, aforementioned steps, including verification and validation of the design, testing, and redesign of the medical device, are repeated until the medical device is fully tested and deemed fit for use in the clinical phase (**Figure 1**). Instead of continuation of the prototyping and pre-clinical phase, the design was frozen for use in the clinical phase.

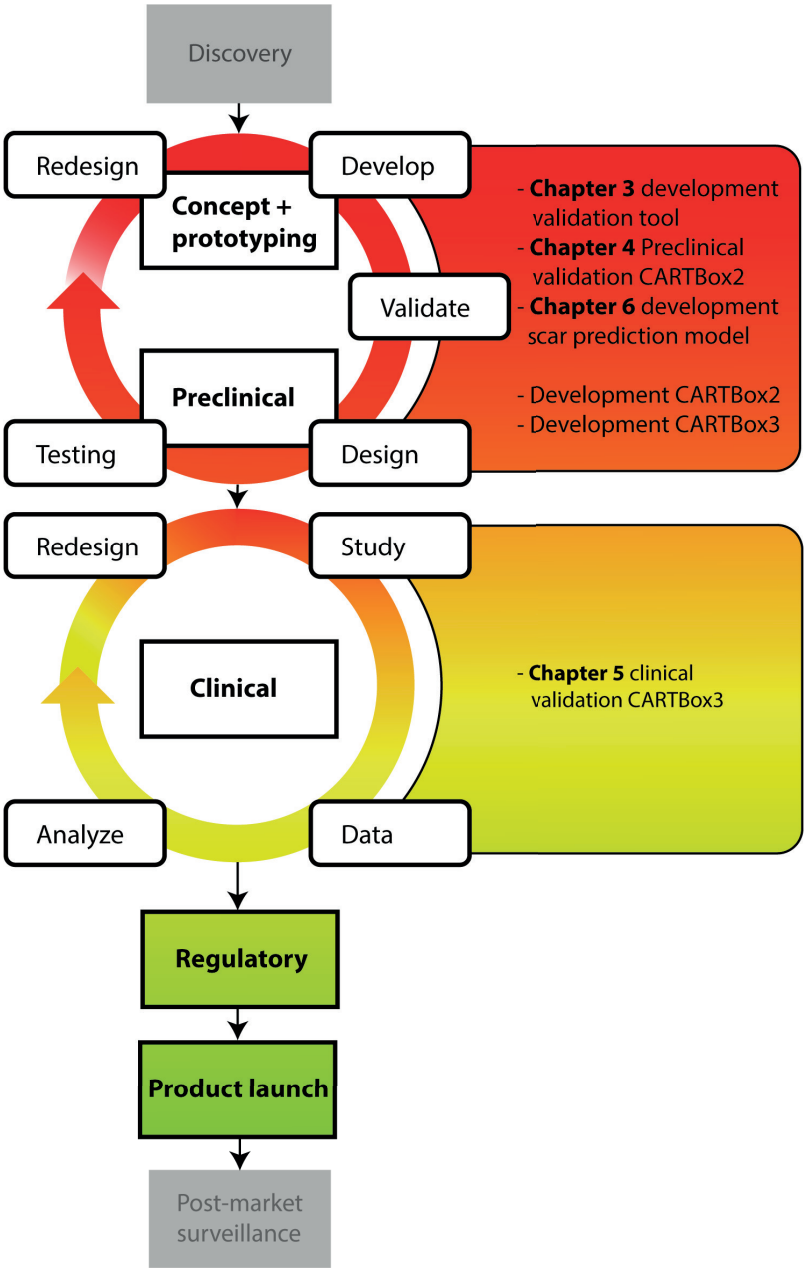

Figure 1: Medical device development cycle. The first two phases of the development cycle consist of iterative steps aimed at improving the medical device and gathering (preliminary) data regarding the device's safety and efficacy. In the panels on the right-side, contributions to the first phase included the development of the validation tool described in **chapter 3**, the pre-clinical validation of the new 3D navigation technique described in **chapter 4**, and development of a scar prediction model described in **chapter 6**. Contribution to the second phase includes the clinical validation of the navigation technique described in **chapter 5**.

The transition from the pre-clinical to the clinical phase and the reason to use the technology for image-guided CRT device implantation can be explained by several reasons. First, the pre-clinical feasibility study had shown that the 3D navigation technique was feasible. Second, the study had also demonstrated that the targeting accuracy was non-inferior compared to the clinical standard technique. Since the safety evaluation of a CE-marked medical device in a pre-clinical setting is of limited value, the next step was further investigation of the safety and feasibility in an observational clinical study. Third, although a new version of the medical device was developed, CARTBox3, the same algorithms and principles of operation were used and development according to the same quality management system. Fourth, since CRT device implantation already makes use of gold standard diagnostic and interventional imaging, MRI and XRF respectively, the technique enabled us to integrate multiple modalities in clinical practice.

Clinical validation of the technique

CRT is a standard therapy for HF and as such part of the European Society of Cardiology (ESC) guidelines on cardiac pacing and resynchronization therapy.[18] Although CRT has shown a beneficial effect on patients with HF, severe left ventricular (LV) dysfunction, and prolonged QRS duration, the improved clinical outcome is suboptimal in 30-45% of patients.[19] Besides improved patient selection and optimized device programming, targeted LV lead delivery has been identified as an important optimization strategy. Several studies have shown that the response rate can be improved by targeting optimal pacing sites for LV stimulation.[20–22] However, these studies did not use image fusion to facilitate image-guided LV lead placement.

Clinical evaluation of the 3D navigation technique, in terms of safety and feasibility of per-procedural visualization of optimal pacing sites and image-guided LV lead placement, was demonstrated in **Chapter 5**. Time-to-peak endocardial circumferential strain obtained from short axis cine MRI feature tracking (MRI-FT) was used for the identification of latest contracting segments. Thereby noise in the strain curves was a limiting factor. A possible explanation could be that the circumferential movement of the myocardial wall is more difficult to track using MRI-FT. Radial strain is possibly more suitable for an FT based analysis

since the tracking of features is then done orthogonal to the endocardial wall, where the contrast is highest. Previous research, however, demonstrated reasonable agreement of MRI-FT with MRI-tagging and LV circumferential endocardial strain has shown to be the most reproducible strain parameter.[23–25] The same research also showed that assessment of the regional strain parameters by MRI-FT may not be as accurate as tagging.[23] In our study, strain analysis was performed in 48 segments per slice and combined to 12 segments per slice during post-processing. The high number of segments during post-processing allowed increased accuracy compared to the American Heart Association (AHA) 17-segment model used in clinical practice. The increased accuracy allows more accurate placement of the LV lead in the zone of latest contraction. The accuracy of MRI-FT highly depends on the accuracy of the segmentation of the endo- and epicardial borders. From those borders features are defined and tracked over time, based on the intensity gradient of the tissue-cavity interface, tissue inhomogeneities, and the spatial coherence. Therefore, image quality and quality of the myocardial segmentation is likely affecting the strain analysis. In addition, large variability has been observed between different FT software packages for CMR strain analysis.[25,26] Standardization of the FT technique is necessary to overcome the variability and produce a more robust MRI-derived strain analysis. Integration of 3D analysis in MRI-FT shows to be less sensitive to through-plane motion and improves reproducibility by superior tracking.[27] In a follow-up study, the use of 3D MRI-FT should be investigated.

Anatomical variations of the coronary sinus can impose difficulties for cannulation and thereby procedure duration.[28] Multiple research applications have shown that 3D reconstructed LV venous anatomy can be used to determine the angles of the X-ray system to optimize cannulation of the coronary sinus.[29–32] Visualization of the complete LV venous anatomy during the implantation may also improve selection of the coronary vein leading to the target site and is suggested to be an important factor in LV lead delivery to a target segment.[33] In the ADVISE study, venous angiography was performed during the intervention because it is considered the gold standard to identify the small venous tributaries unable to be visualized by cardiac CT. Therefore, only the coronary sinus ostium of the coronary vein was derived from the CT scans. New developments such as the snare technique and microcatheters underline the importance of visualizing the small venous anatomy.[34,35]

Developments of the image quality of the cardiac CT technique and contrast protocols may enable complete LV venous anatomy in the future.[36,37] Although, it remains important to consider the relative benefit taken into account the higher radiation burden from cardiac CT compared to venous angiography.

Novel clinical insights from pre-clinical voltage mapping

Many cardiac catheter-based interventions require accurate discrimination between healthy and infarcted myocardium. In our studies, we focused on the gold-standard for scar identification, late gadolinium-enhanced MRI (LGE-MRI), and fused that with XRF. However, the clinical standard to identify myocardial scar during electrophysiology procedures is EMM or EAM (electroanatomical mapping). Using these mapping techniques, electrical and/or mechanical parameters are measured directly at the myocardium in a pointwise fashion, explained in more detail in **Chapter 4**. Previous research has shown that the electrical parameters, unipolar and bipolar voltage, are adequate in distinguishing healthy from infarcted myocardium but lack the potential to discriminate between different infarct transmuralities.[38] We hypothesized that a combination of EMM or EAM parameters by means of a prediction model could accurately discriminate healthy myocardium from scarred myocardium.

Data analysis of previously acquired data can also be used to gain new insights and to innovate with that. Accordingly, in **Chapter 6**, we developed a novel method to predict the presence of LGE-scar by a statistical prediction model using multiple EMM-parameters. To compare the results, we used high-density electromechanical maps from a porcine infarction model and registered the maps in 3D to MRI-derived endocardial surface maps with a projection of the infarction transmurality. The comparison of FT-derived strain parameters to EMM-derived parameters of local mechanical deformation revealed only weak correlations. A possible explanation could be noise in both the FT data and in the linear local shortening (LLS) data. Previous research found no correlation of LLS and local wall thickness data and discussed this was most likely caused by erroneous LLS values as a result of low-density EMM maps.[38] Given the high-density of the EMM maps, the latter is not likely the case in our study.

In the previous section, several factors important for MRI-FT accuracy have been mentioned that could explain the noise in the strain signals. Important for this study was accurate discrimination between healthy and infarcted myocardium. MRI-FT has difficulties with poorly deforming sectors, such as akinetic sectors affected by myocardial infarction, due to poor tracking of the features. To prevent incorrect deformation assessment in these sectors, strain signals below a pre-determined threshold were excluded for further analysis but included in the prediction model. In a future study, it is interesting to investigate the use of radial strain because in the radial direction the blood-cavity contrast may provide improved feature tracking compared to endocardial circumferential strain.

In this study, we demonstrated that our model has a strong predictive ability for the presence of myocardial scar. To perform the internal validation, considering the small number of subjects, we used a bootstrap sample of our dataset. Even though bootstrapping is a statistically correct method for internal validation in a small dataset, the current data originates from a pre-clinical large animal model for chronic myocardial infarction. A clinical dataset is necessary for the clinical validation of the scar prediction model.

Future perspectives

In **Chapter 2**, we briefly acknowledged that interests in performing image-guided targeted catheterization procedures extend further than structural and congenital heart diseases. These cardiac fields rely mostly on planning and anatomical visualization whereas substrate targeting (e.g. endomyocardial biopsies, regenerative therapy) and/or modification (e.g. electrophysiology ablations, CRT device implantations) require soft-tissue visualization, target selection, and interventional device imaging.

Other cardiac interventions

Endomyocardial biopsy (EMB) is another example of cardiac intervention involving substrate targeting, EMB is the gold standard technique to diagnose multiple cardiac diseases ranging from cardiac sarcoidosis, amyloidosis, to unexplained LV hypertrophy.

Currently, EMB is performed under live XRF guidance without the ability for soft-tissue visualization. Cardiologists rely on their experience and judgement while obtaining tissue specimens, which leads to a rather low sensitivity of EMB.[39] For example, in the diagnosis of isolated cardiac sarcoidosis at least 60-70% of the initial EMB procedures are negative or lab results are nonspecific.[40] Besides EMB, non-invasive diagnostic imaging techniques (MRI /PET-CT) are often used to diagnose cardiac sarcoidosis. These imaging modalities, however, have demonstrated varying sensitivity and specificity to detect cardiac sarcoidosis.[41,42] For this reason, EMB remains the gold standard for diagnosis of aforementioned diseases.[43,44] Hybrid fusion technology enables the use of the gold standard LGE-MRI as well as PET-CT to contribute to a standardized method for target selection and targeted image-guided EMB procedures. Thereby increasing the yield and consequently improving the therapy.

The concept of image-guided EMB is not new and has already been investigated.[45–50] A recent case report showed the clinical use of MRI-XRF fusion to guide the bioptome towards an intra-cardiac ventricular mass.[47] Several other studies proposed the use of EMM guidance for EMB procedures.[45,46,50] In one study, biopsy sites of eleven patients with suspected cardiac sarcoidosis were correlated with bipolar amplitudes of less than 5mV, resulting in 100% specificity and positive predictive value for identifying abnormal myocardial tissue.[46] Another study combined the Advanced Catheter Localization technology in the CARTO electroanatomical mapping system with in-house modified bioptomes.[50] Via local changes in the electromagnetic field, the bioptome was visualized on CARTO. Both EMM approaches, however, increase procedure time and patient burden since it is not part of the standard clinical workflow for patients undergoing an EMB procedure. Hence hybrid imaging can play a role in image-guided EMB procedures, integrating information on cardiac function, scar/fibrosis burden, and presence and extent of active inflammation. Furthermore, hybrid imaging has the advantage to visualize the target in 3D and thereby adds the local wall thickness as a parameter to select the biopsy target. Thereby preventing perforation due to biopsies in thin myocardium. The application of targeted image-guided biopsies extends to other infiltrative diseases as well.[51]

Interventional MRI

Cardiac MRI is recognized as an important imaging modality in the diagnosis of many cardiac diseases. MRI provides a comprehensive evaluation of cardiac anatomy, function, blood flow, and tissue characterisation. For this reason, current hybrid fusion imaging applications mainly focus on the incorporation of MRI to provide advanced treatment planning and 3D image-guidance based on soft-tissue visualization. Hybrid fusion imaging applications require multiple imaging modalities to provide the additional imaging information. Therefore, interventional MRI (iMRI) is a logical next step to guide complex cardiac interventions. iMRI provides simultaneous functional, anatomical, tissue characterization, and flow information in a single, ionizing radiation-free, intervention. Moreover, in contrast to hybrid imaging iMRI overcomes the possible registration error origination from the fusion of multiple imaging modalities.

There are numerous studies that have investigated the concept of cardiac interventions by iMRI guidance. Several pre-clinical studies have demonstrated that a ~50% higher diagnostic EMB yield can be achieved by using iMRI compared to conventional fluoroscopic guidance, however, at the cost of increased procedural duration.[48,49] In our department, the feasibility of real-time MRI-guided intramyocardial injections with combined active and passive catheter tracking was reported for the first time.[52] For electrophysiology procedures, the current workflow requires an extensive and complex ablation procedure that involves cardiac surface mapping, ablation, and assessment of the effect of ablation lesions. iMRI enables a single imaging modality workflow which most importantly enables direct visualization of the ablation lesions as well as the lesion transmurality and success of the procedure. Several studies report the safety and feasibility of electrophysiology ablations in interventional MRI in patients.[53,54]

Although iMRI may become an important interventional imaging modality several critical challenges can be identified that need to be resolved. First, a large proportion of chronic HF patients has an implantable cardioversion defibrillation device that is not suitable for the high magnetic field of the MRI. Historically, cardiac implantable devices were regarded as near absolute contraindication for MRI due to major concerns of MRI scanner and cardiac device interaction causing malfunction of or permanent damage to the device, or damage

to the heart by the heating of the device leads. Current ESC guidelines on cardiac pacing and CRT have adopted strict conditions for device programming when MRI is required.[18] Moreover, technological advances have resulted in MRI-conditional devices.[55] The devices still cause scattering artefacts and are prone to heating of tissue due to RF energy absorption. Second, iMRI requires MR compatible and trackable catheters, patient hemodynamic monitoring devices, and other (interventional) tools (e.g. needles, wires, bioptomes). Third, iMRI requires a dedicated MRI system or occupies diagnostic scanning time, which is costly and thus increases procedural costs and an interventional MR setup is not widely available. Fourth, revision of the existing workflow is necessary to transition from current XRF procedures toward an iMRI suite. The revision workflow includes expansion of the interventional team with an MR technologist as well as training of the staff. Fifth, the current ergonomics of the iMRI is less convenient for the cardiologist. The cardiologist is in a bent position for a long time period during the intervention, which is partly because of the small size of the MRI bore and the position of the patient inside the MRI.

For interventional MRI to become successful in the treatment of chronic HF patients, procedural and clinical outcomes should demonstrate a clear advantage over existing techniques.[56] Compared to interventional MRI, XRF-guided interventions are well established, therefore, hospitals should focus on interventions that have a significant advantage by using MR-guidance.[56,57] Research departments, hospitals, and the industry need to work together to provide in the current lack of clinical availability of (interventional) tools which is limiting the clinical adoption.[57] More research and development is necessary before interventional MRI can become the clinical practice in complex percutaneous cardiovascular interventions.

Clinical translation of medical technology

Healthcare is rapidly evolving due to the development of medical technology, the transition of complex surgical procedures to minimal invasive percutaneous procedures, and the introduction of that medical technology in clinical practice. Proper medical technical knowledge of the existing technology, as well as innovations, are necessary to safely use the technology to its full potential. This requires multidisciplinary experts with a solid scientific, medical, and engineering background. Most medical technological innovations arise from

medical technical problems in clinical practice. Biomedical engineers are trained to translate these problems towards engineering solutions, however, are still on the technical side of the medical technology introduction in clinical practice. Physicians, on the other hand, are trained to use the current technology but often lack in-depth technical knowledge. This gap hampers full use of the current medical technology as well as the translation of medical technical problems towards innovative solutions. To bridge the gap, technical physicians could be of great importance to the medical team.

Since 2003, the University of Twente educates technical physicians who are trained healthcare professionals with specific expertise in both the medical and technical domains. Whereas biomedical engineers are more on the design and development side of medical technology, technical physicians are trained to exhibit a unique technical-medical perspective and the ability to apply existing technology in innovative ways. This includes developing innovative diagnostic and treatment solutions for individual patients. For a quick adaptation of novel medical technology, working in multidisciplinary teams consisting of physicians, engineers, biologists, and mixed specialists is mandatory.

Final remarks

In this thesis, we described the development of novel technological approaches for optimization of percutaneous cardiovascular interventions, see **Figure 1**. The technologies were aimed to improve treatment planning, visualization, and guidance of complex cardiac interventions. The development and design phase consisted of iterative validation, software testing, and redesign of the medical device. Evaluation of the safety and feasibility of the technologies was performed in both the pre-clinical and clinical setting. During the whole development, quality assurance assessment was performed to receive regulatory approval. The next step in the development is the validation of the techniques to bring about the desired changes in the clinical effect size. The development steps shown in this thesis, from bench to bedside, accentuate how a medical technology specialist can be of importance for the clinical translation of medical technology. Hybrid fusion imaging technology is an important technique in the growing need for optimizations of complex cardiovascular interventions of heart failure patients.

References

1. Roger VL. Epidemiology of Heart Failure. *Circ Res* 2013;**113**(6):646–659. doi:10.1161/CIRCRESAHA.113.300268.

2. Silva R de, Gutierrez LF, Raval AN, McVeigh ER, et al. X-Ray Fused With Magnetic Resonance Imaging (XFM) to Target Endomyocardial Injections: Validation in a Swine Model of Myocardial Infarction. *Circulation* 2006;**114**(22):2342–2350. doi:10.1161/CIRCULATIONAHA.105.598524.

3. Tomkowiak MT, Klein AJ, Vigen KK, Hacker T a, et al. Targeted transendocardial therapeutic delivery guided by MRI-x-ray image fusion. *Catheter Cardiovasc Interv* 2011;**78**(3):468–478. doi:10.1002/ccd.22901.

4. Dauwe DF, Nuyens D, Buck S De, Claus P, et al. Three-dimensional rotational angiography fused with multimodal imaging modalities for targeted endomyocardial injections in the ischaemic heart. *Eur Heart J Cardiovasc Imaging* 2014; doi:10.1093/ehjci/jeu019.

5. Veinot JP. Endomyocardial biopsy-when and how? *Cardiovasc Pathol* 2011;**20**(5):291–296. doi:10.1016/j.carpath.2010.08.005.

6. Delgado V, Bommel RJ van, Bertini M, Borleffs CJW, et al. Relative Merits of Left Ventricular Dyssynchrony, Left Ventricular Lead Position, and Myocardial Scar to Predict Long-Term Survival of Ischemic Heart Failure Patients Undergoing Cardiac Resynchronization Therapy. *Circulation* 2011;**123**(1):70–78. doi:10.1161/CIRCULATIONAHA.110.945345.

7. Linte CA, Lang P, Rettmann ME, Cho DS, et al. Accuracy considerations in image-guided cardiac interventions: experience and lessons learned. *Int J Comput Assist Radiol Surg* 2012;**7**(1):13–25. doi:10.1007/s11548-011-0621-1.

8. Fisher SA, Doree C, Mathur A, Taggart DP, Martin-Rendon E. Stem cell therapy for chronic ischaemic heart disease and congestive heart failure. Martin-Rendon E, ed. *Cochrane Database Syst Rev* 2016;(12):10–13. doi:10.1002/14651858.CD007888.pub3.

9. Kretzschmar K, Post Y, Bannier-Hélaouët M, Mattiotti A, et al. Profiling proliferative cells and their progeny in damaged murine hearts. *Proc Natl Acad Sci* 2018;**115**(52):E12245–E12254. doi:10.1073/pnas.1805829115.

10. Duran A, Reidell O, Stachelscheid H, Klose K, et al. Regenerative Medicine/Cardiac Cell Therapy: Pluripotent Stem Cells. *Thorac Cardiovasc Surg* 2018;**66**(01):053–062. doi:10.1055/s-0037-1608761.

11. Stastna M, Eyk JE Van. Investigating the Secretome. *Circ Cardiovasc Genet* 2012;**5**(1):1–19. doi:10.1161/CIRCGENETICS.111.960187.

12. Waters R, Alam P, Pacelli S, Chakravarti AR, et al. Stem cell-inspired secretome-rich injectable hydrogel to repair injured cardiac tissue. *Acta Biomater* 2018;**69**(5):95–106. doi:10.1016/j.actbio.2017.12.025.

13. Paitazoglou C, Bergmann MW, Vrtovec B, Chamuleau SAJ, et al. Rationale and design of the European multicentre study on Stem Cell therapy in IschEmic Non-treatable Cardiac diseasE (SCIENCE). *Eur J Heart Fail* 2019;1–10. doi:10.1002/ejhf.1412.

14. Bruun K, Schermer E, Sivendra A, Valaik E, et al. Therapeutic applications of adipose-derived stem cells in cardiovascular disease. *Am J Stem Cells* 2018;**7**(4):94–103.

15. Toth D, Miao S, Kurzendorfer T, Rinaldi CA, et al. 3D/2D model-to-image registration by imitation learning for cardiac procedures. *Int J Comput Assist Radiol Surg* 2018;**13**(8):1141–1149. doi:10.1007/s11548-018-1774-y.

16. Pillarisetti J, Kanmanthareddy A, Reddy YM, Lakkireddy D. MediGuide—impact on catheter ablation techniques and workflow. *J Interv Card Electrophysiol* 2014;**40**(3):221–227. doi:10.1007/s10840-014-9909-8.

17. Christoph M, Wunderlich C, Moebius S, Forkmann M, et al. Fluoroscopy integrated 3D mapping significantly reduces radiation exposure during ablation for a wide spectrum of cardiac arrhythmias. *Europace* 2015;**17**(6):928–937. doi:10.1093/europace/euu334.

18. Brignole M, Auricchio A, Baron-Esquivias G, Bordachar P, et al. 2013 ESC Guidelines on cardiac pacing and cardiac resynchronization therapy. *Eur Heart J* 2013;**34**(29):2281–2329. doi:10.1093/eurheartj/eht150.

19. Daubert J-C, Saxon L, Adamson PB, Auricchio A, et al. 2012 EHRA/HRS expert consensus statement on cardiac resynchronization therapy in heart failure: implant and follow-up recommendations and management. *Hear Rhythm* 2012;**9**(9):1524–1576. doi:10.1016/j.hrthm.2012.07.025.

20. Saba S, Marek J, Schwartzman D, Jain S, et al. Echocardiography-Guided Left Ventricular Lead Placement for Cardiac Resynchronization Therapy: Results of the Speckle Tracking Assisted Resynchronization Therapy for Electrode Region Trial. *Circ Hear Fail* 2013;**6**(3):427–434. doi:10.1161/CIRCHEARTFAILURE.112.000078.

21. Khan FZ, Virdee MS, Palmer CR, Pugh PJ, et al. Targeted Left Ventricular Lead Placement to Guide Cardiac Resynchronization Therapy. *J Am Coll Cardiol* 2012;**59**(17):1509–1518. doi:10.1016/j.jacc.2011.12.030.

22. Leyva F. Cardiac resynchronization therapy guided by cardiovascular magnetic resonance. *J Cardiovasc Magn Reson* 2010;**12**(1):64. doi:10.1186/1532-429X-12-64.

23. Moody WE, Taylor RJ, Edwards NC, Chue CD, et al. Comparison of magnetic resonance feature tracking for systolic and diastolic strain and strain rate calculation with spatial modulation of magnetization imaging analysis. *J Magn Reson Imaging* 2015;**41**(4):1000–1012. doi:10.1002/jmri.24623.

24. Morton G, Schuster A, Jogiya R, Kutty S, et al. Inter-study reproducibility of cardiovascular magnetic resonance myocardial feature tracking. *J Cardiovasc Magn Reson* 2012;**14**(1):1. doi:10.1186/1532-429X-14-43.

25. Everdingen WM van, Zweerink A, Nijveldt R, Salden OAE, et al. Comparison of strain imaging techniques in CRT candidates: CMR tagging, CMR feature tracking and speckle tracking echocardiography. *Int J Cardiovasc Imaging* 2018;**34**(3):443–456. doi:10.1007/s10554-017-1253-5.

26. Cao JJ, Ngai N, Duncanson L, Cheng J, et al. A comparison of both DENSE and feature tracking techniques with tagging for the cardiovascular magnetic resonance assessment of myocardial strain. *J Cardiovasc Magn Reson* 2018;**20**:1–9. doi:10.1186/s12968-018-0448-9.

27. Liu B, Dardeer AM, Moody WE, Hayer MK, et al. Reference ranges for three-dimensional feature tracking cardiac magnetic resonance: comparison with two-dimensional methodology and relevance of age and gender. *Int J Cardiovasc Imaging* 2018;**34**(5):761–775. doi:10.1007/s10554-017-1277-x.

28. Hołda MK, Klimek-Piotrowska W, Koziej M, Mazur M. Anatomical variations of the coronary sinus valve (Thebesian valve): Implications for electrocardiological procedures. *Europace* 2015;**17**(6):921–927. doi:10.1093/europace/euu397.

29. Knackstedt C, Mühlenbruch G, Mischke K, Bruners P, et al. Imaging of the coronary venous system: Validation of three-dimensional rotational venous angiography against dual-source computed tomography. *Cardiovasc Intervent Radiol* 2008;**31**(6):1150–1158. doi:10.1007/s00270-008-9352-2.

30. Gutleben K-J, Nölker G, Ritscher G, Rittger H, et al. Three-dimensional coronary sinus reconstruction-guided left ventricular lead implantation based on intraprocedural rotational angiography: a novel imaging modality in cardiac resynchronization device implantation. *Europace* 2011;**13**(5):675–682. doi:10.1093/europace/eur004.

31. Alikhani Z, Li J, Merchan JA, Nijhof N, et al. Coronary sinus anatomy by computerized tomography, overlaid on live fluoroscopy can be successfully used to guide left ventricular lead implantation: A feasibility study. *J Interv Card Electrophysiol* 2013;**36**(3):217–222. doi:10.1007/s10840-012-9736-8.

32. Zhou W, Hou X, Piccinelli M, Tang X, et al. 3D Fusion of LV Venous Anatomy on Fluoroscopy Venograms With Epicardial Surface on SPECT Myocardial Perfusion Images for Guiding CRT LV Lead Placement. *JACC Cardiovasc Imaging* 2014;**7**(12):1239–1248. doi:10.1016/j.jcmg.2014.09.002.

33. Nguyên UC, Cluitmans MJM, Strik M, Luermans JG, et al. Integration of cardiac magnetic resonance imaging, electrocardiographic imaging, and coronary venous computed tomography angiography for guidance of left ventricular lead positioning. *EP Eur* 2019;**21**(4):626–635. doi:10.1093/europace/euy292.

34. WORLEY SJ, GOHN DC, PULLIAM RW. Goose Neck Snare for LV Lead Placement in Difficult Venous Anatomy. *Pacing Clin Electrophysiol* 2009;**32**(12):1577–1581. doi:10.1111/j.1540-8159.2009.02573.x.

35. Karalis I, Andreou C, Montero Cabezas JM, Schalij MJ. Microcatheters: A valuable tool in the presence of a challenging coronary anatomy in the setting of acute coronary interventions. Case report and mini review. *Cardiovasc Revascularization Med* 2017;**18**(6):48–51. doi:10.1016/j.carrev.2017.02.008.

36. Sun C, Pan Y, Wang H, Li J, et al. Assessment of the coronary venous system using 256-slice computed tomography. *PLoS One* 2014;**9**(8):1–7. doi:10.1371/journal.pone.0104246.

37. Ghekiere O, Salgado R, Buls N, Leiner T, et al. Image quality in coronary CT angiography: challenges and technical solutions. *Br J Radiol* 2017;**90**(1072):20160567. doi:10.1259/bjr.20160567.

38. Slochteren FJ, Es R, Gyöngyösi M, Spoel TIG, et al. Three dimensional fusion of electromechanical mapping and magnetic resonance imaging for real-time navigation of intramyocardial cell injections in a porcine model of chronic myocardial infarction. *Int J Cardiovasc Imaging* 2016;1–11. doi:10.1007/s10554-016-0852-x.

39. Frustaci A, Russo MA, Chimenti C. Diagnostic contribution of left ventricular endomyocardial biopsy in patients with clinical phenotype of hypertrophic cardiomyopathy. *Hum Pathol* 2013;**44**(1):133–141. doi:10.1016/j.humpath.2012.04.023.

40. Kandolin R, Lehtonen J, Graner M, Schildt J, et al. Diagnosing isolated cardiac sarcoidosis. *J Intern Med* 2011;**270**(5):461–468. doi:10.1111/j.1365-2796.2011.02396.x.

41. Zhang J, Li Y, Xu Q, Xu B, Wang H. Cardiac Magnetic Resonance Imaging for Diagnosis of Cardiac Sarcoidosis: A Meta-Analysis. *Can Respir J* 2018;**2018**:1–10. doi:10.1155/2018/7457369.

42. Bravo PE, Singh A, Carli MF Di, Blankstein R. Advanced cardiovascular imaging for the evaluation of cardiac sarcoidosis. *J Nucl Cardiol* 2019;**26**(1):188–199. doi:10.1007/s12350-018-01488-9.

43. Leone O, Veinot JP, Angelini A, Baandrup UT, et al. 2011 Consensus statement on endomyocardial biopsy from the Association for European Cardiovascular Pathology and the Society for Cardiovascular Pathology. *Cardiovasc Pathol* 2012;**21**(4):245–274. doi:10.1016/j.carpath.2011.10.001.

44. Cooper LT, Baughman KL, Feldman AM, Frustaci A, et al. The Role of Endomyocardial Biopsy in the Management of Cardiovascular Disease. *J Am Coll Cardiol* 2007;**50**(19):1914–1931. doi:10.1016/j.jacc.2007.09.008.

45. Nery PB, Keren A, Healey J, Leug E, et al. Isolated cardiac sarcoidosis: Establishing the diagnosis with electroanatomic mapping-guided endomyocardial biopsy. *Can J Cardiol* 2013;**29**(8):1015.e1-1015.e3. doi:10.1016/j.cjca.2012.09.009.

46. Liang JJ, Hebl VB, DeSimone C V., Madhavan M, et al. Electrogram guidance: a method to increase the precision and diagnostic yield of endomyocardial biopsy for suspected cardiac sarcoidosis and myocarditis. *JACC Heart Fail* 2014;**2**(5):466–473. doi:10.1016/j.jchf.2014.03.015.

47. Mcguirt D, Carolina N, Mazal J, Branch P, et al. X-ray Fused With Magnetic Resonance Imaging to Guide Endomyocardial Biopsy of a Right Ventricular Mass. *Radiol Technol* 2017;**87**(6):622–626.

48. Rogers T, Ratnayaka K, Karmarkar P, Campbell-Washburn AE, et al. Real-Time Magnetic Resonance Imaging Guidance Improves the Diagnostic Yield of Endomyocardial Biopsy. *JACC Basic to Transl Sci* 2016;**1**(5):376–383. doi:10.1016/j.jacbts.2016.05.007.

49. Unterberg-Buchwald C, Ritter CO, Reupke V, Wilke RN, et al. Targeted endomyocardial biopsy guided by real-time cardiovascular magnetic resonance. *J Cardiovasc Magn Reson* 2017;**19**(1):45. doi:10.1186/s12968-017-0357-3.

50. Casella M, Russo A Dello, Vettor G, Lumia G, et al. Electroanatomical mapping systems and intracardiac echo integration for guided endomyocardial biopsy. *Expert Rev Med Devices* 2017;**14**(8):609–619. doi:10.1080/17434440.2017.1351875.

51. Khan T, Selvakumar D, Trivedi S, Rao K, et al. The value of endomyocardial biopsy in diagnosis and guiding therapy. *Pathology* 2017;**49**(7):750–756. doi:10.1016/j.pathol.2017.08.004.

52. Tseng CC., Wenker S, Bakker MH, Kraaijeveld AO, et al. Active tracked intramyocardial catheter injections for regenerative therapy with real-time MR guidance: feasibility in the porcine heart. *EuroIntervention* 2018; doi:10.4244/EIJ-D-17-01081.

53. Eitel C, Piorkowski C, Hindricks G, Gutberlet M. Electrophysiology study guided by real-time magnetic resonance imaging. *Eur Heart J* 2012;**33**(15):1975. doi:10.1093/eurheartj/ehr414.

54. Grothoff M, Piorkowski C, Eitel C, Gaspar T, et al. MR Imaging–guided Electrophysiological Ablation Studies in Humans with Passive Catheter Tracking: Initial Results. *Radiology* 2014;**271**(3):695–702. doi:10.1148/radiol.13122671.

55. Lowe MD, Plummer CJ, Manisty CH, Linker NJ. Safe use of MRI in people with cardiac implantable electronic devices. *Heart* 2015;**101**(24):1950–1953. doi:10.1136/heartjnl-2015-308495.

56. Campbell-Washburn AE, Tavallaei MA, Pop M, Grant EK, et al. Real-time MRI guidance of cardiac interventions. *J Magn Reson Imaging* 2017;**46**(4):935–950. doi:10.1002/jmri.25749.

57. Barkhausen J, Kahn T, Krombach G, Kuhl C, et al. White Paper: Interventional MRI: Current Status and Potential for Development Considering Economic Perspectives, Part 1: General Application. *RöFo - Fortschritte auf dem Gebiet der Röntgenstrahlen und der Bildgeb Verfahren* 2017;**189**(07):611–623. doi:10.1055/s-0043-110011.

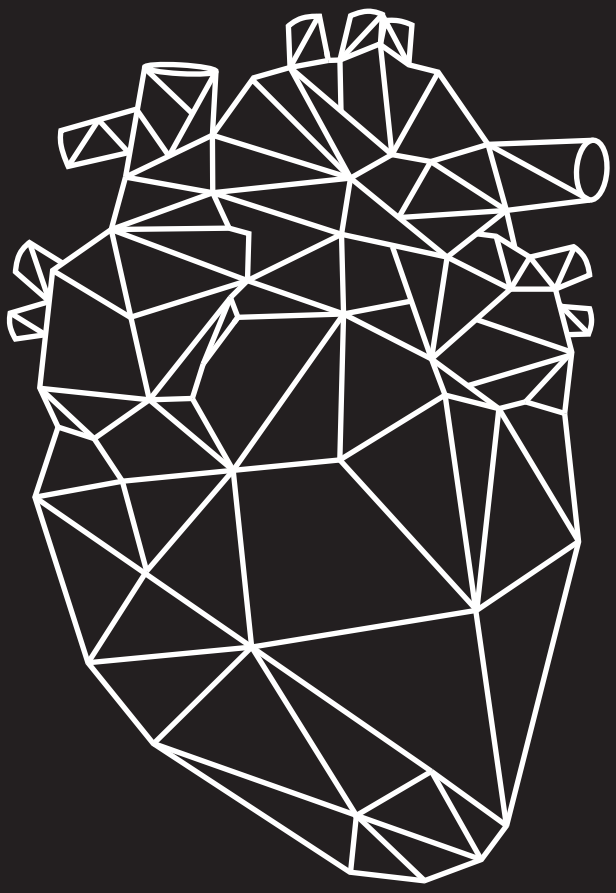

Appendices

Nederlandse Samenvatting
Dankwoord
List of Publications
Curriculum Vitae

Nederlandse samenvatting

Hart- en vaatziekten zijn wereldwijd de belangrijkste doodsoorzaak, met naar schatting 17,9 miljoen cardiovasculaire sterfgevallen in 2015. Een belangrijke bijdrage hieraan is hartfalen. Dit complexe klinische syndroom is aanwezig in ongeveer 2-3% van de volwassen bevolking, maar is het meest voorkomend bij ouderen boven de 65 jaar. Hartfalen is progressief van aard en ongeveer de helft van de patiënten die hartfalen ontwikkelen, sterft binnen 5 jaar na diagnose. Hartfalen wordt gekenmerkt door structurele of functionele stoornissen aan de linker- of rechterkamer, wat leidt tot een verminderde pompfunctie en/of verhoogde druk in het hart bij inspanning of in rust.

Een belangrijke oorzaak van het ontwikkelen van hartfalen is aanhoudende hartziekte als gevolg van kransslagadervernauwing (coronaire hartziekte) na een eerder doorgemaakt hartinfarct, ook wel hartaanval genoemd. In de acute fase van een hartinfarct kan de doorbloeding van de hartspier worden hersteld door een interventie. Dit kan zijn door een dotter- en stentbehandeling of bypassoperatie. Ondanks tijdige interventie kunnen patiënten klachten ontwikkelen als gevolg van de aanhoudende schade aan de hartspier in verband met de ischemische (onvoldoende doorbloeding) gebeurtenis. Om de hartfunctie te verbeteren en de klachten te onderdrukken, wordt een aanvullend medicatie behandeling gestart. Een andere veel voorkomende oorzaak van hartfalen is hoge bloeddruk, maar ook afwijkingen aan de hartkleppen, aan de binnen- of buitenkant van de hartspier, van het hartritme of van de elektrische geleiding kunnen leiden tot het ontwikkelen van hartfalen. De succesvolle interventionele en farmacologische behandeling van hart- en vaatziekten heeft bijgedragen aan een toenemende groep patiënten die coronaire hartziekte overleeft en uiteindelijk chronisch hartfalen ontwikkelt.

Bij patiënten met chronisch stabiel hartfalen wordt het syndroom vaak gereguleerd door aanpassingen aan de levensstijl en een behandeling met medicatie. Patiënten met matig tot ernstig hartfalen hebben echter interventies nodig, waaronder interventies om de bloedtoevoer in de hartspier te herstellen, klepreparatie en -vervanging om de klepstructuur te herstellen, cardiale resynchronisatie therapie om geleidingsvertragingen te

herstellen en het hartritme te verbeteren, en mechanische ondersteuning zoals een steunhart wanneer alle functies verloren zijn. Al deze interventies zijn bedoeld om linkerkamerverslechtering te voorkomen en/of de linkerkamerfunctie te verbeteren, de symptomen te verminderen en het leven te verlengen. De enige definitieve genezing van hartfalen is een harttransplantatie, maar dit is door een tekort aan donorharten alleen beschikbaar voor een beperkt aantal patiënten die lijden aan terminaal hartfalen.

Hoewel de huidige behandelingsstrategieën een gunstig effect hebben op de behandeling van patiënten met hartfalen, zijn optimalisaties en introductie van nieuwe therapieën nodig om de veiligheid, uitkomsten en het slagingspercentage van de interventies te verbeteren. Het effect van cardiale resynchronisatietherapie is bijvoorbeeld beperkt, in 55 tot 70% van de gevallen geeft de therapie verbetering van de conditie. Verschillende onderzoeken hebben echter aangetoond dat dit percentage kan worden verbeterd door bijvoorbeeld de stimulatie in de linkerkamer te richten op specifieke stimulatieplaatsen. Deze bevindingen laten zien dat optimalisaties van de huidige interventionele behandelingsstrategieën noodzakelijk zijn om de groeiende groep patiënten met hartfalen te helpen.

Nieuwe ontwikkelingen op het gebied van interventionele cardiologie hebben bijgedragen aan een betere kwaliteit van leven en overleving van patiënten met hart- en vaatziekten. Zo heeft het combineren van meerdere diagnostische beeldvormingsmodaliteiten nieuwe inzichten opgeleverd in de diagnose en het beheer van deze patiëntenpopulatie. In de interventiekamers zijn naast nieuwe beeldvormingstechnologieën geavanceerde kathetertechnieken en -therapieën routine geworden in een groot aantal centra over de hele wereld. De belangrijkste interventionele beeldvormingsmodaliteit blijft fluoroscopie of doorlichting, een techniek voor röntgenonderzoek. Fluoroscopie biedt live 2D-beeldvorming van hoge beeldkwaliteit maar heeft verschillende nadelen. Zo wordt de patiënt blootgesteld aan straling, is de beeldvormingsmodaliteit minder geschikt voor de weergave van diepte door ondoorzichtigheid van overliggende structuren en ontbreekt de visualisatie van zacht weefsel. Om interventionele behandelingsstrategieën verder te optimaliseren, moeten verschillende uitdagingen worden overwonnen:
1. Driedimensionale beeldvorming; 2. Visualisatie van zacht weefsel; 3. Preoperatieve behandelplanning; 4. Beperking van blootstelling aan straling en contrastmiddelen.

In dit proefschrift wordt de ontwikkeling van een nieuw medisch hulpmiddel beschreven. Dit medische hulpmiddel is een nieuw ontwikkelde softwaretool voor beeldgeleide hartkathetertherapie, CARTBox (CART-Tech B.V., Utrecht, Nederland). De softwaremethode maakt een selectie van optimale therapiedoelen mogelijk op basis van o.a. infarct-transmuraliteit (percentage van de wanddikte dat littekenweefsel is) en lokale wanddikte van de hartspier, afgeleid van preoperatieve MRI-scans. Fusie van de geselecteerde doelen met live fluoroscopie maakt real-time visualisatie mogelijk van MRI-gedefinieerde doelen tijdens de door fluoroscopie geleide interventies. Deze techniek wordt hybride beeldvorming genoemd.

Hybride beeldvormingstechnologieën maken het mogelijk om organen en weefsels te visualiseren tijdens cardiovasculaire interventies door verschillende beeldvormings-modaliteiten te integreren. Hybride beeldvorming kan de werkzaamheid en veiligheid van interventies verbeteren. De grote bedrijven op het gebied van interventionele fluoroscopie systemen bieden softwaremogelijkheden voor het gebruik van hybride beeldvorming. In **hoofdstuk 2** hebben we middels een literatuuronderzoek een overzicht opgesteld van de verschillende commercieel beschikbare systemen die binnen de afdeling cardiologie worden gebruikt, hun mogelijkheden, hun huidig klinisch gebruik en hun voordelen in de context van structurele en aangeboren hartaandoeningen. Hierbij is vastgesteld dat de momenteel beschikbare onderzoeken worden beperkt door te kleine patiënten aantallen. Niettemin resulteert het gebruik van hybride beeldvorming systemen tijdens aortaklepimplantaties in een significante afname van blootstelling aan straling en contrast. Het grootste voordeel hiervan wordt waargenomen wanneer hybride beeldvorming wordt gebruikt in combinatie met 3D-rotatie-angiografie. Bovendien verminderen algoritmes waarmee automatisch de optimale implantatiehoek voor transkatheter-aortaklepimplantatie wordt bepaald, het aantal complicaties aanzienlijk. Het gebruik van hybride beeldvorming systemen tijdens aangeboren hartafwijking interventies resulteert eveneens in een significante afname in stralings- en contrastblootstelling en een afname in proceduretijd. Er zijn dus softwareoplossingen voor hybride beeldvorming die veilig zijn en kunnen helpen bij de planning en beeldgeleiding van cardiovasculaire interventies. Hoewel de huidige hybride beeldvorming technologieën beperkingen hebben, biedt hybride

beeldvorming ondersteuning om betere patiëntenzorg te bieden bij de steeds complexere cardiale interventieprocedures.

De klinische vertaling van nieuwe beeldgeleide katheterinterventies vereist meer precieze validatietechnieken om de nauwkeurigheid van de gerichte toepassing van therapie van deze nieuw ontwikkelde methoden te beoordelen en te valideren. Met het oog op de ontwikkeling van de nieuwe softwaremethode, CARTBox, hebben we een nieuw validatieprotocol ontwikkeld, bedoeld voor dierenstudies, op basis van weefselanalyse. Dit protocol, beschreven in **hoofdstuk 3**, omvat de methode voor weefselverwerking van het hele hart waardoor een gedetailleerde 2D- en 3D-analyse van de hartanatomie en van de injecties in het hart mogelijk wordt gemaakt. In een pilotstudie hebben we laten zien dat agarose een geschikt medium is voor de inbedding van het hele hart, waardoor het weefsel in de gewenste hoek en in gelijke dikte kan worden gesneden. Bovendien is het mogelijk om de resulterende beelden middels beeldregistratie te reconstrueren tot een 3D-model geschikt voor 3D-analyse in hoge resolutie. Het protocol biedt een gestructureerde en reproduceerbare methode voor de beoordeling van de richtnauwkeurigheid van injecties in het hart en kan gemakkelijk worden ingezet voor kwalitatieve en kwantitatieve onderzoeksdoelen.

Dezelfde weefselanalysemethode hebben we vervolgens in **hoofdstuk 4** ingezet om CARTBox2 te valideren. In een non-inferioriteitsonderzoek is de richtnauwkeurigheid van de nieuwe softwaremethode voor door MRI-fluoroscopie geleide katheterinterventies vergeleken met de klinische standaard voor injecties in het hart, het elektromechanische mapping systeem NOGA. Naast de richtnauwkeurigheid is ook de duur van de procedure, de hoeveelheid straling en het aantal hartritmestoornissen gemeten. De studie is uitgevoerd in twee groepen met vijf dieren. In alle dieren is een infarct geïnduceerd en na vier weken zijn per dier 10-16 injecties geplaatst met het NOGA systeem dan wel met CARTBox2. De injecties waren gericht op het grensgebied van het infarct, gedefinieerd als 1-20% infarct-transmuraliteit. Na de injecties is het hart verwijderd en is het validatieprotocol, uit hoofdstuk 3, toegepast om de afstand van de injecties tot het infarctgrensgebied te meten. De resultaten van de studie laten zien dat beide technieken een vergelijkbare nauwkeurigheid behalen. De gemiddelde afstand van de injecties tot het

infarctgrensgebied ligt met NOGA op 0.7 ± 2.2 mm aan de binnenzijde van het infarct en met CARTBox2 op 0.5 ± 3.2 mm buiten het infarct. Omdat de CARTBox-techniek gebruik maakt van hybride beeldvorming, door MRI met fluoroscopie te combineren en het NOGA systeem gebruik maakt van magnetische tracking, is de gemeten stralingsdosis bij CARTBox hoger. De stralingsdosis bij een CARTBox2 procedure is echter lager dan de gemiddelde dotterprocedure. In tegenstelling tot het NOGA systeem, waar eerst een mapping procedure aan vooraf gaat, kan er met de CARTBox techniek direct worden gestart met plaatsing van de injecties waardoor deze procedures korter zijn dan met NOGA. Met de CARTBox methode is een standaard cardiale MRI scan voorafgaand aan de procedure vereist. In deze studie zijn geen verschillen gezien in het aantal hartritmestoornissen tijdens het plaatsen van injecties met beide technieken. De conclusie is dat CARTBox2 een snel en accuraat systeem is, dat enkel software omvat, om injecties in het hart uit te kunnen voeren op basis van gouden standaard MRI-afbeeldingen.

De CARTBox-technologie is doorontwikkeld voor het gebruik tijdens de implantatie van een cardiaal resynchronisatie device, CARTBox3. Cardiale resynchronisatie- therapie is een behandeling voor patiënten met hartfalen waarbij de geleiding over de kamers ongelijk loopt. De therapie is gericht op het herstellen van geleidingsvertragingen en het verbeteren van het hartritme. Tijdens de procedure worden elektrodes geplaatst in beide kamers en in de rechter boezem. Cruciaal voor een succesvolle therapie is de plaatsing van de linkerkamerelektrode. De elektrode dient geplaatst te worden in het gebied waar de dyssynchronie het grootst is en uit de buurt van littekenweefsel en de linker middenrif zenuw. Het littekenweefsel wordt gemeden omdat uit eerdere onderzoeken is gebleken dat het plaatsen van de elektrode dichtbij het litteken resulteert in verslechterde hartconditie. Stimulatie van de linker middenrifzenuw is niet gewenst omdat dit leidt tot chronisch hikken. Door gebruik te maken van beeldgeleiding tijdens het plaatsen van de linkerkamerelektrode bij de implantatie van een cardiaal resynchronisatie device kan het aantal complicaties verlaagd worden en het aantal patiënten, dat baat heeft bij de therapie, vergroot worden.

De veiligheid en haalbaarheid van het CARTBox3-beeldgeleidingsplatform is geëvalueerd in een eerste patiëntenstudie beschreven in **hoofdstuk 5.** Bij vijftien patiënten werden optimale stimulatieplaatsen preoperatief geïdentificeerd met behulp van cardiale beeldvorming. Alle patiënten ondergingen MRI om het littekenweefsel en dyssynchronie te lokaliseren en te visualiseren. Bij zes patiënten werden de anatomie van de linker middenrifzenuw en de uitmonding van de sinus coronarius beoordeeld middels een CT-scan. Door de MRI- en CT-afbeeldingen in 3D op real-time fluoroscopie te leggen, werden de bovengenoemde structuren gevisualiseerd tijdens beeldgeleide plaatsing van de linkerkamerelektrode. Bij de eerste negen patiënten werd het platform getest, maar er werd geen real-time beeldgeleiding geïmplementeerd. Bij de laatste zes patiënten werd real-time beeldgeleide plaatsing van de linkerkamerelektrode met succes uitgevoerd. De CRT-implantatieduur en de duur van doorlichting was met de CARTBox technologie vergelijkbaar met de conventionele plaatsing van de linkerkamerelektrode. In alle patiënten is de elektrode dicht bij het doelgebied geplaatst, maar verwijderd van het littekenweefsel en de linker middenrifzenuw. Bij patiënten die real-time beeldgeleide plaatsing van de linkerkamerelektrode ontvingen, werd de linkerkamerelektrode dichter bij het doelgebied geplaatst in vergelijking met patiënten die geen real-time beeldgeleiding kregen, respectievelijk 8 mm en 26 mm. In de zes maanden follow-up was te zien dat bij de beeldgeleide plaatsing van de linkerkamerelektrode omkering van het proces van remodellering van de hartspier optrad. Dit ging gepaard met een gemiddelde eind-systolisch volumeverandering van de linkerkamer van -30 ± 10% en een gemiddelde ejectiefractie verbetering van de linkerkamer van 15 ± 5%. Real-time beeldgeleide plaatsing van de linkerkamerelektrode door fusie van MR- en CT-beelden met fluoroscopie beelden tijdens cardiaal resynchronisatie device implantatie is haalbaar. Beeldgeleiding ondersteunt de gerichte plaatsing van de linkerkamerelektrode bij de optimale locatie en uit de buurt van littekenweefsel ten opzichte van alleen preoperatieve behandelingsplanning.

Veel hartprocedures vereisen nauwkeurig onderscheid tussen gezond hartweefsel en littekenweefsel. De standaard voor het vaststellen van de aanwezigheid van littekenweefsel is middels MRI, maar tijdens hartinterventies wordt meestal elektro-anatomische (of mechanische) mapping gebruikt. Daarom is naast de ontwikkeling van een nieuw medisch hulpmiddel ook onderzocht of met het gebruik van oude data het eerder beschreven elektro-anatomische mapping systeem, NOGA, te verbeteren is. In **hoofdstuk 6** is een studie beschreven waarin een statisch model is ontwikkelt om de aanwezigheid van littekenweefsel op basis van een combinatie van meerdere elektromechanische parameters te voorspellen. In een retrospectieve studie is de voorspellende nauwkeurigheid van dit model geëvalueerd in een varkensmodel met een chronisch hartinfarct. Als eerste stap zijn elektromechanische maps met een hoge dichtheid van het NOGA systeem in 3D samengevoegd met MRI. Voor het statistisch model is een multivariaat mixed-effect logistisch regressiemodel gebruikt. Daarnaast zijn de weefseldeformatieparameters afgeleid van de MRI gecorreleerd met de elektromechanische afgeleide metingen van lokale mechanische activiteit. In totaal zijn van dertien dieren 787 NOGA punten vergeleken met de corresponderende MRI-locaties. De gemiddelde registratiefout was 2.5 ± 1.16 mm. Het model is nauwkeurig in het onderscheiden van gezonde hartspierweefsel van littekenweefsel. Unipolaire en bipolaire voltages waren de sterkste voorspellers voor de aanwezigheid van littekenweefsel in de hartspier. De elektromechanische afgeleide metingen van lokale mechanische activiteit waren niet significant gecorreleerd met de MRI afgeleide parameters voor weefsel deformatie. De volgende stap is dit model te testen in een klinische dataset en te vergelijken met de gouden standaard.

Dankwoord

In dit dankwoord wil ik graag iedereen bedanken die heeft bijgedragen in de totstandkoming van dit proefschrift.

Prof. dr. **S.A.J. Chamuleau**, Beste **Steven**, in 2014 kwam ik tijdens mijn laatste 5e jaar stage op de afdeling cardiologie terecht. Onder supervisie van jou en Frebus heb ik vervolgens mijn afstudeerstage bij jou mogen doen en vroeg je mij al gauw om aansluitend een PhD traject in te gaan. Eerst als co-promoter en halverwege de rit ben je professor geworden en daarmee ook eerste promotor. Samen hebben we een aantal leuke studies opgezet en uitgevoerd en veel besproken tijdens de gezellige ChamPhD meetings. Ik hoop dat je de meetings nieuw leven kunt inblazen! De BBQ's en etentjes o.a. bij jou thuis met je gezin natuurlijk niet te vergeten, deze hebben een indruk achter gelaten. Je doortastendheid en klinische blik heb ik altijd zeer gewaardeerd en veel aan gehad, dank voor de afgelopen 4.5 jaren.

Prof. dr. **P.A.F.M. Doevendans**, Beste **Pieter**, zo snel en doeltreffend de antwoorden op mijn e-mails vaak waren (OK PD) waren ook onze meetings 'to-the-point'. Ik was één van de vele PhD studenten op de afdeling maar toch wist je altijd waar ik mee bezig was en vooral wat mijn volgende stap moest gaan zijn. Daarmee bleef je mij verbazen, ook toen Steven eerste promoter werd. Bedankt voor de korte maar krachtige meetings de afgelopen jaren en natuurlijk de zeer gezellige kerstborrels!

Dr. ir. **F.J. van Slochteren**, Beste **Frebus**, ik begon in 2014 als TG student bij jou en Steven maar uiteindelijk werd ik jouw eerste PhD student. We hebben in de afgelopen jaren heel veel mooie studies opgezet en uitgevoerd en daar was jouw technische kennis vaak onontbeerlijk. Ik heb je op veel facetten mogen meemaken, als regelrechte onderzoeker, als entrepreneur, als begeleider, en als vriend. Bedankt voor de vele meetings, congres tripjes, en etentjes afgelopen jaren! Niet alleen in het UMCU heb ik veel van je geleerd maar ook binnen CART-Tech, van software design tot software testen en alle documentatie behorend bij medische device ontwikkeling. Ik heb van dichtbij mogen meemaken, en kunnen bijdragen aan, hoe je bedrijf is uitgegroeid tot wat het nu is. Er is weliswaar nog een

lange weg te gaan maar ik wens jou heel veel succes met het uitbouwen van de startup en ik wil **Paul Leufkens** daar natuurlijk ook bij betrekken!

Dr. **R. van Es**, Beste **Rene**, als tweede technische geneeskunde promovendus kwam ik in de groep van Chamuleau. Ik zag je de ene na de andere technische geneeskunde student begeleiden, eerst als promovendus en later als doctor. Niet veel later werd je mijn co-promoter, vervolgens werd **Marijn** jouw tweede promovendi. Jouw veelzijdige blik heb ik altijd als zeer prettig ervaren, een rasechte onderzoeker met veel out-of-the-box ideeën. Daarnaast was je altijd te porren voor een goede discussie, koppen koffie in de appendix, borrels, en super georganiseerde etentjes. Ook al ben je niet uit de villa weg te slaan, ik wens je een mooi kantoor en bijbehorende carrière toe!

De leden van de lees commissie, prof dr. **B.K. Velthuis**, prof. dr. **G.J. de Borst**, prof. dr. ir. **H.W.A.M. de Jong**, prof. dr. ir. **C. Slump**, prof. dr. **N.S. de Groot**, bedankt voor de bereidheid zitting te nemen in de beoordelingscommissie van mijn proefschrift. Daarnaast wil ik ook dr. **J.F. van der Heijden** en dr. **A.O. Kraaijeveld** bedanken voor de bereidheid om zitting te nemen in de oppositie.

Natuurlijk wil ik ook alle (oud-)onderzoekers van de afdeling cardiologie bedanken. Beste **Sanne**, **Geert**, **Peter-Paul**, **Martine**, **Marloes**, **Freek**, **Cas**, **Lennart, Tom, Rob, Odilia, David, Agnieska, Max. Iris**, wat enig dat we samen de dierproefkunde cursus hebben gedaan. **Cheyenne**, de koele kikker van de villa, erg prettig voor wat adviezen met name tijdens mijn stagetijd. **Wouter G**, ik ben heel benieuwd naar meer mooie tekeningen van de natuur, veel succes bij de radiologie, wanneer gaan we nou een bordspel spelen? **Thomas** en **Remco**, jullie tempo bier drinken was ongeëvenaard, alleen **Dirk** kwam nog in de buurt met de snelheid waarmee hij promoveerde. **Wouter E**, ik heb een hilarische tijd gehad samen bij de hartstichting cursus, het was daarnaast een eer dat ik bij jouw bruiloft mocht zijn. **Timion**, je komst in de villa was kort maar krachtig, hopelijk heb ik je (naast mijn flauwe humor) kunnen meegeven hoe een dual-monitor setup aangesloten moet worden. **Marijn**, nu weer de enige TG promovendus binnen de afdeling maar dat zal vast niet lang duren, aan jou de eer om tot die tijd de TG vlag hoog te houden. **Evangeline**, noemenswaardig is je inzet om me op de hoogte te houden van borrels zelfs toen ik al niet meer in dienst was.

Bas, op jou kon ik altijd vertrouwen dat mijn Jiskefet grappen opgepikt werden en je haakte dan ook dikwijls in op de vele sketches. **Einar**, de viking van de afdeling, ik heb erg genoten van jouw 'heldere' momenten, humor, en ongezouten mening in goede discussies. **Odette**, ik heb met veel plezier samen aan de ADVISE studie gewerkt, wat hadden de CART-Tech mannen zonder ons gemoeten in Barcelona. **Rik,** bedankt voor de koffiemomenten tijdens de promotie en in de afrondende fase van het boekje. Alvast succes met jouw verdediging. **Arjan**, naast je serieuze kant kun je praten als Brugman, Sofia en Krakau waren een genot. Zele! **Mira**, mijn trouwe appendix-genoot van de villa, met jou heb ik de nodige momenten kunnen sparren over wat gaande was en andersom ook natuurlijk, gelukkig was je mijn flauwe grappen nooit zat. **Steven**, altijd paraat met Dumpert oneliners, lekker boyski, laten we vooral het boulderen erin houden.

Voor iedereen die het betreft, heel veel succes met de rest van jullie promotie. Dit geldt natuurlijk ook voor alle andere onderzoekers uit het Nest, Q, Medische Fysiologie, en andere (nieuwe) plekken. Bedankt voor de gezelligheid.

Het experimentele cardiologie lab van de afdeling cardiologie. Beste **Alain**, **Zhiyong**, **Hamid**, **Esther**, **Corina**, **Judith**, **Lena**, **Emma**, **Patricia**, **Evelyne**, **Marijn**, **Klaus**, en natuurlijk prof. dr. Joost Sluijter, Beste **Joost**, als ik af en toe weer eens de voortgang mijn projecten bij de stamcel besprekingen presenteerde zag ik menig oren wapperen door alle beeldvorming en andere technische kennis. Jullie stonden open voor mijn medische technische input en gaven constructieve feedback. Andersom was het ook vaak zo dat ik de verscheidene onderwerpen die voorbij kwamen soms lastig te begrijpen vond. Toch heb ik dankzij jullie veel geleerd over de biologie, jullie werk en de oplossingen. Ik heb met heel veel plezier met jullie samengewerkt!

Aan de studenten die heb mogen begeleiden, bedankt voor al jullie inzet en gezelligheid! **Marloes**, **Eliane**, **Niels**, **Tim**. **Tom**, ik had je nooit moeten vragen voor de 2018 WK voetbalpoule, we hadden geen schijn van kans meer. **Leon**, hele dagen harten inbedden in agar is zo gek nog niet onder het genot van kruidnoten en Jiskefet! Succes in de toekomst.

Niet mijn student maar wel het vermelden waard, **Rutger**, genoemd in het rijtje technische geneeskunde studenten maar met je zeer brede interesse en kennis denk ik dat TG je niet had misstaan.

Alle stafleden van de afdeling cardiologie. Bedankt voor jullie kleine en grote bijdragen aan mijn onderzoek. In het bijzonder dr. M. Meine, beste **Mathias**, bedankt voor de goede en leuke CRT en ADVISE meetings! Ik heb je nog nooit somber meegemaakt en je stond altijd paraat met mooie flauwe humor, dat kan ik waarderen! Natuurlijk ook **Tamara**, **Sylvia**, **Jantine**, **Ingrid**, heel erg bedankt voor de gezelligheid in jullie kamer en alle zaken die jullie voor mij geregeld hebben in de afgelopen jaren.

Experimentele cardiologie medewerkers in het GDL. Beste **Marlijn**, **Joyce**, **Martijn**, **Evelyn,** het was soms even bikkelen door de lange dagen die we samen maakten maar enorm bedankt voor de hulp en de gezelligheid tijdens de dierexperimenten.

Beste **Marion**, **John,** heel erg bedankt voor jullie gezellige gesprekken en alles wat jullie voor mij geregeld of geleerd hebben op het research lab en de radionuclide apotheek.

Alle onderzoekers en radiologen die mij geholpen hebben tijdens mijn onderzoek. Beste **Joep**, **Martijn**, **Niels**. Altijd paraat voor hulp bij de MRI, ik heb veel van jullie geleerd o.a. op het gebied van scannen! Daar naast ook dr. F.A.A. Mohamed Hoesein, beste **Firdaus**, de samenwerking in de ADVISE-CRT studie was kort maar krachtig en heb ik als zeer prettig ervaren. Grappig dat ik je na de studie steeds vaker tegen kwam, dat zal in de toekomst zeker nog wel eens gebeuren!

Medewerkers bij de diergeneeskunde. Beste **Anke**, **Monique**, **Ingrid**, **Jeanette**, onwijs bedankt voor de gezelligheid bij de DGK tijdens alle ochtenden, middagen en avonden scannen!

Dansvrienden, **Dennis**, **Freya**, **Mick**, **Naomi**, **Donald**, **Annelienke**, **Arjan** en **Bernadet**, we kennen elkaar pas een paar jaar maar dat mag de pret niet drukken. De danslessen en dansfeesten zorgden ervoor dat wij een leuke vriendengroep gevormd hebben die dadelijk alweer aan het vierde jaar gaat beginnen.

Bang!, **Thijs**, **Luuk**, **Bruce**, **Rob**, **Seline**, ondanks dat we allemaal druk waren konden we toch met enige regelmaat een middag plannen voor Bang!, Mansions of Madness, en andere bordspellen. Bedankt voor deze gezellige middagen en avonden!

Tweakers, **Marc**, **Thomas**, **Edwin**, **Wiel**, **Mischa**, **Jurian**, **Jeroen**, **Tom** en adoptie-Tweakers **Luuk, Alexander**, **Chiel** de meesten van jullie heb ik in 2010 leren kennen tijdens ons jaarlijkse weekend weg met Tweakers maar inmiddels uitgegroeid tot o.a. een hechte vriendengroep. Bedankt voor alle leuke momenten en epische mannenweekenden de afgelopen jaren.

Studie vrienden, **Nick**, **Erwin**, **Bart**, **Brian**, **Sander**, **Razmara**, **Lex**, **Ali**, en alle aanhang heel erg bedankt voor alle geduld die jullie gehad hebben de afgelopen jaren en met name de afgelopen maanden. We hebben elkaar in het laatste jaar van de PhD veel te weinig gezien en gesproken maar toch waren er soms nog wel wat momenten in de drukke agenda's vrij. Laten we, nu we in de volgende fase beland zijn, vooral weer vaker borrelen, met elkaar dineren, spelletjes- en Jiskefet avonden beleven.

Beste Paranimfen, **Mira** en **Nick**, jullie zijn natuurlijk eerder al genoemd maar ere wie ere toekomt en daarom wil ik jullie nog in het bijzonder bedanken. Bedankt voor alle inzet en werk wat jullie verzet hebben afgelopen tijd, zonder jullie hulp en ideeën had ik het niet tot zoiets moois kunnen brengen. Ik ben blij dat jullie mijn paranimfen wilden zijn!

Lieve familie, **Mam**, **Hanneke**, wat fijn dat jullie mijn familie zijn. Het zijn heel wat turbulente jaren geweest en soms was de radiostilte voor mij even nodig om alles te kunnen ondernemen wat ik op de planning had staan. Bedankt voor alle begrip, steun en liefde die jullie mij gegeven hebben.

Lieve vriendin, **Rosanne**, we hebben elkaar leren kennen toen ik net terug was van mijn reis in Indonesië. We troffen elkaar aan op het punt dat ik klaar was om vers te beginnen aan mijn promotie traject. Inmiddels wonen we alweer een jaar samen in ons mooie appartement in Utrecht! Bedankt dat je me de afgelopen vier jaren (drie jaren en een paar maanden in dienst) de ruimte hebt gegeven die ik nodig had en het geduld hebt weten op te brengen die daarvoor soms nodig was. Niet te vergeten de onvoorwaardelijke liefde die je altijd hebt gegeven!

List of Publications

Van den Broek, H. T., De Jong, L., Doevendans, P. A., Chamuleau, S. A., Van Slochteren, F. J., Van Es, R. 3D Whole-heart Myocardial Tissue Analysis, J. Vis. Exp, 2017.

Van den Broek, H. T., van Es, R., Krings, G. J., De Ruiter, Q. M. B., Voskuil, M., Meine, M., Loh, P., Doevendans, P. A., Chamuleau, S. A. J., Van Slochteren, F. J. 3D Hybrid Imaging for Structural and Congenital Heart Interventions in the Cath Lab, Structural Heart, 2018.

Van Es, R., **Van den Broek H. T.**, Van der Naald, M., De Jong, L., Nieuwenhuis, E., Kraaijeveld, A.O., Doevendans, P. A., Chamuleau, S. A. J., Van Slochteren, F. J. Validation of a novel stand-alone software tool for image guided cardiac catheter therapy, Int J Cardiovasc Imaging, 2019.

Van den Broek, H. T.*, Salden, O. A. E.*, Van Everdingen, W. M., Mohamed Hoesein, F. A. A., Velthuis B. K., Doevendans, P. A., Cramer, M., Tuinenburg, A. E., Leufkens, P., Van Slochteren, F. J., Meine, M., Multimodality Imaging for Real-Time Image-Guided Left Ventricular Lead Placement during Cardiac Resynchronization Therapy Implantations. Int J Cardiovasc Imaging, 2019.

The first two and last two authors contributed equally to this manuscript.

Van den Broek, H. T., Wenker, S., Van de Leur, R., Doevendans, P.A., Chamuleau, S.A.J., Van Es, R., Van Slochteren, F.J., 3D Myocardial Scar Prediction Model Derived from Multimodality Analysis of Electromechanical Mapping and Magnetic Resonance Imaging, J of Cardiovasc Trans Res, 2019.

Curriculum Vitae

Hans Thijs van den Broek was born on December 7th, 1987 in Arnhem, the Netherlands. He grew up in Arnhem with his mother Ineke and younger sister Hanneke. After the graduation of secondary school, Thijs moved to Enschede to study Technical Medicine at the University of Twente. His interest in imaging made him follow the master track 'Medical Imaging and Interventions'. At the age of 27, Thijs received his MSc degree after finishing his Master Thesis at the Department of Cardiology of the University Medical Center Utrecht. During the Master Thesis project, Thijs developed a novel method for the translation of 3D treatment planning data to a vendor-independent solution.

During the master thesis, Thijs' attention was drawn to research and in 2015 he started as a Ph.D. candidate in the Department of Cardiology of the University Medical Center Utrecht. This Ph.D. study was performed as a part of the BMM SMARTCARE II project granted to Prof. Dr. S.A.J. Chamuleau. In this project, new regenerative therapies and treatment strategies are developed for ischemic heart disease. As a part of the project, Thijs (co-)authored multiple peer-reviewed papers and presented his work at national and international congresses. Under the supervision of Prof. Dr. S.A.J. Chamuleau, Prof. Dr. P.A.F.M. Doevendans, Dr. Ir. F.J. van Slochteren, and Dr. R. van Es the project resulted in the Ph.D. thesis entitled 'Advancing medical devices for novel image-guided percutaneous cardiac interventions'.

In July 2019, Thijs started working as a Clinical Product Owner Cardiology at Philips Medical Systems within the Cardiology Informatics business unit in Eindhoven.